

Dissertation

submitted to the
Combined Faculties for the Natural Sciences and for
Mathematics
of the Ruperto-Carola University of Heidelberg, Germany
for the degree of
Doctor of Natural Sciences

presented by
Dipl.-Phys. Tomasz Wocjan
born in Warsaw, Poland
Oral examination: December 16th, 2009

**Dynamics of DNA
in Nucleosomes and Plasmids
studied by Brownian dynamics**

Referees:

Prof. Dr. Jörg Langowski

Prof. Dr. Jeremy C. Smith

Zusammenfassung

Dynamik von DNS in Nukleosomen und Plasmiden untersucht mit Brownscher Dynamik

In dieser Arbeit wurde die Dynamik von DNS in Nukleosomen (DNS-Protein-Komplexe) und Plasmiden (DNS-Ringe), welche die grundlegenden strukturellen Einheiten für die Organisation von DNS in prokaryotischen und eukaryotischen Zellen sind, analysiert. Die Untersuchung von DNS Bewegung auf dieser Längenskala ist von Bedeutung für das Verständnis der übergeordneten Struktur, welche einen entscheidenden Faktor in der Regulierung von fundamentalen Prozessen, wie z.B. Transkription und Replikation, darstellt. Modelle von DNS und Nukleosomen sind mit Hilfe von Brownschen Dynamik Simulationen untersucht worden in Hinblick auf experimentelle Techniken wie Fluoreszenzkorrelationsspektroskopie (FCS), die zeitaufgelöste Informationen über die Bewegung von fluorophormarkierter DNS liefert, und dynamische Kraftspektroskopie (DFS), die die konformationellen Änderungen der nukleosomalen DNS unter Anwendung einer externen Kraft misst. Die Bewegung einzelner DNS Monomere ist bezüglich verschiedener Parameter untersucht worden, wobei eine Beschleunigung der Fluorophoredynamik in permanent gekrümmten DNS Sequenzen mit zunehmender Superhelizität aufgezeigt wurde. Darüberhinaus wurde die Rotationsdynamik des Fluorophoredipolmomentes berücksichtigt, welches eine mögliche Erklärung bietet für ein experimentell beobachtetes Rouseregime der Monomerbewegung. In Simulationen von Streckungsexperimenten wurde das Abrollen der DNS von dem Proteinkomplex analysiert. Im Rahmen der DFS Theorie wurden die kinetischen Raten und Energiebarrieren entlang des Reaktionweges, sowie Bindungsenergien berechnet und in Bezug zu experimentellen Daten gesetzt.

Abstract

Dynamics of DNA in Nucleosomes and Plasmids studied by Brownian dynamics

This thesis investigates dynamics of DNA within nucleosomes (DNA-protein complexes) and plasmids (DNA rings), which are the basic units of DNA organization in prokaryotic and eukaryotic cells. The study of DNA motion at this length scale is important for the understanding of higher-order structure, which plays a key role in the regulation of fundamental biological processes such as transcription and replication. Coarse-grained models of DNA and the nucleosome were analyzed using a Brownian dynamics simulations in the context of experimental techniques such as Fluorescence Correlation Spectroscopy (FCS), which provides time-resolved information on motion of fluorophore-labeled DNA, and Dynamic Force Spectroscopy (DFS), which probes conformational changes of nucleosomal DNA by the application of external force. Single DNA monomer motion was analyzed under varying parameters, which showed an acceleration of fluorophore dynamics in permanently bent DNA sequences with increasing superhelicity. Furthermore, the rotational dynamics of the fluorophore dipole moment was taken into account, which gives a possible explanation for the experimentally observed appearance of a Rouse-like regime for single monomer dynamics. Using stretching simulations, the DNA unwrapping transition from DNA/protein complex was studied. In the framework of the DFS theory, kinetic rates and energy barriers along the transition pathway as well as binding energies were calculated and related to experimental data.

Die vorliegende Arbeit wurde in der Zeit von Februar 2006 bis September 2009 am Deutschen Krebsforschungszentrum in Heidelberg in der Abteilung Biophysik der Makromoleküle unter der wissenschaftlichen Anleitung von Herrn Prof. Dr. Jörg Langowski angefertigt.

Contents

1	Biological Overview	17
1.1	DNA	17
1.2	DNA Supercoiling	19
1.3	Nucleosome	21
2	Theoretical concepts	29
2.1	Polymer theory	29
2.1.1	Ideal chain models	29
2.1.2	Polymer dynamics	32
2.1.3	Twisting motion in the Barkley-Zimm model	35
2.2	Single-molecule force spectroscopy	36
2.2.1	Phenomenological model of the rupture kinetics	37
2.2.2	Model-dependent description of the rupture kinetics	40
3	Model and Methods	43
3.1	DNA model	43
3.1.1	Mechanical properties of DNA	43
3.1.2	Electrostatic interaction	45
3.2	Histone core model	49
3.3	Forces and Torques	53
3.4	Hydrodynamic interactions	54
3.5	Brownian dynamics algorithm	55
3.6	Parametrization	56
3.6.1	DNA parameters	57
3.6.2	Histone octamer parameters	58
3.6.3	Simulation parameters	58
3.7	Initialization	59
3.8	Circular and superhelical DNA	61
3.8.1	Monte Carlo algorithm	62
3.8.2	pUC18 plasmid	62
3.9	Oligonucleosomes	64
3.9.1	Nucleosome-Nucleosome interaction	64
3.9.2	Excluded volume interaction	65
3.9.3	Internucleosomal forces and torques	67
3.9.4	Hydrodynamic interactions in oligonucleosome model	69

4	Dynamics of circular DNA	71
4.1	Circular DNA	71
4.1.1	Brownian dynamics time trajectories	72
4.2	Comparison to analytical solution	80
4.2.1	Gaussian semiflexible chain model	80
4.2.2	Barkley-Zimm model	82
4.3	Circular DNA with permanently bent sequences	83
4.4	Polarization effects	86
4.4.1	Fluorophore's dipole moment dynamics	87
4.4.2	FCS simulation	90
5	Nucleosome dynamics	97
5.1	DNA fluctuations at equilibrium	97
5.2	Nucleosome stretching simulations	100
5.2.1	Nucleosome conformations	101
5.2.2	Force-extension curves	104
5.3	Dynamic Force Spectroscopy	106
5.3.1	Rupture force distribution	115
5.3.2	Links to DFS experiments	116
5.3.3	Complete dynamic force spectrum	120
5.3.4	Effect of DNA charge renormalization	121
5.4	Oligonucleosomes	123
6	Concluding Remarks	129
6.1	Conclusion	129
6.2	Future perspectives	132
7	Appendix	133

List of Figures

1.1	DNA organization in chromatin structure	18
1.2	DNA structure	19
1.3	Electron microscopy image of supercoiled DNA	20
1.4	Histone protein and histone protein handshake motif	22
1.5	Nucleosome structure	25
1.6	Electron microscope images of the chromatin fiber	26
2.1	Schematic setup of single-molecule force spectroscopy experiment . . .	37
2.2	Schematic representation of energy surface under external force	39
3.1	Local coordinate system of DNA segments	44
3.2	Twisting angle between DNA segments	46
3.3	Schematic representation of histone octamer model	52
3.4	Initialization of nucleosome conformations	60
3.5	Nucleosome relaxation	61
3.6	Nucleosome-nucleosome interaction potential	66
4.1	Circular DNA conformations	72
4.2	Single monomer mean-square displacement	74
4.3	Local exponent of single monomer motion	75
4.4	Local writhe	78
4.5	End-loop acceleration	79
4.6	Internal motion of Gaussian semiflexible chain	81
4.7	DNA twisting motion	83
4.8	Local writhe for circular DNA with/without permanent bends	85
4.9	Internal motion of circular DNA with permanent bends	87
4.10	Schematic view of fluorophore attachment to superhelical DNA	88
4.11	Angular correlation of fluorophore dipole moment	89
4.12	Experimental FCS data on superhelical dynamics	92
4.13	Simulated FCS correlation curves	95
5.1	Thermal fluctuations of DNA in the nucleosome	99
5.2	Site exposure equilibrium constant	100
5.3	Effect of external force on adsorbed DNA	101
5.4	Nucleosome conformations during stretching	102
5.5	DNA contour length during stretching	103
5.6	Force-extension curves as function of stretching velocity	105

5.7	Force-extension curves as function of adsorption energy density	106
5.8	Mean rupture forces and phenomenological model	107
5.9	Contour surfaces of rupture force RMSD (I)	111
5.10	Contour surfaces of rupture force RMSD (II)	112
5.11	Contour surfaces of rupture force RMSD (III)	113
5.12	Description of mean rupture force and force variance by model-dependent approach	115
5.13	Rupture force probability distribution of single nucleosomes	116
5.14	Comparison of experimental and simulated rupture forces	117
5.15	Complete dynamic force spectrum	121
5.16	Effect of DNA charge renormalization on thermal DNA fluctuations in the nucleosome	123
5.17	Effect of DNA charge renormalization on force-extension curves and mean rupture forces	124
5.18	Contour surfaces of rupture force RMSD (IV)	125
5.19	Dinucleosome conformation and force-extension curve	126
5.20	Dinucleosome rupture force distribution	127
5.21	Trinucleosome conformations	127

List of Tables

3.1	DNA model parameter (nucleosome)	58
3.2	Histone core parameters (nucleosome)	59
3.3	Simulation parameters (nucleosome)	59
3.4	Simulation parameters (circular DNA)	63
3.5	DNA parameters (circular DNA)	63
3.6	Nucleosome-nucleosome interaction parameters	66
3.7	Excluded volume parameters	67
4.1	Mean-square displacement ratios	77
4.2	Radius of gyration for circular DNA	85
4.3	FCS simulation parameters	91
5.1	Phenomenological model parameters	108
5.2	Model-dependent approach parameters	114
5.3	Effective adsorption energy density and binding energy	120
5.4	Model-dependent approach parameters for renormalized DNA charge	123
5.5	Mean nucleosome distances in trinucleosomes	128

Introduction

The DNA molecule has a unique role in any living cell as the carrier of genetic information. It encodes the instructions for the synthesis of proteins, which in turn define the cellular structure and function. A fundamental question in biology is how the access to certain regions in the genome is regulated, such that DNA-processing proteins responsible for DNA transcription, replication and repair can exert their specific functions. On the other hand, DNA sequences or genes must be made inaccessible or silenced, if the corresponding information is not required. At the same time the entire DNA molecule has to be highly compacted to fit into the cell. These requirements can only be met by a highly dynamic organization of DNA. In the present work the dynamics of two basic structural units of DNA organization inside cells are studied - plasmids and nucleosomes.

DNA in prokaryotic cells often exists in the form of DNA rings, or so-called plasmids. The DNA molecule itself consists of two individual strands forming a double helix with a defined number of twists per length in the torsionally relaxed state, but by closing the DNA ends to a ring, an additional amount of twist can be introduced. The additional torsional stress of the DNA molecule induces a conformational change of the DNA ring, such that plasmids often adopt a superhelical conformation, which resembles a twisted telephone cord. Superhelicity is highly important for biological processes e.g. bringing two specific DNA sites in close contact, which is necessary for the initiation of transcription, replication and recombination [Wasserman and Cozzarelli, 1986]. A thorough understanding of these processes requires quantitative information about the internal dynamics of single sites on DNA. Recently the single monomer dynamics of linear and circular DNA have been measured with Fluorescence Correlation Spectroscopy (FCS) [Shusterman et al., 2004, Petrov et al., 2006, Shusterman et al., 2008]. FCS is based on a correlation analysis of photons emitted by fluorophore-labeled molecules moving through a small laser excitation focus and allows to calculate the dynamics from the correlation curves. In the experimental study [Shusterman et al., 2008] an acceleration of the dynamics on all time scales was observed with increasing superhelicity. Interestingly, on intermediate length scales the monomer dynamics showed characteristics reminiscent of a Rouse model [Shusterman et al., 2004, 2008]. The Rouse model provides a description of a flexible polymer in dilute solution neglecting hydrodynamic interactions between the individual chain monomers. This is surprising, since for a semiflexible polymer as DNA in dilute solution one would expect that hydrodynamic interactions are important.

A purpose of this thesis was to analyze the internal dynamics of single monomer sites by numerical simulations. A method which is suitable to study such a problem is a Brownian dynamics simulation. In Brownian dynamics (BD) the collisions of the small and fast solvent molecules are replaced by a stochastic force. The DNA is represented in a coarse-grained model as a chain of linear segments incorporating mechanical properties e.g. bending rigidity, as well as hydrodynamic and electrostatic interactions [Klenin et al., 1998]. The reduction of degrees of freedom allows to access relative large time and length scales, which are otherwise too costly in terms of computational resources. The motion of specific sites in linear DNA in the performed BD simulations was shown to be in excellent agreement with the theory of semiflexible polymers [Harnau et al., 1996]. Thus, in this thesis I analyzed how circularization and superhelicity change the single site motion, in particular whether superhelicity leads to accelerated dynamics. In plasmids locally curved DNA sequences occur, which adopt a bent conformation at equilibrium. In this context I also investigated the influence of the monomer position relative to a bent sequence.

In order to relate the simulations to FCS experiments the motion of a fluorophore attached to the local DNA segment was explicitly taken into account. Since the fluorophore absorbs linearly polarized light preferentially in direction parallel to its transition dipole moment, the effect of rotational dynamics on the experimental outcome in FCS measurements of single-fluorophore-labeled plasmids was studied. A FCS simulation toolbox [Krieger, 2009] allowed to calculate the autocorrelation function of the fluorescence intensity. An intermediate regime was observed only by excitation with polarized light, therefore the inclusion of polarization effects provides a possible mechanism to explain for the observed Rouse-like regime in FCS studies.

In eukaryotic cells DNA is wrapped in repetitive units around a cylindrical histone protein complex in about two turns, forming a series of nucleosomes. The formation of the complex between the numerous negative charges on DNA and the positively charged histone core is balanced by a high energy penalty required for bending of the semiflexible DNA molecule around the protein complex, but quantitative estimates of the binding energies are still missing [Schiessel, 2003]. In vivo proteins may change the DNA-histone interaction by reducing the charge on the histone proteins, which affects the degree of compaction of the chromatin fiber and therefore the activation of genes in this region of the genome.

On the other hand stretches of DNA buried inside the nucleosome can not be processed by many proteins as they are sterically occluded due to the close contact with the histone core surface. But it was shown that DNA undergoes thermal fluctuations such that the DNA transiently lifts off the histone core surface [Polach and Widom, 1995, Anderson and Widom, 2000, Li et al., 2005]. These fluctuations may dominate the binding kinetics for such proteins that do not actively rearrange nucleosomes by ATP-consumption.

In recent years, the dynamics of nucleosomes have been studied by single-molecule experiments which allowed to probe forces at the molecular level or even actively exert forces and investigate the mechanical response of DNA and proteins. The basic idea is that a single molecule is chemically fixed at its ends and stretched under constant

velocity or force loading rate conditions, while the exerted force is measured. Stretching experiments of trapped nucleosome arrays have shown that the outer DNA turn in the nucleosome unwinds at low force, while a considerable energy barrier hinders the complete unwinding of DNA from the nucleosome [Brower-Toland et al., 2002, Pope et al., 2005]. Although Brower-Toland et al. postulated strong chemical binding sites at the position of the energy barrier to explain this peculiar behavior, calculations on an analytical model indicate that the toroidal geometry of the nucleosome itself is of great importance to stabilization of the nucleosome [Kulić and Schiessel, 2004].

Here I studied the DNA unwrapping transition with a BD simulation of a coarse-grained histone core model. The model reflects the superhelical DNA geometry inside the nucleosome as known from X-ray crystallography [Luger et al., 1997, Davey et al., 2002]. The conformational DNA fluctuations from the histone core at equilibrium were simulated, which could be directly related to DNA site exposure probabilities from restriction enzyme accessibility assays [Polach and Widom, 1995]. In order to probe the transition to the nucleosome state with unwrapped DNA, I performed stretching simulations of single nucleosomes, which displayed characteristic force-extension curves as found in experiments. During unwrapping the transitional state is associated with a maximum of force, the rupture force, a quantity containing implicitly information about the energy landscape. Within the theoretical framework of Dynamic Force Spectroscopy (DFS) [Evans and Ritchie, 1997, Dudko et al., 2006], estimates on kinetic transition rates and the energy barrier along the transition pathway were obtained. Comparisons with stretching experiments of nucleosomal arrays [Brower-Toland et al., 2002, Pope et al., 2005] lead to quantitative statements about the strength of DNA-histone core interactions and binding energies.

At higher-order the nucleosomes fold into the chromatin fiber, whose exact structure and interactions are to date not fully understood. An experimental technique to test internucleosomal interactions inside the chromatin fiber is force spectroscopy [Cui and Bustamante, 2000]. The present work provides a framework for stretching simulations of oligonucleosomes, extending the single nucleosome model. It was applied to obtain preliminary results on oligonucleosome conformations and the mechanical response to stretching of dinucleosomes.

The thesis is organized as follows:

In Chapter 1 a brief biological overview of the genome at the different levels of organization in eukaryotes and prokaryotes is given.

Chapter 2 provides an introduction to polymer physics. Static and dynamic properties of ideal chains are summarized, laying the foundation for the DNA model. In the second part force spectroscopy and its application as a single-molecule manipulation technique are reviewed and the theoretical framework of DFS is elucidated.

In Chapter 3 a description of the DNA and histone core model is given and the Brownian dynamics algorithm is explained in detail. At the end of the chapter the oligonucleosome model is presented.

In Chapter 4 the dynamics of single monomers in circular DNA are investigated.

The focus of Chapter 5 lies on nucleosome dynamics at equilibrium and under mechan-

ical stress.

Finally concluding remarks and further perspectives are presented in Chapter 6.

Chapter 1

Biological Overview

The genetic information is stored in a long biomolecule, the DNA. The total length of DNA is about two meters in human cells, but it has to be compacted into a cell nucleus of only a few microns. At the same time the information encoded in the genome has to be processed, such that the cell can efficiently perform their biological functions. This requires the access of regulatory proteins and transcription factors to DNA. The solution to this problem lies in the complex hierarchical organization of DNA in the eukaryotic cell (see Fig. (1.1)).

On the lowest scale DNA is wrapped around a protein complex of cylindrical shape, which is known as nucleosome core particle. The individual nucleosome core particles are connected via an additional amount of free DNA, termed linker DNA. This structural organization provides already a certain compaction in linear dimension. At a higher scale the nucleosome array adopts an extended beads-on-a-string structure at low salt conditions, which makes a transition into a denser, more compact structure - a chromatin fiber with a diameter of 30 nm - by increasing salt to moderate ionic strength. The 30-nm chromatin fiber undergoes higher-order folding in loop structures of several kilo base pairs length, which finally are organized into the chromosomes.

In contrast to eukaryotes DNA is found to adopt a circular and often interwound structure in prokaryotes, which will be also reviewed in this chapter.

In the following section we give a short overview of the individual components of DNA organization.

1.1 DNA

Deoxyribonucleic acid (DNA) is the carrier of genetic information for all living organisms. It encodes the instructions for the construction of biomolecules such as proteins and ribonucleic acid (RNA), which are essential for the cell. The building block of DNA is the nucleotide - a joined structure of a pentose sugar ring (deoxyribose) to which a phosphate group and a nitrogenous base are covalently bonded. The nucleotide contains one of the four different aromatic bases adenine (A), thymine (T), cytosine (C) and guanine (G), and which represent the cell's alphabet to store information. Phosphodiester bonds between the sugar and phosphate group link together individual nucleotides, therefore forming the backbone of a single, unbranched DNA

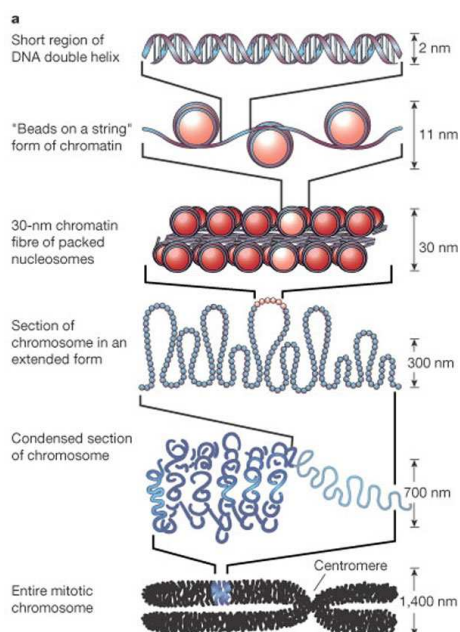


Figure 1.1: The organization of DNA within the chromatin structure. The basic packing unit is the nucleosome, in which about two superhelical turns of DNA are wound around a histone octamer. The nucleosomes are connected by linker DNA, and fold into a fiber of about 30 nm in diameter. The chromatin fiber is folded into a higher-order structure at the next level of organization (Figure adopted from [Felsenfeld and Klug, 2003]).

strand. The linking of the 5' carbon atom of a pentose ring to the 3' carbon atom of the adjacent nucleotide via a phosphate group introduces a direction in the DNA strand. Two antiparallel, complementary polynucleotide strands interact via hydrogen bonding between the bases. Here adenine pairs with thymine via two hydrogen bonds, while cytosine binds to guanine with three hydrogen bonds. The double strand is further stabilized by hydrophobic base stacking interactions and van-der-Waals interactions. The resulting 3-dimensional structure is a right-handed, double helix, in which the strands wind around each other such that the hydrophobic bases are hidden in the interior of the structure.

Three different structures of the double helix exist, known as A-DNA, B-DNA and Z-DNA. At physiological conditions the B-DNA structure is the most common. The B-DNA structure has a diameter of about 2 nm and successive base pairs in the double helix are stacked with a distance of 3.4 Å along the helical axis. On average each base pair is rotated with a twist angle of 34° with respect to the adjacent nucleotide pair, such that a complete helical turn has 10.5 base pairs. As the two DNA strands wind around each other, a major groove and a minor groove with a width of 22 Å and 12 Å respectively are formed in between the phosphate-sugar backbone. The geometry of the minor and major groove are important for the DNA interaction with proteins.

Deformations of the DNA structure like bending or twisting cost energy, as the optimal stacking of the base pairs and form of the phosphate-sugar backbone are distorted. The DNA structure therefore implies a bending rigidity of DNA, which restricts the flexibility of the molecule. A measure for the DNA flexibility is the persistence length, which will be introduced in section (2.1.1) on the basis of polymer models. It approximately describes the length scale on which the polymer can be considered as a stiff rod, while beyond the persistence length thermal fluctuations result in a decorrelation of the chain segment orientations.

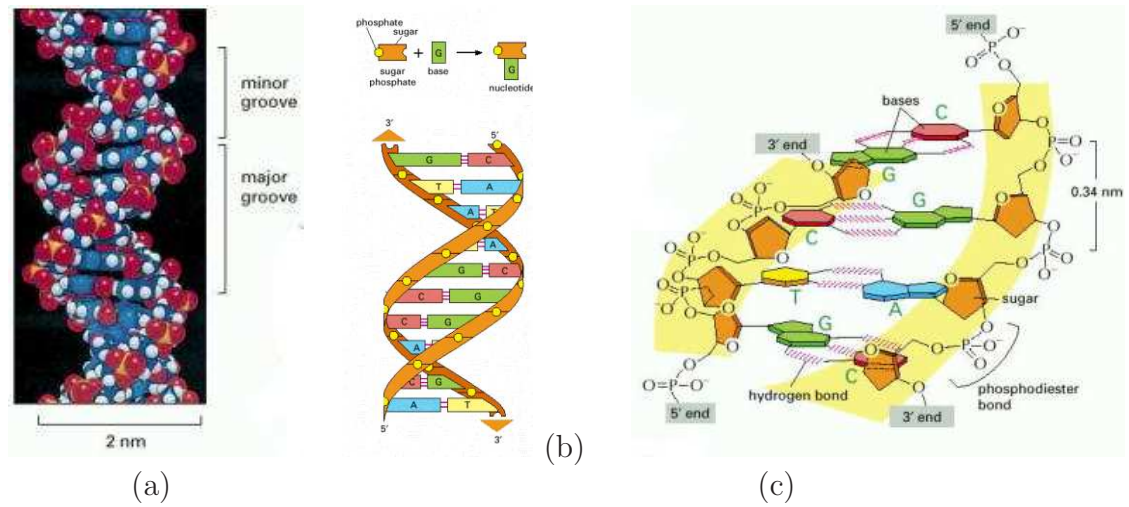


Figure 1.2: (a) Space-filling and (b) schematic model of the DNA structure. A DNA molecule consists of two anti-parallel strands, which are complementary in their nucleotide sequence and form a right-handed double helix with 10.5 bp per complete turn. The double helix structure forms a minor (1.2 nm) and major groove (2.2 nm) between the two winding DNA strands. Fig. (c) illustrates the formation of hydrogen bonding between base pairs and the phosphate-sugar backbone DNA strand. Adopted from [Alberts et al., 2002].

Besides the pure mechanical bending rigidity for DNA also the electrostatic repulsion between charges on the DNA backbone plays a central role. DNA is a highly charged molecule at physiological salt conditions, as the phosphate group of the backbone carries two negative elementary charges per base pair. Therefore only at high salt concentrations, at which the DNA charge is effectively screened, the pure mechanical value of 30 nm describes DNA flexibility [Manning, 1981]. Otherwise a higher value for the persistence length must be assumed. At physiological conditions experimental data is in agreement with a DNA persistence length of 50 nm [Hagerman, 1988].

In cell division the whole genome of the organism must be replicated and for this the double-stranded DNA structure provides a simple mechanism for DNA replication. As a result of the rather weak hydrogen bonds as compared to the covalently bonded sugar-phosphate the two single strands can be separated, while leaving the backbone intact. Then to each nucleotide in both DNA single strands a corresponding complementary nucleotide may bind, forming two complete copies of the original DNA molecule.

1.2 DNA Supercoiling

Biologically active DNA in bacteria and other prokaryotic cells, and also in yeast, is circular. The structures are called plasmids, and often adopt a supercoiled, conforma-

tion which resembles a twisted telephone cord e.g. as shown in Fig. (1.3). The typical plasmid size varies from one to several kilo base pairs.

For the formation of supercoiled DNA one may consider a closed DNA ring lying in a plane, which is initially in the torsional relaxed state of one complete helical turn per 10.5 bp. Then additional twist is induced by cutting the DNA at one position, twisting one DNA end around its axis and linking the two DNA ends together. In this torsionally stressed state, because neighboring segments of DNA are not coaxial, the torque will rotate one segment around the axis of the other. Ultimately the chain will be displaced from the plane in which the DNA was initially located. As a consequence in closed DNA rings, the change in the number of twist is related to a change of the spatial shape of the double helix as a whole. It results in a supercoiled structure for the considered DNA ring, where one DNA is interwound with the second.

The existence of supercoiled DNA was first shown in 1965 by electron microscopy and sedimentation studies [Vinograd et al., 1965]. Naturally occurring circular DNA chains are always underwound (negatively supercoiled), which is due to the presence of enzymes like gyrases. Gyrase, which are capable of twisting DNA, introduce supercoils in DNA. Underwound supercoils favor the unwinding of DNA occurring over a certain length of the molecule and facilitate subsequent processes of replication, transcription and recombination [Waigh, 2007]. Further enzymes called topoisomerases II change the topology of DNA rings by mutual crossing of DNA molecules. Bringing two or more specific DNA sites in close contact is important for many biological processes such as transcription and recombination [Wasserman and Cozzarelli, 1986]. It has been shown that supercoiled DNA facilitates the intrachain reaction by juxtapositioning of the sites greatly compared to relaxed DNA [Vologodskii et al., 1992, Jian et al., 1998]. In this biological context the dynamics of individual DNA sections is of great importance and is a main focus of the thesis.

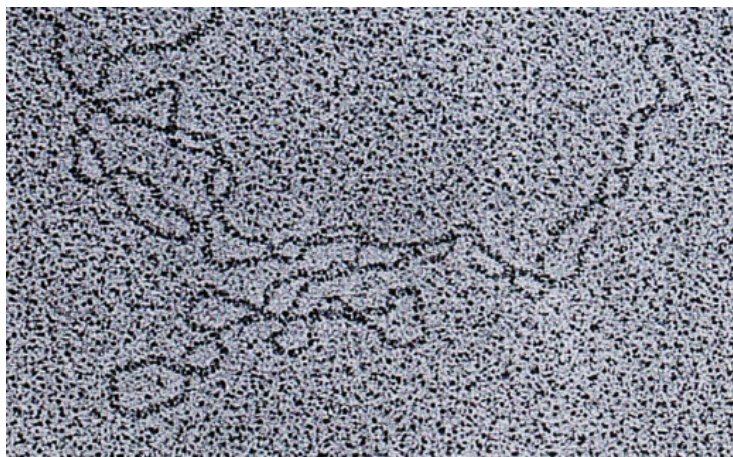


Figure 1.3: Electron microscopy of negatively supercoiled, interwound DNA (Figure adopted from [Boles et al., 1990])

1.3 Nucleosome

The basic packing unit of DNA in most eukaryotic cells is the nucleosome. First indirect evidence that about $\approx 80\%$ of DNA is organized into repetitive units has been found by nuclease digestion. Nucleases are particular enzymes, which are able to cleave free DNA at its phosphodiester bonds between the nucleotide subunits of nucleic acids. The exposure of nuclease to chromatin has revealed that the DNA in chromatin is degraded in discrete fragments, which contain multiples of a unit consisting of 180 to 200 bp [Williamson, 1970, Hewish and Burgoyne, 1973]. In the early 70's electron microscopic (EM) studies supported the hypothesis of a fundamental repeating unit in chromatin [Woodcock, 1973, Olins and Olins, 1974]. In detail the EM pictures resolved a bead-on-a-string structure of the DNA-protein complex fiber (see Fig. (1.6b)), which also explains why the nuclease acting only on the accessible DNA yields fragments of regular length. A further milestone was achieved by Kornberg who analyzed the constitution of the nucleosome in individual components, giving proof that the nucleosome is built up from histone proteins and DNA [Kornberg, 1974]. From the first structure obtained by X-ray crystallography [Finch et al., 1977], it was possible to stepwise improve the resolution of the nucleosome crystallographic structure [Richmond et al., 1984, Arents et al., 1991, Arents and Moudrianakis, 1993, Luger et al., 1997] up to a resolution of 1.9 Å [Davey et al., 2002, Richmond and Davey, 2003]. The crystallographic data established that the nucleosome core particle (NCP) forms a fairly rigid protein complex of cylindrical shape, consisting of 8 histone proteins, around which 146-147 bp of DNA are wrapped. The approximative shape of the nucleosome core particle as a cylinder has a diameter of 11 nm and a height of 5.5 nm.

Histone proteins

The histone core consists of two copies of each core histone protein H2A, H2B, H3 and H4. All histone core proteins are relatively small proteins with 102-135 amino acids and have a weight in the range of 11 to 16 kDa. Due to the large amount of lysine and arginine residues histones are also highly basic at near neutral pH. These proteins are structured in a histone-fold domain at the carboxyl (C-)terminal end of the protein and a charged tail at the amino (N-)terminal end [Wolffe, 1995]. In all core histones a long α -helix is connected by a nonhelical loop segment to shorter α -helices on each side to form the so-called histone-fold domain. In the nucleosome the histones form crescent-shaped heterodimers by interaction between the proteins histone-fold domains, which is described as handshake structural motif. Hereby the histone folds of H2A and H2B interact with each other, while H3 pairs with the H4 histone. The H3-H4 dimer associates further with a second H3-H4 dimer to form a tetramer $(\text{H3} - \text{H4})_2$. Finally the histone octamer is formed by binding of H2A-H2B dimers onto each side of the $(\text{H3} - \text{H4})_2$ tetramer.

With increasing salt concentration the H2A-H2B dissociate first and subsequently the H3 and H4 histone. This indicates that the interactions between the histone are mainly electrostatic in nature. The total histone core has about 220 cationic arginine and lysine residues [Khrapunov et al., 1997], which are positively charged at physiological

conditions.

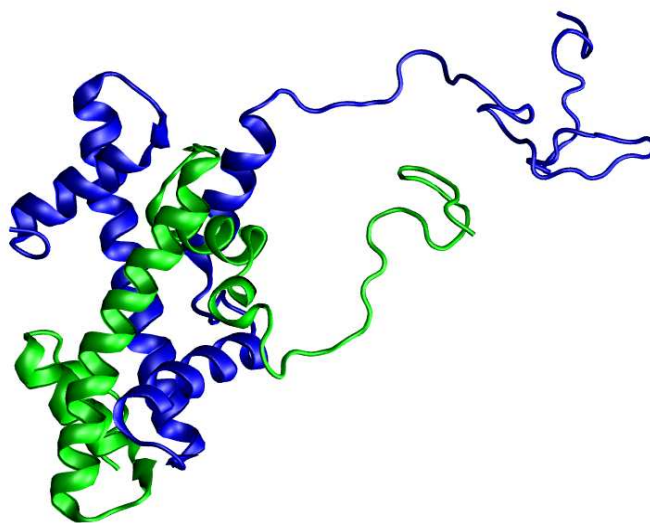


Figure 1.4: A H3 (*blue*) and a H4 (*green*) histone protein are represented forming a dimer via the handshake structural motif. Each histone protein is characterized by a globular histone domain consisting of 3 α -helices connected by loops and by a less structured histone tail region.

Histone tails

The histone tails have a high flexibility due to the absence of extensive structured α -helix formations, and may reach out far from the histone octamer. The tails contain a major part of the lysine and arginine amino acids of the histone protein, and are therefore highly positively charged. From the total of 220 lysine and arginine residues about 103 are located on the unfolded histone tails and about 117 residues are included in the globular histone domains [Khrapunov et al., 1997]. Although it is known that the removal of histone tails do not hinder the reconstitution of nucleosomes, they occupy critical functions in the nucleosome and for the higher-order structure. The functionalization of the tails is possible with the high positive charges on the tails, which interact with the negatively charged DNA or other proteins.

For example the role of the H4 histone tail is to mediate the interaction between different nucleosomes. The H3 tail positioned in proximity of the outgoing linker DNA arms screens the negative charge on the linker DNA. Consequently the H3 tail has a large influence on the entry-exit angle of the two linker DNA arms.

Of great interest is the fact that the N-terminal histone tails can be chemically modified by e.g. acetylation, methylation or phosphorylation. For the variety of modifications the precise role is still unknown, but is believed to influence e.g. the access

to DNA or the higher-order organization of DNA. As *in vivo* enzymes are responsible for these modifications, it opens the possibility of a regulation mechanism for the cell. Acetylation of the lysine residues at the N-terminal region of histone proteins as an example removes positive charges, thereby reducing the affinity between histones and DNA. RNA polymerase and transcription factors can then access the promoter region. Therefore histone acetylation enhances transcription while histone deacetylation represses transcription. The corresponding regulatory proteins for the histone acetylation is the histone acetyltransferase (HATs), while histone deacetylases catalyze the histone deacetylation.

An important consequence of posttranslational modifications of histones is the induced change of the histone core charge state. The modified total charge is reflected in the DNA-histone core interaction, which must be taken into account in the simulations of nucleosomes.

DNA in the nucleosome

The crystallographic data [Luger et al., 1997] shows that the DNA in the nucleosome structure makes a flat, left-handed superhelix around the histone core of about $1\frac{3}{4}$ turns. The pitch of the superhelix is about 2.39 nm. The histone fold domains account for the organization of 121 bp of DNA. The H3 α -helix extension and tails bind further 13 bp at each terminus of the superhelix. The superhelical path represents only an approximation, while in reality DNA shows sharper bends in some regions than in other positions on the histone core surface. Further the average DNA torsion in the nucleosome (10.2 bp per turn) deviates from the value observed in free solution (10.5 bp per turn), which follows from a geometric argument that a right-handed DNA double-helix is overwound by following a left-handed superhelix around the histone core. But the twist is also a local property on the exact DNA position in the nucleosome and reflects the interaction with specific DNA-histone core interaction sites.

A general attraction between DNA and the histone octamer is given by the consideration that a DNA stretch of ≈ 146 bp organized in the nucleosome corresponds to 292 negative charges, while the histone core has about ≈ 220 positive charges. In detail the DNA-histone interaction is established mainly between the phosphodiester backbone of the DNA and amino acids in the α -helices or the unstructured loops. The DNA is bound to interaction sites with the minor groove facing the histone core; in total as reported in [Luger et al., 1997, Davey et al., 2002] 14 binding sites between histones and DNA are found in the nucleosome. At the contact site a side-chain of an arginine residue can penetrate into the minor groove. Further the positive charge of the α -helix dipole interact with individual phosphate groups and at the interaction sites direct hydrogen bonds and indirect hydrogen bonds via a bridging water molecule establish the contact to the phosphate-sugar backbone.

A DNA sequence-dependent affinity to the histone core was shown by [Anderson and Widom, 2000]. DNA fragments which were prone to bending e.g. sequences containing many AT-base pairs, performed better in respect to the binding affinity than other naturally occurring sequences. Competitive nucleosomal reconstitution with artificial nucleosome-positioning sequences showed also an affinity for sequences with a helical

periodicity of 10.2 bp/turn [Shrader and Crothers, 1990].

Linker histone

Nuclease digestion of native chromatin showed also the existence of fragments of 166 bp length on intermediate time scales [Bednar et al., 1998]. The protection of the undigested DNA originates from the linker histone H1, which binds to the outgoing linker DNA. Hereby the immediate digestion of an additional 10 bp linker DNA at each side of the central 146 bp is sterically hindered by the linker histone. The structure containing the nucleosome core particle and linker histone with a total of ≈ 166 bp is referred to as chromatosome [Simpson, 1978].

Electron cyro microscopy images of the chromatosome show a stem-like motif with an asymmetrically positioned H1. It is known that linker histone H1 facilitates the compaction of nucleosome arrays [Clark and Kimura, 1990, Bednar et al., 1998] and the presence of H1 reduces the distance between the outgoing linker arms [Tóth et al., 2006]. This might involve the screening of the mutual repulsion of the linker DNA segments by the C-terminal tails of the linker histone.

From the nucleosome to chromatin

In eukaryotic cells DNA is organized into chromatin [van Holde, 1989]. As previously described, the nucleosome is the basic packing unit of DNA, but on larger length scale the nucleosomes are compacted into a chromatin fiber. In general the repeat length, the average base pair number per nucleosome, is in the range from 156 to more than 240 bp [van Holde, 1989]. At low salt conditions the nucleosome array exhibits an expanded structure as shown in Fig. (1.6b), which is termed beads-on-a-string. The array has a diameter of about 10 nm and has a zig-zag arrangement of nucleosomes. With increasing ionic strength the beads-on-a-string conformation undergoes a transition into a more compact fiber [Finch and Klug, 1976], the so-called 30 nm chromatin fiber. An electron microscope image of the chromatin fiber under physiological conditions is depicted in Fig. (1.6a). The actual chromatin structure is not known and a variety of models have been proposed for the spatial conformation of nucleosomes inside the chromatin fiber. The two most prominent models are the solenoid model and the zig-zag model. In the solenoid model proposed by Klug et al. the nucleosomes are arranged on one single solenoid helix, while in the competing zig-zag model the adjacent nucleosomes are positioned on two helices. In the latter model straight DNA linkers connect neighboring nucleosomes, while the former model requires bent linkers, which are energetically unfavorable. Although no chromatin model can be excluded and a considerable heterogeneity is likely to exist in the higher order structures of chromatin [Wolffe, 1995], indications for the zig-zag conformation at physiological conditions are present. According to Ref. [Bednar et al., 1998] the zig-zag structure, confirmed at low salt, persists also at higher salt without transition to a solenoid arrangement of the nucleosomes. Scanning force microscopy yielded images of an irregular zig-zag [Leuba et al., 1994, Zlatanova et al., 1998] and a tetranucleosome structure has been resolved in X-ray crystallography, which is in agreement with straight linkers of the zig-zag model [Schalch et al., 2005].

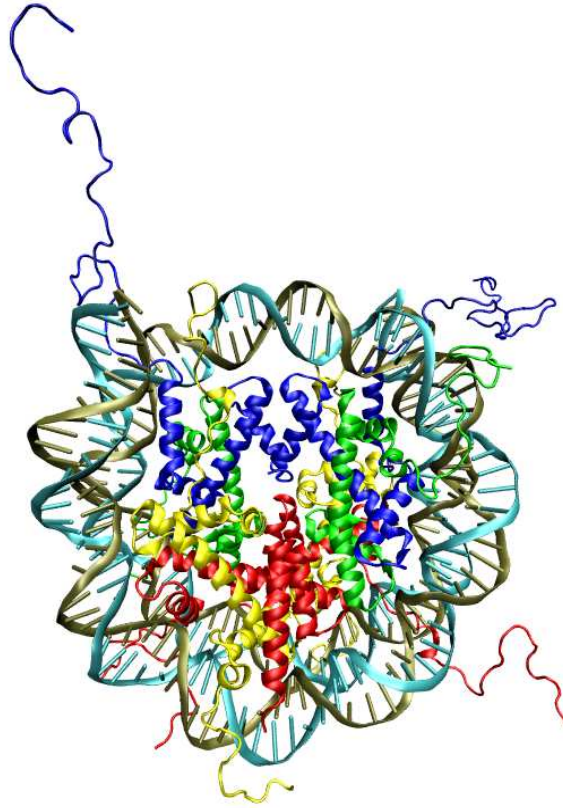


Figure 1.5: Ribbon diagram of the nucleosome core particle showing 146 bp DNA phosphodiester backbone and eight histone proteins based on X-ray crystallographic data of the 1KX5 structure. The histone core is formed by two of each H2A (*yellow*), H2B (*red*), H3 (*blue*) and H4 (*green*) histone proteins.

In recent years measurements with single molecule manipulation techniques such as optical tweezers or atomic force microscopy allowed to exert forces on chromatin fibers. The response to mechanical stress allows to probe the interaction strength between individual nucleosomes. Stretching experiments of a native chromatin fiber isolated from chicken erythrocytes have been performed [Cui and Bustamante, 2000]. The value of the internucleosomal attractive energy estimated from the force-extension curves at physiological ionic strength is about $\approx 3.4 k_B T$. Recent force spectroscopy of nucleosome arrays reconstituted with recombinant histones reported even an nucleosome-nucleosome interaction energy in the range of $10 k_B T$ to $16 k_B T$ [Kruithof et al., 2008].

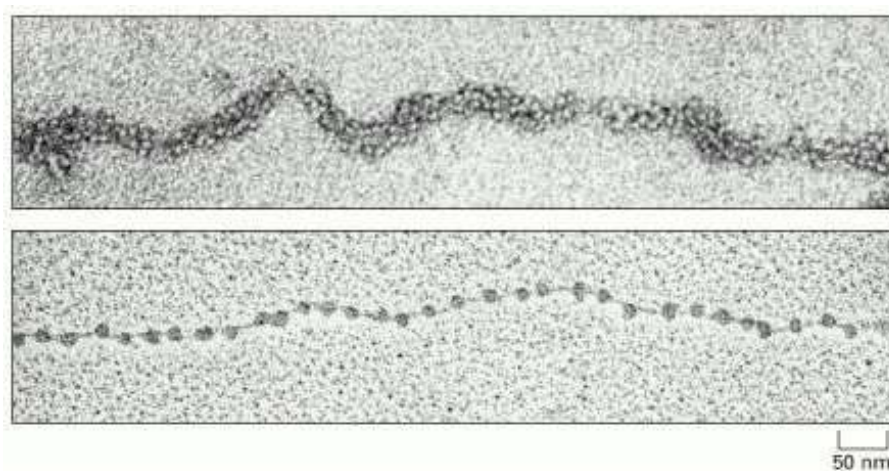


Figure 1.6: (a) Chromatin isolated directly from an interphase nucleus appears in the electron microscope as a fiber of 30 nm diameter. (b) Individual nucleosomes are visible at low salt conditions in a bead-on-a-string structure. (Adopted from [Alberts et al., 2002]).

Nucleosome dynamics

DNA inside the nucleosome is sterically occluded, which creates obstacles for many DNA-binding proteins. But the nucleosome is not a static entity but exhibits a highly dynamic behavior. Sometimes the unwrapping of DNA or translocation of nucleosomes is the result of ATP-dependent nucleosome remodeling factors [Muchardt and Yaniv, 1999]. The problem remains as the remodeling factors require site-specific DNA-binding proteins, which in turn have to gain access to nucleosomal DNA. But energy in form of ATP is not always necessary, because as confirmed in experiments thermal fluctuations are sufficient for the accessibility of target sites within the nucleosome by regulatory proteins [Polach and Widom, 1995, Anderson and Widom, 2000]. More direct measurements with the Fluorescence Resonance Energy Transfer technique showed that nucleosomes undergo conformational fluctuations spontaneously, in which a stretch of DNA transiently lifts off the histone octamer surface [Koopmans et al., 2007, Li et al., 2005, Tomschik et al., 2005, Gansen et al., 2009].

The nucleosome dynamics is determined by the interaction energy of DNA and the histone core, but no reliable quantitative estimates of the binding energy are available. Based on the accessibility of target sites in the restriction enzyme assays [Polach and Widom, 1995, Anderson and Widom, 2000], Schiessel proposed a binding energy of a few $k_B T$ per contact site [Schiessel, 2003], which is nearly in balance with bending energy required to wrap the DNA around the histone core. In the calculation the mutual repulsion of the DNA strands is not taken into account, therefore the total mean binding energies are higher. Analytical models which explicitly include electrostatic interactions between DNA-DNA, DNA-histone core and bending energy result in significantly higher binding energies [Kunze and Netz, 2000, 2002, Arcesi et al., 2007].

Stretching experiments are also a useful tool to obtain detailed information on the DNA-histone core interaction in individual nucleosomes. The technique allows to investigate the transition to the nucleosome, completely unwrapped from DNA. In this class of experiments a high energetic barrier of about $\approx 20 - 38 K_B T$, stabilizing the unwrapping of the inner DNA turn, was revealed [Brower-Toland et al., 2002, Pope et al., 2005]. A part of this work deals with the simulation of nucleosome unwrapping under external force. A goal is to relate the simulated unwrapping transitions to experiments and obtain estimates on the binding energies.

The stretching experiments are also of interest from a biological point of view as it is known that DNA and RNA polymerases can exert transiently considerable forces (and torques) of about ≈ 40 pN [Yin et al., 1995, Davenport et al., 2000, Forde et al., 2002]. This may allow to open the nucleosome structure and transcribe nucleosomal DNA.

Chapter 2

Theoretical concepts

In this chapter a basic introduction to polymer physics is given. A comprehensive review on this topic can be found in [Rubinstein and Colby, 2003, Flory, 1988, Doi and Edwards, 1986]. The presented polymer models set the framework for the subsequent description of the polymer dynamics and the employed DNA model in the simulation, which will be presented in the next chapter.

The next part gives an overview on single-molecule force spectroscopy. A summary of analytical methods is provided, which allow to obtain relevant parameters e.g. kinetic rates from Dynamic Force Spectroscopy (DFS).

2.1 Polymer theory

2.1.1 Ideal chain models

Chain models play a prominent role in polymer physics. In the most simplest representation of real polymers, a chain of immaterial segments is assumed. Chain models are termed ideal, when interactions between segments, which are separated by a large distance, are ignored. Although in real polymers long-range interactions are present e.g. as excluded volume interaction, polymers can be treated also as ideal under certain conditions. Despite their simplicity ideal chain models capture already basic physical polymer properties and provide a good starting point for the description of polymers.

Freely jointed chain and freely rotating chain model

A simple model for a polymer is the freely jointed chain. In this model the chain consists of N straight segments \vec{s}_i of fixed length l_0 in linear succession, which are freely rotating at their joints. The total contour length of the polymer is then defined as $L_c = Nl_0$. An important observable of a polymer is the end-to-end vector, which is given by the sum of the segment vectors $\vec{R} = \sum_{i=1}^N \vec{s}_i$. Since no preferred directions of the segments exist and the path of the polymer represents a 3-dimensional random walk, the ensemble average of the chain end-to-end distance is zero. A second important observable of a polymer characterizing the size is the second moment $\langle R^2 \rangle$ of the end-to-end distance distribution. No correlations exist between different segments ($\langle \vec{s}_i \vec{s}_j \rangle =$

δ_{ij}) and therefore the mean-square end-to-end distance is

$$\langle R^2 \rangle = \sum_{i=1}^N \sum_{j=1}^N \langle \vec{s}_i \vec{s}_j \rangle = \sum_{i=1}^N \langle s_i^2 \rangle + 2 \sum_{i=1}^N \sum_{\substack{j=1 \\ i < j}}^N \langle \vec{s}_i \vec{s}_j \rangle = Nl_0^2. \quad (2.1)$$

Besides the freely jointed chain different models exist which take into account restrictions in the bending angle and the internal rotation angle between neighboring segments due to the underlying chemical structure of real polymers. One of these models is the freely rotating chain. Here it is assumed that the bond angles $\{\beta_i\}$ between adjacent segments at the joints are fixed to a constant angle β , while allowing free rotation of the torsion angle $\{\phi_i\}$ around the axis. The direction of the rotation axis is defined by the neighboring segment. All torsion angles are equally likely and independent of each other. The fixing of the bond angle imposes now correlations between the segment vectors \vec{s}_i and \vec{s}_j

$$\langle \vec{s}_i \vec{s}_j \rangle = l_0^2 (\cos \beta)^{|j-i|}, \quad (2.2)$$

and results in the following second moment of the end-to-end distribution

$$\langle R^2 \rangle = Nl_0^2 \frac{1 + \cos \beta}{1 - \cos \beta} \quad (2.3)$$

for the freely rotating chain.

The flexibility of any real polymer with no long-range interactions can be characterized by treating the macromolecule effectively as a freely jointed chain. The equivalent chain is a freely jointed chain with N segments and an effective segment length B , but it has the same experimentally accessible properties of the actual polymer, such as the same radius of gyration $\langle R^2 \rangle$ and the same contour length. The effective segment length B of the equivalent freely jointed chain is termed Kuhn length and gives a measure of the polymer flexibility. In any ideal polymer chain the correlations between segments separated by a sufficiently large distance along the contour vanish. In this case the freely jointed chain model with an appropriately chosen Kuhn length can be applied to the real polymer.

Worm-like chain model

The worm-like chain (or Kratky-Porod model) is used to represent semi-flexible polymers. In contrast to the presented models consisting of rigid segments, the flexibility of the polymer is distributed continuously along the chain contour. It can also be regarded as a special case of a freely rotating chain in the limit of small bond angles β , while keeping the ratio l_0/β^2 and the chain contour length constant. This relation between the freely rotating chain and worm-like chain will become insightful in the next chapter 3, when the DNA model is introduced. The path of a polymer $\vec{r}(s)$ in space with contour length L_c can be parameterized with the distance $s \in [0, L_c]$ along the contour of the polymer. At each point of the chain a tangent vector $\vec{u}(s) = \partial \vec{r} / \partial s$

pointing in the chain direction can be defined. The flexibility of the polymer is taken into account with a bending energy $E^{(b)}$ proportional to the square of the curvature $\partial \vec{u}/\partial s$:

$$E^{(b)} = \frac{\kappa}{2} \int_0^{L_c} ds \left(\frac{\partial \vec{u}}{\partial s} \right)^2. \quad (2.4)$$

Here the bending rigidity κ defines the polymer stiffness. It can be shown that the correlation function of the cosines between the tangential vector decays exponentially along the contour

$$\langle \vec{u}(s) \vec{u}(0) \rangle = \exp \left(-\frac{s}{l_p} \right). \quad (2.5)$$

The persistence length l_p is the correlation length of the decay and gives another measure of the polymer flexibility. It is directly related to the bending rigidity (an intrinsic property of the polymer) via $\kappa = k_B T l_p$. The spatial size of the polymer coil is likewise measured with the mean-square distance, which is in the worm-like chain model given by

$$\langle R^2 \rangle = 2l_p \left(L_c - l_p \left(1 - \exp \left(-\frac{L_c}{l_p} \right) \right) \right). \quad (2.6)$$

In the limit of chains that are long compared to their persistence length $L_c \gg l_p$, one obtains then $\langle R^2 \rangle \approx 2l_p L_c$. The worm-like chain model also recovers the properties of a freely jointed chain with a Kuhn length B twice the persistence length l_p in the limit of long chains.

The importance of the worm-like chain model in biophysics is due to its good representation of semi-flexible biopolymers. The fact that especially double-stranded DNA can be modeled as a worm-like chain yielding good approximations for the conformational statistics, will be used in this work.

Gaussian chain model

All presented chain models have no long-range interactions but excluded volume, and furthermore all interactions are local. Therefore it is possible to divide the chain into N individual segments at the points s_0, \dots, s_N , which are statistically independent from each other. Then the probability $P(\vec{r}(s_0), \dots, \vec{r}(s_N))$ of a polymer to adopt a conformation, specified by the spatial positions of the points $\vec{r}(s_0), \dots, \vec{r}(s_N)$ can then be represented as a product of the conditional probabilities $g(\vec{r}(s_i), \vec{r}(s_{i+1}))$ of finding the end of the i th segment at the point $\vec{r}(s_i)$, provided that the $(i-1)$ th segment ended at the point $\vec{r}(s_i)$. The general class with the stated properties is called Markov chains, which encompasses the class of ideal chains. For this class of models it has been shown that if the separation between two points $\vec{r}(s_i)$ and $\vec{r}(s_{i+1})$ on the contour exceeds a Kuhn length, the distribution of distances between these points is Gaussian

$$g(\vec{r}(s_i), \vec{r}(s_{i+1})) = \left(\frac{3}{2\pi a^2} \right)^{\frac{3}{2}} \exp \left(-\frac{3(\vec{r}(s_i) - \vec{r}(s_{i+1}))^2}{2a^2} \right). \quad (2.7)$$

In the Gaussian chain model the points $\{\vec{r}_i\}$ can be envisioned as beads, which are connected by springs to maintain the linear connectivity of the polymer. The parameter a hereby denotes the root-mean-square distance between neighboring beads. The Gaussian distribution of neighboring beads allows to assign an interaction energy to each spring connecting adjacent beads

$$U_{i,i+1} = -k_B T \sum_{i=0}^{N-1} \ln g(\vec{r}(s_i), \vec{r}(s_{i+1})). \quad (2.8)$$

The polymer properties on the large scale, e.g. as the end-to-end distance $\langle R^2 \rangle = Na^2$, are independent of the local structure of a chain. With an appropriate choice of the parameter a , all large-scale properties of the Gaussian chain will coincide with any ideal polymer.

2.1.2 Polymer dynamics

Until now, only equilibrium properties of polymers have been considered. In the following we briefly review the standard models to describe dynamic properties e.g. the time-dependence of internal motion. The polymer models provide the framework for the verification and interpretation of the dynamic properties of the BD simulation.

Rouse model

The standard model to describe polymer dynamics without excluded volume interactions and topological constraints immersed in an immobile viscous medium is the Rouse model [Rouse, 1953]. The motion of the i th bead in a Gaussian chain as introduced in the preceding section is governed by the friction force of the solvent, the random force due to collisions with the surrounding solvent molecules and forces derived from the interaction energy between neighboring beads according to Eq. (2.8). In the continuous limit the equation of motion is reduced to a diffusion equation

$$\gamma \frac{\partial \vec{r}(s, t)}{\partial t} - \frac{3k_B T}{a^2} \frac{\partial^2 \vec{r}(s, t)}{\partial s^2} = \vec{\Gamma}(s, t), \quad (2.9)$$

where γ denotes the friction coefficient, and $\vec{\Gamma}$ is the random force with zero mean and width $2k_B T \gamma$ to which each bead is subject in the solvent. The transformation of the Rouse equation in Fourier space decomposes into a set of $k = 0, \dots, N$ independent equations for the Rouse modes $\psi_k^{(r)}$. The motion of a polymer chain can be represented as a superposition of the independent Rouse modes. Each Rouse mode is characterized by a relaxation time

$$\tau_k = \frac{N^2 a^2 \gamma}{3\pi^2 k_B T k^2}, \quad (2.10)$$

which sets the time scale on which the Rouse modes $\psi_k^{(k)}$ are uncorrelated. The mean-square displacement of a single bead is finally given by the following expression

$$\begin{aligned} \langle [\vec{r}(s, t) - \vec{r}(s, 0)]^2 \rangle &= \frac{6k_B T}{N\gamma} t + \\ &\quad \frac{4Na^2}{\pi^2} \sum_{k=1}^{\infty} \frac{1}{k^2} \cos^2 \left(\frac{\pi k s}{N} \right) \left[1 - \exp \left(-\frac{t}{\tau_k} \right) \right]. \end{aligned} \quad (2.11)$$

The first term on the right hand side covers the normal diffusive motion of the polymer coil. The diffusion coefficient is compared to a single bead reduced due to the friction of N beads in the polymer chain. For times $t \gg \tau_1$ the first term greatly exceeds the second, which describes the contributions to the mean-square displacement from the internal motion. In the limit $t \ll \tau_1$ the mean-square displacement grows as $\propto t^{1/2}$.

Zimm model

The Rouse model exhibits discrepancies with experimental results, which stem from the absence of hydrodynamic interactions. The Zimm model incorporates the perturbation of the surrounding solvent by the motion of the chain segments [Zimm, 1956]. Hydrodynamic interactions between the individual beads is treated on the level of the Oseen tensor.

The corresponding equation to Eq. (2.9) in the continous limit reads

$$6\pi\eta \frac{\partial \vec{r}(s, t)}{\partial t} = \int_0^{L_c} ds' \left\langle \frac{1}{|\vec{r}(s, t) - \vec{r}(s', t)|} \right\rangle \left(\frac{3k_B T}{a^2} \frac{\partial^2 \vec{r}(s', t)}{\partial s'^2} + \vec{\Gamma}(s', t) \right). \quad (2.12)$$

Hereby a preaveraging approximation of the Oseen tensor, which defines the hydrodynamic coupling, was performed. The Oseen tensor is averaged over the equilibrium distribution function $P(\vec{r}(s_0), \dots, \vec{r}_N)$ of the polymer (see Gaussian chain model in section (2.1.1)), as indicated by the brackets $\langle \rangle$. If off-diagonal elements of hydrodynamic tensor are neglected, the Zimm equation adopts the same structure as the Rouse model. Analogously the solution of the Zimm equation (2.12) can be represented in terms of Rouse modes $\psi_k^{(r)}$ with the corresponding relaxation times $\tilde{\tau}_k$ given by

$$\tilde{\tau}_k = \sqrt{\frac{3}{\pi}} \frac{\gamma}{k_B T} \left(\frac{Na^2}{k} \right)^{\frac{3}{2}}. \quad (2.13)$$

In the Zimm model the mean-square displacement follows a power law $\propto t^{2/3}$ in the limit $t \ll \tilde{\tau}_1$.

Dynamics of a Gaussian semiflexible chain

An analytical description of the dynamics of a Gaussian semiflexible chain has been given in the work of Harnau, Winkler, Reineker [Harnau et al., 1996]. Basically the polymer chain is a Gaussian chain represented as a continuous differential space curve

$\vec{r}(s, t)$ with the contour coordinate s along the contour length. Firstly a Gaussian semiflexible chain is characterized by a Gaussian distribution function of the distances between two points along the chain contour as defined in section (2.1.1). As a second property bending is energetically penalized. The same expression (2.4) for the elastic energy as in the worm-like chain is hereby used in order to incorporate the effect of chain rigidity.

The resulting equation of motion of the Gaussian semiflexible polymer including hydrodynamic interactions is given by the following Langevin equation

$$\frac{\partial \vec{r}(s, t)}{\partial t} = \int_{-L_c/2}^{L_c/2} \mathbf{D}(s, s') \left[2\nu k_B T \frac{\partial^2 \vec{r}(s', t)}{\partial s'^2} - \epsilon k_B T \frac{\partial^4 \vec{r}(s', t)}{\partial s'^4} + \vec{\Gamma}(s', t) \right] ds' \quad (2.14)$$

with free-end boundary conditions. The factor $\epsilon = 3l_p/2$ is related to the bending energy, while $\nu = 3/4l_p$ is associated with the chain stretching flexibility. As before a stochastic, Gaussian force $\vec{\Gamma}(s, t)$ with zero mean is added due to the surrounding solvent. Hydrodynamic interactions are taken into account on the level of a preaveraged Rotne-Prager tensor $\mathbf{D}(s, s')$ [Rotne and Prager, 1969] obtained by averaging over the equilibrium polymer conformations

$$\begin{aligned} \mathbf{D}(s, s') &= \frac{1}{3\pi\eta} \mathbf{I} [\delta(s - s') + Q(s - s')] \\ Q(s - s') &= \Theta(|s - s'| - d) \sqrt{\frac{3}{2\pi \langle [\vec{r}(s) - \vec{r}(s')]^2 \rangle}} \\ &\quad \exp\left(-\frac{3d^2}{2 \langle [\vec{r}(s) - \vec{r}(s')]^2 \rangle}\right). \end{aligned} \quad (2.15)$$

The first term represents the local friction, while the Heaviside step function accounts for the excluded volume of the chain with thickness d . The equation of motion (2.14) can be solved by a normal mode analysis, expanding the equation in terms of the eigenfunctions $\psi_k(s)$ with the eigenvalues ξ_k :

$$\begin{aligned} \psi_0(s) &= \sqrt{\frac{1}{L_c}} \\ \psi_k(s) &= \sqrt{\frac{A_k}{L_c}} \left(\alpha_k \frac{\sin(\alpha_k s)}{\cos(\alpha_k L_c/2)} + \beta_k \frac{\sinh(\beta_k s)}{\cosh(\beta_k L_c/2)} \right), \quad k \text{ odd} \\ \psi_k(s) &= \sqrt{\frac{A_k}{L_c}} \left(-\alpha_k \frac{\cos(\alpha_k s)}{\sin(\alpha_k L_c/2)} + \beta_k \frac{\cosh(\beta_k s)}{\sinh(\beta_k L_c/2)} \right), \quad k \text{ even} \end{aligned} \quad (2.16)$$

with

$$\beta_k^2 - \alpha_k^2 = 2\nu/\epsilon, \quad \xi_0 = 0, \quad \xi_k = \epsilon\alpha_k^4 + 2\nu\alpha_k^2. \quad (2.17)$$

The constants α_k and β_k can be determined from the boundary conditions, while the A_k are normalization constants. The relaxation times τ_k of the chain in the free draining

limit can be expressed by the eigenvalues of the eigenvalue equation: $\tau_k = 3\pi\eta/\xi_k$. The relaxation times $\tilde{\tau}_k$ in the presence of hydrodynamic interactions are given by the matrix elements of $Q(s-s')$ in terms of the eigenfunctions $\psi_k(s)$

$$\tilde{\tau}_k = \frac{\tau_k}{1 + \langle \psi_k(s) | Q(s-s') | \psi_k(s) \rangle}. \quad (2.18)$$

Finally the dynamics of the internal motion relative to the motion of the center-of-mass \vec{r}_{cm} can be expressed as

$$\begin{aligned} \langle \vec{r}_{\text{rel}}^2(t) \rangle &= \langle [\vec{r}(s, t) - \vec{r}_{\text{cm}}(t) - \vec{r}(s, 0) - \vec{r}_{\text{cm}}(0)]^2 \rangle \\ &= \frac{2k_B T}{\pi\eta} \sum_{k=1}^{\infty} \tau_k \psi_k^2(s) \left(1 - \exp\left(-\frac{t}{\tilde{\tau}_k}\right) \right). \end{aligned} \quad (2.19)$$

The theory yields in the limit of a stiff chain $l_p \gg L_c$, in which only bending modes contribute and stretching modes can be neglected, that the internal motion is reduced to a power law $\langle \vec{r}_{\text{rel}}^2(t) \rangle \propto t^{-3/4}$. A similar power law was derived in [Kroy and Frey, 1997]. The opposite limit $l_p \ll L_c$ of a flexible chain recovers the result of the Zimm model.

2.1.3 Twisting motion in the Barkley-Zimm model

The double helical structure of DNA allows also torsional motions besides stretching and bending of the molecule. On the simplest level a description of torsion in DNA can be given considering a thin, uniform rod of length L_c , which can perform torsional deformation along the long axis, as done in [Barkley and Zimm, 1979]. Hydrodynamic interactions have been neglected due to the small perturbations of the surrounding viscous fluid in the case of twisting. If $\gamma(s, t)$ describes the relative rotation angle of two rod cross sections, then the equation of motion for twisting reads

$$\frac{\partial \gamma}{\partial t} = \frac{C}{\rho} \frac{\partial^2 \gamma}{\partial s^2}, \quad (2.20)$$

where ρ is the frictional coefficient per unit length, and the related diffusion coefficient $D = k_B T / \rho$. For a circular cylinder with a hydrodynamic radius of r_{HD} the frictional coefficient per unit length can be given by $\rho = 4\pi\eta r_{\text{HD}}^2$. Assuming the torsional deformations to obey Hooke's law, the elastic energy of this twisted rod is given by

$$E^{(t)} = \frac{C}{2} \int_{-L_c/2}^{L_c/2} ds \left(\frac{\partial \gamma}{\partial s} \right)^2. \quad (2.21)$$

We are interested in the temporal evolution of the rotation angle $\gamma(t)$ at the center position of the cylinder, when at the initial conditions at time $t = 0$ the rotation angle is γ_0 and the rod is in thermal equilibrium. For this case in [Barkley and Zimm, 1979] the time distribution $\psi(\gamma, t | \gamma_0, 0)$ of the rotation angle γ with the initial rotation angle γ_0 has been calculated:

$$\psi(\gamma, t | \gamma_0, 0) = \frac{1}{\sqrt{\pi\Gamma(t)}} \exp\left(-\frac{(\gamma - \gamma_0)^2}{\Gamma(t)}\right), \quad (2.22)$$

where the twisting decay function is

$$\Gamma(t) = \frac{4Dt}{L_c} + \frac{8D}{\sigma L_c} \sum_{k=1}^{\infty} \frac{1 - \exp(-\sigma \lambda_k^2 t)}{\lambda_k^2}, \quad (2.23)$$

with $\lambda_k = 2k\pi/L$, $k \in \mathbb{N}$ and $\sigma = C/\rho$. Barkley and Zimm showed that the elastic model of DNA is formally equivalent to a bead model, where the adjacent beads are coupled by harmonic potentials [Allison and Schurr, 1979].

2.2 Single-molecule force spectroscopy

A major focus of this work lies on conformational changes in nucleosomes. The application of an external force may induce such changes and facilitate the transition between different conformational nucleosome states. Since the typical time scale of transition is shifted by an external force to smaller time scales, which are accessible in computer simulations, it allows to study the transitions numerically. An analogous experimental tool is single-molecule force spectroscopy, which makes it possible to probe forces and motions associated with biological molecules or actively exert forces. Molecular-scale forces play a key role in all biological processes like DNA replication, cellular motility or protein motors as kinesin and myosin. Different experimental realizations of force spectroscopy exist e.g. optical tweezers, magnetic tweezers, atomic force microscopy (AFM), micro-needle manipulation and flow-induced stretching, but the principle idea remains the same in every case. In general one end of the investigated molecule is fixed onto a surface, while the other end is attached to a probe. For instance specific binding between probe and surface is realized with ligand-receptor pairs such as biotin-avidin or antibody-antigen pairs such as digoxigenin and anti-digoxigenin. The extension of the molecule is determined from the anchoring point on the surface relative to the position of the probe, which is monitored in the experiment. The probe can be approximated by a linear spring with a certain spring stiffness k_{eff} , which allows to determine the force from Hooke's law ($F = -k_{\text{eff}}x$). Therefore the measurement of the deviation x from the equilibrium position of the probe yields the acting force on the molecule.

In an optical tweezer experimental setup the molecule is attached to a dielectric sphere, which experience a restoring force due to the interaction of the induced dipole with the gradient of the electrical field in the laser beam focus [Ashkin et al., 1986]. Within a certain range the restoring force is linear to the displacement from the equilibrium position. A typical setup of an optical tweezer experiment to measure forces is shown in Fig. (2.1).

Besides imaging of surfaces the AFM represents another technique which can be applied to force measurements. In AFM forces onto the attached molecule under study are transmitted with the tip of a cantilever, and sensed by deflection of the cantilever [Binnig et al., 1985].

With optical tweezers it is possible to manipulate and measure forces in the range from 0.1 pN up to 100 pN, while AFM covers slightly higher force scales from 10 pN to 10^4 pN due to the higher stiffness of the effective spring.

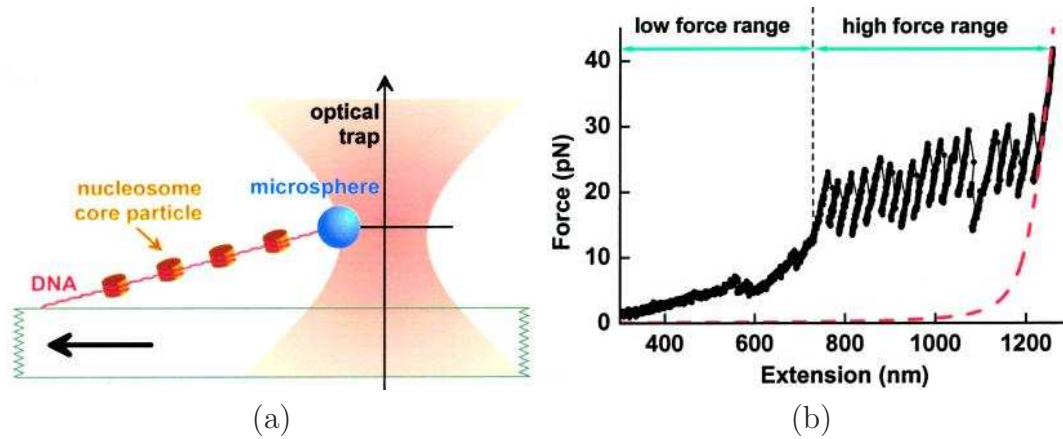


Figure 2.1: (a) Typical experimental setup for single-molecule force spectroscopy with optical tweezers. Here a nucleosomal array was stretched between the surface of a microscope coverslip and an optically trapped microsphere. (b) Force-extension curve of a nucleosomal array recorded with the optical tweezers setup. Adopted from [Brower-Toland et al., 2002]

A further extension of this technique is Dynamic Force Spectroscopy (DFS), which was pioneered by Evans et al. [Evans and Ritchie, 1997, 1999]. It represents a powerful tool to probe single molecules bonds in an adhesion complex. In DFS experiments, a bond is driven away from its equilibrium by pulling a spring at a constant velocity. Eventual rupture of the bond occurs by escape from the bound state over an energy barrier. The analysis of the rupture force spectrum, the peak force measured during pulling, yields information about the molecular energy landscape and adhesion strength of the complex. The detailed analytical methods needed to extract the relevant quantities is described in the following sections (2.2.1) and (2.2.1).

Besides the mode in which the molecule is stretched with a constant velocity, the measurements may be conducted at a constant force exerted on the molecule. A constant force during measurements is achieved by a dynamic feed-back loop of the exerted force to the displacement of the probe.

New applications for DFS has been recently possible with the work of Jarzynski [Jarzynski, 1997b,a]. The Jarzynski equation gives the free energy difference of two equilibrium states in terms of an ensemble of the irreversible work performed along the path connecting the two states. As has been demonstrated [Hummer and Szabo, 2001] free energy surfaces can therefore be reconstructed from repeated pulling experiments.

We further remark that DFS as a single-molecule technique may resolve transient or multiple configurational states, which otherwise could not be obtained with ensemble average in bulk measurements.

2.2.1 Phenomenological model of the rupture kinetics

In order to extract information about kinetics and energy landscapes from single-molecule pulling experiments, several methods have been developed to analyze the

experimental data. In its simplest form Bell [Bell, 1978] proposed a model for the bond dissociation rate between a ligand and its receptor. The dissociation of two particles (receptor and ligand) can be understood as a diffusive motion out of an energy well $U(x)$, which represents the interaction energy of one particle separated with a distance x from the second particle. At the absence of an external force, an energy barrier $E_b = U(x_+^0) - U(x_-^0)$ between the meta stable minimum at the distance x_-^0 and the barrier at x_+^0 prevents escaping from the energy well. The potential is characterized by the reaction distance between the energy minimum and the energy barrier $d = x_+^0 - x_-^0$. A schematic energy well potential showing the relevant properties is depicted in Fig. (2.2a). In the limit of large energy barriers compared to the thermal energy $E_b \gg k_B T$, the escape rate is related to the energy barrier according to the Kramers theory [Kramers, 1940, Hänggi et al., 1990]:

$$k_{\text{off}} = k_0 \exp\left(-\frac{E_b}{k_B T}\right). \quad (2.24)$$

One obtains an Arrhenius-like dependence of the escape rate, where the intrinsic escape rate $k_0 = \omega_- \omega_+ / 2\pi\gamma$ is defined by the curvatures $M\omega_{\pm}^2$ of the potential $U(x)$ at the extremal points. In this kinetic limit the escape occurs due to thermal fluctuations.

The application of a constant external force F onto one particle, derived from a potential $V(x) = -Fx$ corresponds to an effective potential $U(x) - Fx$, in which the particle moves. The external force shifts the energy minimum x_-^0 and maximum x_+^0 to new positions $x_-(F)$ and $x_+(F)$ and under external force the energy barrier E_b becomes $E_b(F) = U(x_+) - U(x_-) - Fd$. The critical force F_c is defined as the external force at which the energy barrier vanishes. For small forces in relation to the critical force $F \ll F_c$ the potential is only minimally perturbed and therefore the positions of the energy minima and maxima are only slightly shifted. Consequently, the energy barrier E_b is reduced in approximation by a linear term $-Fd$. Under this assumptions the critical force adopts a value of E_b/d . As a consequence the rate of rupture $\tilde{k}(t)$ scales with the exponential of the applied force in the phenomenological theory:

$$\tilde{k}(t) = k_{\text{off}} \exp\left(\frac{F(t)d}{k_B T}\right). \quad (2.25)$$

Here k_{off} denotes the rate constant for bond disruption under zero external force as indicated by Eq. (2.24). Further the external force is generalized to be a function of time. The application of an external force facilitates the transition beyond the energy barrier. The tilting of the potential due to the application of an external force is shown in Fig. (2.2b).

The ansatz implies that the transition of the system can be represented by a 1-dimensional reaction coordinate x by projection of the entire dynamics onto a single reaction coordinate. Further the escape rate along the reaction coordinate should also yield the intrinsic dissociation rate. The approach is valid if the relaxation times of the other degrees of freedom are smaller than the time scale associated with the dynamics along the reaction coordinate.

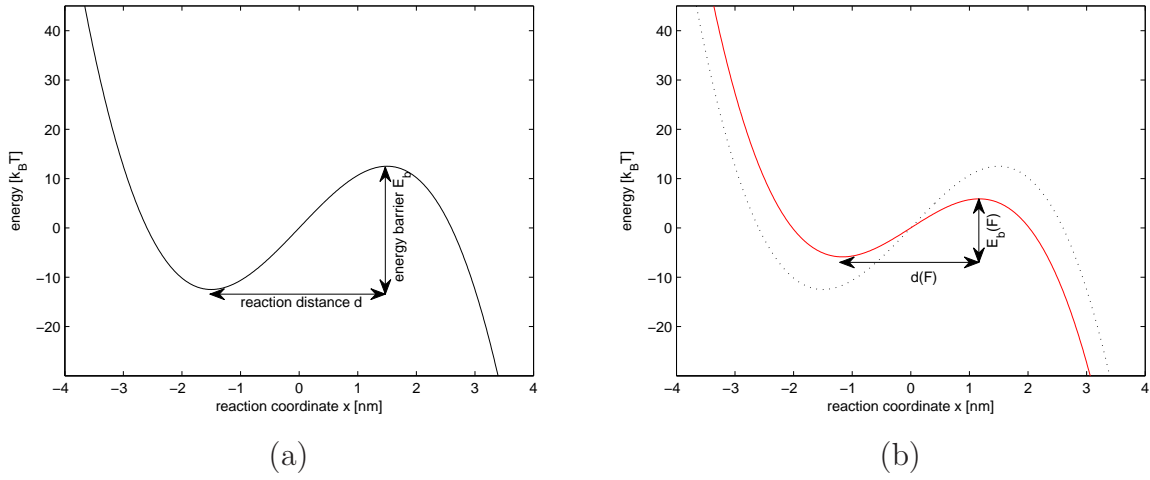


Figure 2.2: Schematic representation of a 1-dimensional energy surface with a single energy well. (a) Energy surface with the energy barrier E_b and a reaction distance d between energy minimum and energy barrier at zero external force. (b) Combined energy surface $U(x) - Fx$ at an external force F . The energy barrier $E_b(F)$ decreases with increasing external force F .

If the transition to the unbound state is assumed to be irreversible beyond the energy barrier, the process can be described simply by a first order kinetic reaction

$$\frac{dS(t)}{dt} = -\tilde{k}(t) S(t) \quad (2.26)$$

$$S(t) = \exp\left(-\int_0^t \tilde{k}(t') dt'\right). \quad (2.27)$$

The probability of the system to be in a state where the transition has not occurred yet is denoted by $S(t)$.

The transition times are distributed as $-\dot{S}(t) dt$, which is in relation to the probability distribution of forces $F(t)$. Then the following equation holds true: $P(F) dF = -\dot{S}(t) dt$.

In typical DFS experiments the force is a linear function of time $F(t) = r_f t$ with the force loading rate r_f . Changing the variable of integration from time t to the force $F(t)$, the probability distribution of forces is then given by

$$P(F) = \frac{k(F)}{r_f} \exp\left(-\frac{1}{r_f} \int_0^F k(F') dF'\right). \quad (2.28)$$

From the knowledge of the force distribution (2.28) Gergely et al. derived the mean rupture force $\langle F \rangle$ as a function of the force loading rate r_f [Gergely et al., 2000]. In the slow pulling regime $\langle F \rangle \ll F_c$ or correspondingly small forces, Bell's escape rate (2.25) is applicable, yielding the expression

$$\langle F \rangle = \int_0^\infty F' P(F') dF' = \frac{k_B T}{d} \exp\left(\frac{k_B T k_{\text{off}}}{dr_f}\right) E_1\left(\frac{k_B T k_{\text{off}}}{dr_f}\right) \quad (2.29)$$

with the exponential integral $E_1(z) = \int_z^\infty \exp(-t) t^{-1} dt$ [Abramowitz and Stegun, 1970]. If the loading rates r_f are sufficiently high, such that the energy barrier is affected by the pulling in the bond life time k_{off}^{-1} without external force or equivalently $k_B T \ll dr_f/k_{\text{off}}$ holds true, the expression (2.29) can be reduced to

$$\langle F \rangle = \frac{k_B T}{d} \left[\ln(r_f) - \ln\left(\frac{k_B T k_{\text{off}}}{d}\right) - \gamma \right], \quad (2.30)$$

Here $\gamma = 0.5772\dots$ denotes the Euler-Mascheroni constant. In this regime the rupture force is a linear function of the logarithm of the force loading rate $\langle F \rangle \propto \ln(r_f)$. In experiments often the most probable rupture force is determined. The most probable rupture force F^* can be calculated from the derivative of the rupture force distribution:

$$\left. \frac{\partial P(F)}{\partial F} \right|_{F=F^*} = 0 \quad (2.31)$$

$$F^* = \frac{k_B T}{d} \left(\ln r_f - \ln\left(\frac{k_B T k_{\text{off}}}{d}\right) \right) = \langle F \rangle + \frac{k_B T \gamma}{d} \quad (2.32)$$

We note that the most probable rupture force is shifted with respect to the mean rupture force by a constant term.

The analysis of the rupture forces yields therefore information about the energy landscape along the transition pathway.

2.2.2 Model-dependent description of the rupture kinetics

Another class for the description of the kinetics facilitated by external force uses a defined model potential, while in the phenomenological approach only the reaction distance as an independent parameter characterizes the energy surface. Further it accounts explicitly for the perturbation of the potential in the presence of an applied force field. Kurkijärvi has been the first to employ the method in the context of solid-state physics [Kurkijärvi, 1972], and later it has been analyzed more profoundly by Garg [Garg, 1995]. But Dudko et al. were the first, who applied the method in the context of single-molecule DFS [Dudko et al., 2003, 2006].

The main argumentation of Garg's formalism is as follows. Due to the exponential dependence of the escape rate on the external force, the escape probability increases disproportionately high with rising force. Close to the critical force F_c or equivalently $1 - F/F_c \ll 1$ the energy barrier disappears and therefore the majority of escapes from the potential well occurs in this force range. Further it is assumed that for this case all smooth surfaces can be well represented by a cubic polynomial. As the extremal positions x_\pm are near the inflection point x_c , the energy surface can be expanded around x_c , yielding an approximation of the potential up to the third order

$$U(x) \approx U(x_c) + F_c(x - x_c) + \frac{U'''(x_c)}{6}(x - x_c)^3. \quad (2.33)$$

The energy extremal positions for the combined potential $U(x) - Fx$ are then given by

$$x_{\pm} = x_c \pm \sqrt{-\frac{2F_c}{U'''(x_c)}} \sqrt{1 - \frac{F}{F_c}}. \quad (2.34)$$

In this high force limit the energy barrier $E_b(F)$ scales with the external force as

$$E_b(F) = E_b \left(1 - \frac{F}{F_c}\right)^{\frac{3}{2}} \quad (2.35)$$

$$E_b = \frac{2}{3} \frac{(2U'_0)^{\frac{3}{2}}}{(-U''')^{\frac{1}{2}}}. \quad (2.36)$$

The approximating linear-cubic of the energy surface in the vicinity of the critical force can be denoted as

$$U(x) = \frac{3}{2} E_b \left(\frac{x}{d}\right) - 2E_b \left(\frac{x}{d}\right)^3, \quad (2.37)$$

in agreement with the preceding definitions. In order to derive the escape rate $k(F)$ of the combined potential $U(x) - Fx$, one can make use of Kramers theory of thermally activated escape [Kramers, 1940] (see Eq. 5.5). In a second step, if a constant force loading rate r_f is assumed, the escape rate allows to obtain the distribution of rupture forces $P_1(F)$ (see Eq. (5.6)) according to the integral in Eq. (2.28). As in the preceding section for the phenomenological model, Eq. (2.29) then defines the mean rupture force and carrying out the integration one obtains

$$\langle F \rangle = \frac{E_b}{\nu d} \left(1 - \left(\frac{1}{E_b} \ln \frac{k_{\text{off}} \exp(E_b + \gamma)}{d r_f}\right)^{\nu}\right). \quad (2.38)$$

For a linear-cubic energy surface the parameter ν equals a value $2/3$. The variance of the rupture force σ_F^2 is given by

$$\sigma_F^2 = \frac{\pi^2}{6 d^2} \left[\frac{1}{E_b} \ln \frac{k_{\text{off}} \exp(E_b + \tilde{\gamma})}{d r_f} \right]^{2\nu-2}. \quad (2.39)$$

Here $\tilde{\gamma}$ has approximately a numerical value of 1.064. In the fast pulling regime the rupture force scales with $\langle F \rangle \propto \ln(r_f)^{3/2}$. It should be remarked that the variance of the rupture force is also a function of the force loading rate. In contrast to the phenomenological model the variance is independent on r_f .

In the limit of very high forces $F > F_c$ the energy barrier vanishes. Thermal fluctuations do not contribute significantly to the escape rate compared to mechanical pulling. This represents the mechanical limit of force facilitated escape from an energy well potential.

Chapter 3

Model and Methods

In this work numerical simulations were used to assess the dynamics of DNA and DNA/protein complexes. Since the dynamics involves relative long time and length scales, we focused on the most important physical features of the system and disregarded degrees of freedom that are not relevant on the scales of interest. The coarse-grained simulations are based on the program package *corchy++* developed by K.Klenin et al., which has been already successfully applied to a number of problems [Merlitz et al., 1998, Klenin and Langowski, 2004]. The chapter is subdivided in a part presenting the DNA model, a description of the nucleosome model and the used Brownian dynamics algorithm. Subsequently we discuss the developed extension of the nucleosome model to allow for simulation of oligonucleosomes.

3.1 DNA model

The DNA is based on the model described in [Klenin et al., 1998]; here we give a brief overview and state the basic assumptions underlying the simulation. The DNA polymer is represented as an elastic chain with electrostatic interactions. The chain has N straight segments and the chain conformation is specified by the positions of its vertices \vec{r}_i ($i = 0, \dots, N$). The segments are represented by the vectors $\vec{s}_i = \vec{r}_{i+1} - \vec{r}_i$ ($i = 0, \dots, N-1$). A local right-handed coordinate system of three orthogonal vectors $(\vec{f}_i, \vec{g}_i, \vec{e}_i)$ of unit length is attached to each segment as illustrated in Fig. (3.1). The \vec{e}_i -vector is in direction of the i th segment: $\vec{e}_i = \vec{s}_i/s_i$, where $s_i = |\vec{s}_i|$ denotes the segment length.

3.1.1 Mechanical properties of DNA

The mechanical properties of the DNA have been accounted for by harmonic potentials for bending, stretching and twisting.

The stretching energy is defined for each i th segment

$$\frac{E_i^{(s)}}{k_B T} = \frac{1}{2(l_0 \delta)^2} (l_0 - s_i)^2, \quad (3.1)$$

where l_0 is the segment equilibrium length and δ the stiffness parameter. The energy of the system is expressed in units of the thermal energy k_B throughout the work. Here k_B denotes the Boltzmann constant and the temperature of the system is held constant at T .

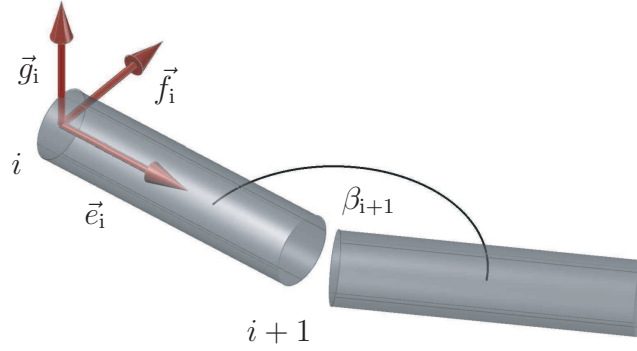


Figure 3.1: At each i th segment a local coordinate system $(\vec{f}_i, \vec{g}_i, \vec{e}_i)$ is attached. For each unbent $(i+1)$ th joint the bending angle β_{i+1} is defined as the angle between \vec{e}_i and \vec{e}_{i+1} .

A bending energy is defined for each chain joint

$$\frac{E_i^{(b)}}{k_B T} = \alpha_b \beta_i^2. \quad (3.2)$$

Here α_b is the bending rigidity parameter and β_i denotes the angle between the two adjacent segments with unit vectors \vec{e}_{i-1} and \vec{e}_i .

Considering Eq. (2.3) for the mean-square end-to-end distance of a freely rotating chain, the analogue expression for a chain with a bending potential defined by Eq. (3.2) is given by

$$\langle R^2 \rangle = N \langle s_i \rangle^2 \left(\frac{1 + \langle \cos \beta \rangle}{1 - \langle \cos \beta \rangle} \right). \quad (3.3)$$

Instead of the cosine of the constant bending angle β between adjacent segments in Eq. (2.3) the mean equilibrium cosine $\langle \cos \beta \rangle$ has been adopted. The mean equilibrium cosine can be calculated for any isotropic bending potential:

$$\langle \cos \beta \rangle = \frac{\int_0^\pi \cos \beta \sin \beta \exp(-\alpha_b \beta^2) d\beta}{\int_0^\pi \sin \beta \exp(-\alpha_b \beta^2) d\beta}. \quad (3.4)$$

As the discrete model chain shall represent an approximation of a worm-like chain with the same contour length L_c , we can identify the mean-square end-to-end distance for sufficiently large number of segments N with the mean square distance limit $\langle R^2 \rangle = BL_c$ of the worm-like chain. Then the bending rigidity parameter is related to the Kuhn length B according to the following equation

$$\frac{B}{l_0} = \frac{1 + \langle \cos \beta \rangle}{1 - \langle \cos \beta \rangle}. \quad (3.5)$$

The bending rigidity constant can be tuned, such that the model chain adopts the Kuhn length for DNA as known from experiments. Within this approach the discrete chain model represents a good approximation of worm-like chain polymers.

The sequence of the basic building blocks of DNA - the nucleotides adenine, guanine, cytosine and thymine - defines the intrinsic curvature of DNA molecules in 3-dimensional space. In detail hydrophobic effects and electrostatic interactions between adjacent base pairs are dependent on the exact sequence of CG-and AT-base pairs. They influence the relative position (tilt, roll and twist) and orientation (shift, slide and rise) of neighboring base pairs [Calladine et al., 2004]. In the simulation it is also possible to introduce sequences with intrinsic curvature. At thermal equilibrium in sequences without intrinsic curvature adjacent segment vectors \vec{e}_i and \vec{e}_{i-1} are collinear on average. In permanently bent sequences adjacent segments vectors deviate from this average collinearity of non-bended sequences at thermal equilibrium. Therefore an auxiliary unit vector \vec{b}_i with the polar coordinates (ϕ^*, θ^*) in the local coordinate system is introduced at the bent i th joint, such that the relevant bending angle for the bending energy is now calculated between \vec{e}_{i-1} and \vec{b}_i . In the new equilibrium position the segment vector \vec{e}_i points in the direction of the auxiliary unit vector.

The twist energy between two adjacent segments is defined by the following harmonic potential

$$\frac{E_i^{(t)}}{k_B T} = \frac{1}{2k_B T} \frac{C}{l_0} \tau_i^2, \quad (3.6)$$

where C is the torsional rigidity constant and τ_i is the twist angle between the $(i - 1)$ th and i th segments. Here the twist angle τ_i is defined as the sum of two angles $\tau_1 + \tau_2$. With the definition of an additional vector $\vec{p}_i = \vec{s}_{i-1} \times \vec{s}_i$, which is normal to the plane spanned by the segment vectors \vec{s}_{i-1} and \vec{s}_i , the two angles can be calculated. τ_1 is the angle between the local coordinate unit vector \vec{f}_{i-1} and the vector \vec{p}_i and τ_2 is the angle between the local coordinate unit vector \vec{f}_i and the vector \vec{p}_i .

3.1.2 Electrostatic interaction

The electrostatic interaction between DNA segments in this model is treated within the Debye-Hückel approximation, which represents the linearized equation of the full, non-linear Poisson-Boltzmann equation. The Debye-Hückel theory takes the screening

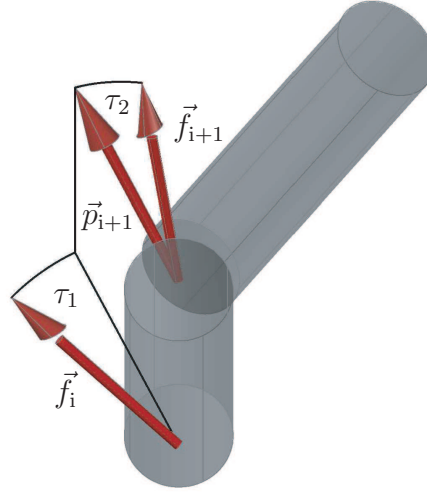


Figure 3.2: The twist angle τ_{i+1} is defined as the sum of two angles τ_1 and τ_2 . τ_1 is the angle between \vec{f}_i and \vec{p}_{i+1} , while τ_2 is the angle between \vec{p}_{i+1} and \vec{f}_{i+1} .

between charges due to the presence of mobile ions in the solution into account. If no mobile ions are present the electrostatic interaction between charges separated by a distance \vec{r} is simply given by the Coulomb interaction

$$\frac{U_{\text{Coulomb}}(\vec{r})}{k_B T} = \frac{l_B}{|\vec{r}|}, \quad (3.7)$$

where the Bjerrum length $l_B = e^2 / (4\pi D k_B T)$ is the distance at which the electrostatic interaction between two elementary charges equals the thermal energy $k_B T$. At a temperature of 298.15 K in water the Bjerrum length l_B is about 0.7 nm. The corresponding electrostatic interaction in the Debye-Hückel approximation with mobile ions in solution is

$$\frac{U_{\text{DH}}(\vec{r})}{k_B T} = l_B \frac{\exp(-\kappa|\vec{r}|)}{|\vec{r}|}. \quad (3.8)$$

Here κ denotes the inverse Debye-Hückel screening length, which is given by the expression $\kappa^2 = 8\pi e^2 I / k_B T D$. The salt solution is specified by the ionic strength I , the proton charge e and the dielectric constant of water D . Analogously the electrostatic contribution to the energy for two nonadjacent DNA segments (i, j) in a monovalent salt solution reads

$$\frac{E_{ij}^{(e)}}{k_B T} = \frac{\nu^{\star 2}}{k_B T D} \int d\lambda_i \int d\lambda_j \frac{\exp(-\kappa r_{ij})}{r_{ij}}. \quad (3.9)$$

r_{ij} is the distance between the positions along the i th segment and the j th segment, which are parameterized by the integration parameters λ_i and λ_j (see Eq. (3.14)).

DNA is a highly charged polyelectrolyte with a linear bare charge density $\nu = -2e/\Delta$, where $\Delta = 0.34$ nm is the base pair distance. As will be pointed out the bare DNA charge is reduced under certain conditions to a renormalized charge density ν^* . In the following we consider two approaches for the calculation of the renormalized charge density.

The first approach follows the charge renormalization procedure developed by Manning at the end of the 60's [Manning, 1969a,b, 1977]. Note that calculations of the electrostatic interaction on the level of the Debye-Hückel do not take into account non-linear effects, which arise due to the presence of salt ions surrounding the charged object. In such systems two mechanism are competing with each other; counterions are attracted to the charged DNA surface, but at the same time try to diffuse away from the macromolecule in order to maximize the entropy. As a result for charged objects in solution a counterion condensation transition exists at which binding of the free counterions occurs.

In this approach the distribution of counterions around highly charged polyelectrolytes is treated in terms of the Manning parameter $\xi = l_B/b$, which has the meaning of a dimensionless linear charge density and is central to the condensation transition. Here $b = \Delta/2$ denotes the distance between two elementary charges positioned along the polyelectrolyte axis. The counterions valency is denoted with z , which is in the case of monovalent ions taken to be $z = +1$. Manning states that in the case of a weakly charged polyelectrolyte, where the condition $\xi < 1/z$ holds true, the entropy terms prevail. Then the counterions are driven away from the polyelectrolyte. But for highly charged polyelectrolytes, where $\xi > 1/z$, it is energetically favorable due to the strong electrostatic interaction that a certain fraction of counterions $1 - 1/z\xi$ stays bound to the polyelectrolyte. The resulting linear charge density ν^* is therefore renormalized with respect to its bare linear charge density ν . The two components, the condensed and the free counterions are in equilibrium with each other. In the weakly charged regime $\xi < 1/z$ the renormalized charge density ν^* equals then exactly the bare linear charge density ν . In the highly charged regime $\xi > 1/z$, ν^* is renormalized to $\nu/z\xi$. We remark that the renormalized charge density is beyond the transition point just a constant function of the bare charge density. The important point is now that the renormalized charge density ν^* can be used in the linear Debye-Hückel theory replacing the bare linear charge density ν . Further the renormalization procedure allows to incorporate non-linear effects on the level of the linear Debye-Hückel approximation. For DNA the bare linear charge density with two elementary charges per phosphate group is $\nu = 5.88 \text{ nm}^{-1}$, which yields a Manning parameter $\xi = 4.2$ well beyond the transition point. The corresponding renormalized charge density is then $\nu^* = 1.4 \text{ nm}^{-1}$, which represents roughly a quarter of the bare linear charge density.

Several limitations of this ansatz have to be considered. At first the method is strictly speaking only valid in the limit of vanishing salt or correspondingly $\kappa \rightarrow 0$. At higher concentration of counterions the condensation is weakened. Also in the presence of a positively charged macromolecule like the histone core it should be expected that positive counterions decondense from the DNA. This kind of effects, termed counterion release, have been studied in many experimental [Koltover et al., 1999] and theoretical

works [Sens and Joanny, 2000], and have been also applied specific to the nucleosome system, as done in [Schiessel, 2003].

The two limiting values for the linear charge density of polyelectrolytes in the Debye-Hückel potential will be used in the simulation to estimate the overall effect of counterion condensation. Therefore the bare linear charge density ν will represent the upper limiting value, while the charge renormalization due to counterion condensation sets only a lower bound on the effective linear charge density.

For free DNA, which is not bound to a positively charged macromolecule, an often used approach is to apply the method developed in the work of Stigter et al. in Ref. [Schellman and Stigter, 1977, Stigter, 1977]. This ansatz will be used in simulations of free DNA without the presence of histone cores in this work. In this approach it is assumed that the ionic atmosphere around a DNA molecule can be classified into three regions dependent on the radial distance to the DNA axis.

- In the outmost regime the electrical potential is low ($e\psi/k_B T \ll 1$) and deviations of the DNA molecule from cylindrical symmetry are marginal. Therefore the potential satisfies the condition for the Debye-Hückel approximation.
- The condition for a weak potential ($e\psi/k_B T \ll 1$) does not hold anymore in the Gouy region, and the full, nonlinear Poisson-Boltzmann equation has to be used to calculate the potential. The ions are considered to be point charges and the cylindrical symmetry holds true.
- In the Stern layer below a radial distance r_{ES} a fraction $1 - q$ of the counterions is bound permanently e.g. to the phosphate groups of the DNA backbone. The bound counterions do not participate in laminar hydrodynamic flow when the macromolecule is in motion as in opposition to the mobile ions in the Gouy (diffusive) region.

Taking into account the cylindrical symmetry of the system, the problem can be reduced to the solution of the full, non-linear Poisson-Boltzmann equation for a cylinder with a radius r_{ES} given by the extension of the Stern layer. The charge density on the cylinder is renormalized due to the permanently bound counterions to a value $q\nu$ with a surface potential $e\zeta/k_B T$ as boundary condition. Now it is always possible to find a linear charge density ν^* such that in the outmost region the Debye-Hückel approximation matches the solution of the full Poisson-Boltzmann equation of the charged cylinder. The electrostatic radius r_{ES} and the surface potential $e\zeta/k_B T$ can now be determined from experiments of DNA electrophoretic mobility as a function of salt concentration. Experimental electrophoretic mobility data can be found in [Ross and Scruggs, 2004]. According to [Schellman and Stigter, 1977, Stigter, 1977] this allows to set the charge factor q to a value of 0.73 and an electrostatic radius of 1.2 nm for DNA in the range of physiological salt conditions as considered here in the simulations.

The electrostatic energy of the system is calculated by evaluating the Debye-Hückel integral (3.9) for each pair of non-adjacent segments, while forces and torques due to

the electrostatic interaction require partial derivatives of the expression. In order to save computational time as the calculation scales like N^2 with the number of the segments, pre-computed values of the energy integral are stored in a 4-dimensional table $f(\rho_{ij}, \gamma_{ij}, \gamma_{ji}, \sigma_{ij})$ and the respective partial derivatives at the start of the simulation. A linear interpolation is used to calculate the partial derivative at arbitrary points in the parameter space in the simulation. The range of parameter covers the conformational space of relative segment orientation to each other. The relative orientation of two segments in space can be described completely by four dimensionless parameters

$$\rho_{ij} = \frac{1}{l_0} (|\vec{r}_j - \vec{r}_i|) \quad (3.10)$$

$$\gamma_{ij} = \frac{\vec{e}_i \cdot \vec{\rho}_{ij}}{|\vec{\rho}_{ij}|} \quad (3.11)$$

$$\gamma_{ji} = -\frac{\vec{e}_j \cdot \vec{\rho}_{ij}}{|\vec{\rho}_{ij}|} \quad (3.12)$$

$$\sigma_{ij} = \frac{[\vec{s}_i \times \vec{\rho}_{ij}] [\vec{s}_j \times \vec{\rho}_{ij}]}{||[\vec{s}_i \times \vec{\rho}_{ij}]|| ||[\vec{s}_j \times \vec{\rho}_{ij}]||}. \quad (3.13)$$

The relative orientation of the segments is defined by the distance ρ_{ij} of the segmental middle points to each other, the tilt angle cosine of the i th segment γ_{ij} , the tilt angle cosine of the j th segment γ_{ji} and the twist angle cosine of the two segments σ_{ij} . The distance \vec{r}_{ij} between two points on the segments can then be parameterized with the two parameters λ_i and λ_j by the expression

$$\vec{r}_{ij} = \rho_0 \begin{pmatrix} 0 \\ 0 \\ l_0 \rho_{ij} \end{pmatrix} - \lambda_i \begin{pmatrix} \sqrt{1 - \gamma_{ij}^2} \sigma_{ij} \\ \sqrt{1 - \gamma_{ij}^2} \sqrt{1 - \sigma_{ij}^2} \\ \gamma_{ij} \end{pmatrix} + \lambda_j \begin{pmatrix} \sqrt{1 - \gamma_{ji}^2} \\ 0 \\ -\gamma_{ji} \end{pmatrix}. \quad (3.14)$$

The total contribution to the electrostatic energy is finally the sum over all pairs of nonadjacent segments (i, j) .

3.2 Histone core model

The nucleosome consists of a (H3-H4)₂ tetramer and two H2A-H2B dimers forming a fairly rigid protein complex of cylindrical shape. The crystallographic data shows further that the DNA in the nucleosome structure makes a flat, left-handed superhelix around the histone core [Luger et al., 1997]. The basic idea of the histone core model is that the known superhelical DNA conformation is recovered as ground state of the DNA-histone core system in the simulations. A description of the histone core model can be found in [Wocjan et al., 2009a].

Keeping to the idea of coarse-grained modeling and reducing the system to the essential physical properties, the histone core is represented as a cylinder with radius $R^{(n)}$. In order to simulate the adsorption of the DNA to the histone core a phenomenological

potential is assumed such that the requested DNA polymer conformation from the experiments is recovered at equilibrium. Thus a superhelical path with $N^{(n)}$ turns and a pitch $p^{(n)}$ according to the known geometry is defined on the surface of the cylinder. Then the interaction distance $|\vec{R}_i|$ between the i th DNA segment and the protein is determined as the distance between the closest point on this path and the middle point $\vec{r}_i^{(m)}$ of the segment. For physiological conditions as used in the simulations, the electrostatic interaction between the DNA chain and the octamer can be considered as short-ranged. A choice fulfilling the requirement is a simple V-groove potential with a cut-off distance r_0 for the distance dependence. The cut-off parameter is of the order of the screening length κ^{-1} , reflecting the fact that electrostatic interactions between DNA and histone core are of main importance. The interaction energy $E_i^{(n)}$ for each interacting segment can be tuned with the potential well depth parameter U_0 . The complete interaction potential is then given by

$$\frac{E_i^{(n)}}{k_B T} = \begin{cases} -U_0 \frac{r_0 - |\vec{R}_i|}{r_0} \left[\frac{\Theta_0 - \Theta_i}{\Theta_0} (1 - k_0) + k_0 \right] & \Theta_i < \Theta_0 \\ -U_0 \frac{r_0 - |\vec{R}_i|}{r_0} k_0 & \Theta_i \geq \Theta_0. \end{cases} \quad (3.15)$$

Besides the term describing the distance dependence of the potential in Eq. (3.15), also a factor for the relative orientation of segment and histone core is included. The additional factor takes into account the twist, which is induced by the superhelical geometry of DNA in the nucleosome, and balances this contribution in the twisting energy. The main idea is that at each point on the superhelical path a vector \vec{a} is defined, which gives the preferred orientation of the segment on the histone core. The relative orientation is measured by the angle $\Theta_i = \arccos(\vec{f}_i \cdot \vec{a})$ between the \vec{f}_i vector, indicating the orientation of the i th segment, and \vec{a} . The angle dependency of the potential has a V-groove shape for $\Theta_i < \Theta_0$, which energetically favors the alignment of \vec{f}_i in direction of the given orientation \vec{a} at the interaction point on the superhelical path. Outside the critical angle Θ_0 the potential is constant, but reduced by a factor k_0 . At the energy minimum of the described interaction potential DNA adopts a superhelical conformation, while being at the same time twisted according to the geometry.

The following section shows how to calculate the induced twist, and in detail the additional twist between two adjacent segments. A general procedure to calculate the twist $\text{Tw}(C_1, C_2)$ of a space curve C_1 about a second space curve C_2 is given in Ref. [White and Bauer, 1986]. The space curves can be parameterized by an angle α in the x-y plane of a right-handed coordinate system with the z-direction aligned along the histone core axis \vec{c} . Then the left-handed DNA superhelix \vec{r} and the nucleosome axis \vec{c} are described by

$$\vec{r}(\alpha) = R^{(n)} \begin{pmatrix} \cos \alpha \\ \sin \alpha \\ -\gamma \alpha \end{pmatrix} \quad \text{and} \quad \vec{c}(\alpha) = R^{(n)} \begin{pmatrix} 0 \\ 0 \\ -\gamma \alpha \end{pmatrix}, \quad (3.16)$$

where $\gamma = p^{(n)} / (2\pi R^{(n)})$ defines the slope of the space curve. For the space curves C_1 defining the nucleosome axis, while C_2 denoting the left-handed DNA superhelix, the

following equation yields the total twist

$$\text{Tw}(C_1, C_2) = \frac{1}{2\pi} \int_{C_2} [\vec{t}(\alpha) \times \vec{n}(\alpha)] \cdot d\vec{n}. \quad (3.17)$$

Thus the twist is the total change of the vector \vec{n} in the direction mutually perpendicular to the tangent vector of the superhelix \vec{t} and to \vec{n} . Here \vec{n} is the component of the vector joining a point on C_2 to the corresponding point on C_1 , which is orthogonal to the tangent vector. The corresponding parameterizations of the tangent vector \vec{t} and the vector \vec{n} are

$$\vec{t}(\alpha) = \frac{1}{\sqrt{1+\gamma^2}} \begin{pmatrix} -\sin \alpha \\ \cos \alpha \\ -\gamma \end{pmatrix} \quad \text{and} \quad \vec{n}(\alpha) = -\vec{b}(\alpha) = \begin{pmatrix} -\cos \alpha \\ -\sin \alpha \\ 0 \end{pmatrix}. \quad (3.18)$$

For this geometry one obtains for the total twist (in number of turns) along C_2

$$\text{Tw}(C_1, C_2) = \frac{1}{2\pi} \int_{C_2} [\vec{t}(\alpha) \times \vec{n}(\alpha)] \cdot \frac{d\vec{n}}{d\alpha} d\alpha \quad (3.19)$$

$$= -\frac{\gamma N^{(n)}}{\sqrt{1+\gamma^2}} \quad (3.20)$$

The twist angle $\Delta\tau$ induced by the superhelical geometry for a single segment is therefore the fraction

$$\Delta\tau = \text{Tw}(C_1, C_2) \frac{2\pi l_0 \gamma}{H^{(n)} \sqrt{1+\gamma^2}} \quad (3.21)$$

Now with the knowledge of the additional twist due to the superhelical geometry, the vector $\vec{a}(\alpha)$ can be obtained by rotation of the vector $\vec{b}(\alpha)$ about the angle $\tau = (\alpha/2\alpha_0) \Delta\tau$ around the axis $\vec{c} \times \vec{b}$. Here $2\alpha_0 = 2 \arctan(l_0/2R^{(n)})$ defines the angle, which is spanned by a single segment in the x-y plane. Fig. (3.3) shows schematically the histone octamer model.

Alternatively one can consider without loss of generality two adjacent segments with the segment center positions $\vec{r}(\alpha_0)$ and $\vec{r}(-\alpha_0)$ on the predefined superhelical path. According to the definition in section (3.1.1) the vector \vec{p} is given by the cross product of the tangent vectors $\vec{t}(-\alpha_0) \times \vec{t}(\alpha_0)$ of the two segments. Then the twist angle $\Delta\tau = \tau_1 + \tau_2$ between the two angles is the sum of the angle τ_1 between vectors $\vec{n}(-\alpha_0)$ and \vec{p} , and the angle τ_2 between \vec{p} and $\vec{n}(\alpha_0)$. The resulting twist angle per segment is given by

$$\Delta\tau = \pi - 2 \arccos \left(-\frac{\gamma \sin \alpha_0}{\sqrt{\gamma^2 + \cos^2 \alpha_0}} \right), \quad (3.22)$$

which is consistent with the calculated twist angle per segment in Eq. (3.21).

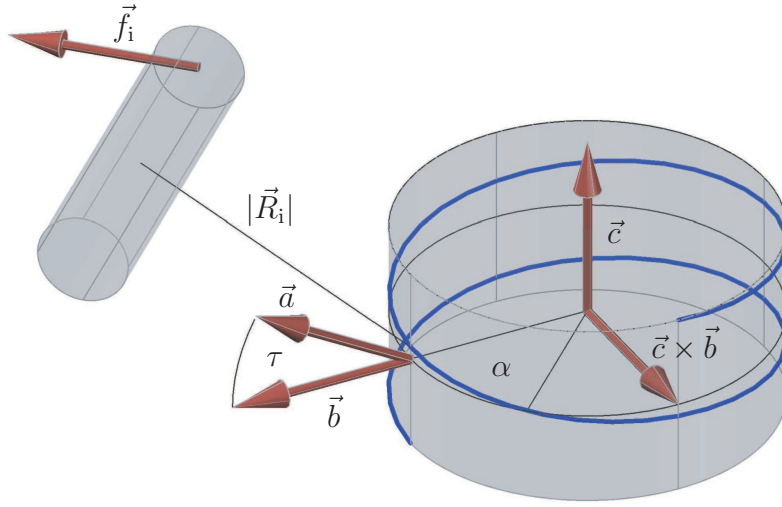


Figure 3.3: Schematic representation of the histone octamer model. The histone core is represented as a cylinder with the symmetry axis \vec{c} . A superhelix (*blue line*) of 1.75 turns is parametrized by the angle α in the plane perpendicular to the \vec{c} -axis. The distance dependence of the DNA-histone core potential is given by the interaction distance $|\vec{R}_i|$ between the middle point of the i th segment and the closest point on the superhelix. At each point of the superhelix, a vector \vec{a} is defined, which takes the DNA twist due to the spool geometry into account. The vector \vec{a} is obtained by rotation of \vec{b} by an angle τ about the rotation axis $\vec{c} \times \vec{b}$.

Throughout the work we expressed the interaction strength instead of the energy well depth U_0 by the adsorption energy density $\epsilon = U_0/l_0$. The adsorption energy density is hereby only the upper limit of the interaction strength and the effective adsorption energy density will be lower on average.

In the nucleosome model the path of the DNA is predefined, which is ultimately based on the crystallographic structure. But the assumptions underlying the model are not as rigorous as it seems. A general feature of polymer-sphere complexation is that for polymers with large persistence lengths compared to the sphere radius, the polymer distribution is rather inhomogeneous on the sphere. In addition if the adsorption energy is large, then also the fluctuations around the optimal path remain small [Marky and Manning, 1991, 1995, Schiessel et al., 2000]. Here the amount of wrapped DNA around the histone core is of the order of the persistence length, and the DNA-histone complexes can be regarded as strongly coupled due to the present high charge densities. Therefore the choice of an interaction potential, which enforces the DNA to follow a single superhelical path according to the distribution of interaction sites in the real nucleosome system, represents a reasonable approximation.

3.3 Forces and Torques

The BD algorithm requires the calculation of the forces and torques acting on the individual segments and the histone core. Forces and torques are given as the partial derivatives of the total energy over the system coordinates. The total energy of a DNA-histone core conformation is the sum of the bending, stretching, twisting, electrostatic and DNA-histone core interaction energies

$$E = \sum_{i=0}^{N-1} \left(E_i^{(b)} + E_i^{(t)} + E_i^{(s)} + E_i^{(n)} \right) + \sum_{i=0}^{N-1} \sum_{j=i+2}^{N-1} E_{ij}^{(e)}, \quad (3.23)$$

as defined in the preceding sections. The complete system is specified by the segment vertices \vec{r}_i and the angle ϕ_i of rotation of the local reference system $(\vec{f}_i, \vec{g}_i, \vec{e}_i)$ around the \vec{e}_i -axis. Further additional system coordinates introduced by the nucleosome are the position of the histone core center $\vec{r}^{(n)}$ and the orientation of the histone core, which is recorded by the histone core axis \vec{c} . The expressions for forces and torques acting on the polymer chain due to DNA-DNA interaction have been calculated in Ref. [Klenin et al., 1998]. Forces and torques acting on DNA and histone core due to the DNA-histone core interaction can be found in [Wocjan et al., 2009a] and are summarized in the appendix (7).

In Dynamic Force Spectroscopy experiments external forces can be applied to the DNA. Alternatively the device can be operated in a velocity mode, where DNA can be stretched with a constant velocity. In order to simulate these types of experiments, and the different operating modes, additional forces and constraints are included into the model.

- An additional time-dependent external force \vec{F}^{ext} can be applied to the DNA ends of a linear polymer chain. The external force starts with an initial force \vec{F}_0^{ext} and increases linearly with a constant force loading rate r_F , such that the resulting external force at time t is $\vec{F}^{\text{ext}}(t) = \vec{F}_0^{\text{ext}} + r_F t$. The direction of \vec{F}^{ext} is taken along the direction of the \hat{z} -axis of the global coordinate system. An additional force term $\Delta\vec{F}_0$ and $\Delta\vec{F}_N$ acting on the DNA end vertices \vec{r}_0 and \vec{r}_N , respectively, takes the external force into account:

$$\Delta\vec{F}_0 = -\vec{F}^{\text{ext}} \quad (3.24)$$

$$\Delta\vec{F}_N = \vec{F}^{\text{ext}}. \quad (3.25)$$

- In the velocity mode at each time step Δt the DNA end vertices are displaced relative to each other with a constant stretching velocity \vec{v} , which points in direction of the \hat{z} -axis:

$$\Delta\vec{r}_0 = -\frac{\vec{v}\Delta t}{2} \quad (3.26)$$

$$\Delta\vec{r}_N = +\frac{\vec{v}\Delta t}{2}. \quad (3.27)$$

3.4 Hydrodynamic interactions

In order to describe the dynamics of macromolecules in dilute solution, hydrodynamic interactions mediated by the solvent particles have to be taken into account. Hydrodynamic interactions were introduced to the model by attaching beads to each chain vertex and an additional bead representing the histone core. The hydrodynamic diffusion tensor \mathbf{D} represents the hydrodynamic interaction and is composed of 3×3 submatrices \mathbf{D}_{ij} , which describe the interactions between the individual beads. The submatrices can be classified according to the coupling of translational and rotational motion into translational-translational, rotational-translational, rotational-rotational and translational-rotational coupling submatrices, denoted as \mathbf{D}_{ij}^{tt} , \mathbf{D}_{ij}^{rt} , \mathbf{D}_{ij}^{rr} and \mathbf{D}_{ij}^{tr} , respectively. Further it is distinguished if the diffusional submatrix couples two different beads ($i \neq j$) or if the coupling is between the same bead ($i = j$).

Each bead has an assigned value σ_i for the bead radius. The radius σ_i can adopt the value of the hydrodynamic DNA bead radius a for a DNA bead or the hydrodynamic histone core bead radius $r_{\text{HD}}^{(n)}$ for the histone core bead. The DNA bead radius a is adjusted such that the translational diffusion coefficient of n beads placed equidistantly in a row with a distance l_0 equals the translational diffusion coefficient of a cylinder with hydrodynamic radius r_{HD} and length nl_0 . The diffusion coefficient of a cylinder can be calculated as described in [Tirado and de la Torre, 1979, 1980], while the diffusion coefficient for the string of beads is given in [Hagerman and Zimm, 1981].

In order to obtain the diffusional submatrices the approach given in [Goldstein, 1985] was applied in the simulation, retaining terms in leading order. The translational-translational self-diffusion matrix is given by

$$\mathbf{D}_{ii}^{tt} = \frac{k_B T}{6\pi\eta\sigma_i} \mathbf{I}. \quad (3.28)$$

Here η denotes the viscosity of the solution.

For the hydrodynamic interaction between different beads ($i \neq j$) two cases - overlapping and non-overlapping beads - have to be considered. This is due to the fact that the distance between different DNA beads and on the other hand a DNA and a histone core bead can become sufficiently small during simulations. The beads are called overlapping, when the spatial separation r_{ij} between the beads is less than the combined radius of the two beads $\sigma_i + \sigma_j$. The Rotne-Prager tensor [Rotne and Prager, 1969] is then modified accordingly for the non-overlapping and overlapping case

$$\mathbf{D}_{ij}^{tt} = \begin{cases} \frac{k_B T}{8\pi\eta r_{ij}} \left(1 + \frac{\sigma_i^2 + \sigma_j^2}{3r_{ij}^2}\right) \mathbf{I} + \left(1 - \frac{\sigma_i^2 + \sigma_j^2}{3r_{ij}^2}\right) \frac{\vec{r}_{ij} \otimes \vec{r}_{ij}}{r_{ij}^2} & r_{ij} \geq \sigma_i + \sigma_j \\ \frac{k_B T}{6\pi\eta\sigma_{\text{eff}}} \left[\left(1 - \frac{9r_{ij}}{32\sigma_{\text{eff}}}\right) \mathbf{I} + \frac{3}{32\sigma_{\text{eff}}} \frac{\vec{r}_{ij} \otimes \vec{r}_{ij}}{r_{ij}^2}\right] & r_{ij} < \sigma_i + \sigma_j. \end{cases} \quad (3.29)$$

If the beads have equal radii σ_{eff} is simply replaced by the respective bead radius. As there does not exist a rigorously analytical solution for overlapping beads with unequal radii, an intermediate value σ_{eff} between the different bead radii has been used throughout the simulations for this case. Then the effective radius is set to

$$\sigma_{\text{eff}} = \sqrt{(\sigma_i^2 + \sigma_j^2)/2}. \quad (3.30)$$

Similar expressions have been proposed in [Carrasco et al., 1999, Arya et al., 2006]. Rotation is treated differently for the histone core bead and DNA beads. The rotational-rotational self-diffusion matrix for the histone core bead is defined as

$$\mathbf{D}_{ii}^{rr} = \frac{k_B T}{8\pi\eta\sigma_i^3} \mathbf{I}. \quad (3.31)$$

The diffusional submatrix regarding the translation-rotation coupling between a DNA bead and a histone core bead is given by

$$\mathbf{D}_{ij}^{rt} = \begin{cases} \frac{k_B T}{8\pi\eta r_{ij}^3} \epsilon \cdot \vec{r}_{ij} & r_{ij} \geq \sigma_i + \sigma_j \\ \frac{k_B T}{8\pi\eta(\sigma_i + \sigma_j)^2} \epsilon \cdot \frac{\vec{r}_{ij}}{r_{ij}} & r_{ij} < \sigma_i + \sigma_j. \end{cases} \quad (3.32)$$

In Eq. (3.32), ϵ is the Levi-Civita tensor and the product $\epsilon \cdot \vec{r}_{ij}$ is defined, with the vector \vec{r}_{ij} in Cartesian coordinates (x_{ij}, y_{ij}, z_{ij}) , in the following way:

$$\epsilon \cdot \vec{r}_{ij} = \begin{pmatrix} 0 & z_{ij} & -y_{ij} \\ -z_{ij} & 0 & x_{ij} \\ y_{ij} & -x_{ij} & 0 \end{pmatrix}. \quad (3.33)$$

For beads representing DNA rotational movement is restricted to rotation about the \vec{e}_1 -axis. We treat therefore the rotation of individual DNA beads as hydrodynamically decoupled from the remaining beads. The corresponding rotational diffusion coefficient of a DNA bead is given by

$$D_{\text{rot}} = \frac{k_B T}{4\pi\eta r_{HD}^2 l_0}. \quad (3.34)$$

The rotational diffusion coefficient D_{rot} equals therefore the quantity for a cylinder of DNA radius r_{HD} and length l_0 .

3.5 Brownian dynamics algorithm

A classical approach for Brownian dynamics simulations is the algorithm developed by Ermak and McCammon [Ermak and McCammon, 1978]. The central equation is a first-order approximation to the solution of the stochastic differential Langevin equation. It was known that the first-order method can be inefficient or numerically unstable, therefore Iniesta and Garcia de la Torre proposed a second-order algorithm to circumvent the problems. Based on this work [Iniesta and Garcia de la Torre, 1990] a second-order Brownian dynamics algorithm [Klenin et al., 1998] is employed in the simulation to calculate the consecutive chain and histone core conformations.

The spatial conformation of the system at time t is denoted by the super vector $\vec{R}(t) = \{\vec{r}_i(t), \vec{r}^{(n)}(t), \vec{c}(t)\}$ composed of \tilde{N} components; in detail $3(N+1)$ DNA bead components and in addition 6 components for the histone core. $\vec{R}(t)$ keeps track of the bead positions \vec{r}_i , the histone core position $\vec{r}^{(n)}$ and the histone core axis \vec{c} . Additionally the angular orientation of the segments is recorded by the rotation angle

ϕ_i . The super vector $\vec{A} = \{\vec{F}_i, \vec{F}^{(n)}, \vec{T}^{(n)}\}$ is composed of the corresponding forces \vec{F}_i , $\vec{F}^{(n)}$ and torque $\vec{T}^{(n)}$ acting on the i th DNA segment and histone core. The torque acting on the i th DNA segment is recorded in T_i .

In the first half-step a vector \vec{R}' and a rotation angles ϕ'_i is predicted at time $t + \Delta t$ based on the conformation, forces and torques at time t . The predicted conformation is calculated according to the following set of equations

$$\vec{R}'_i(t + \Delta t) - \vec{R}_i(t) = \sum_{j=0}^{\tilde{N}} \mathbf{D}_{ij}(t) \frac{\vec{A}_j(t)}{k_B T} \Delta t + \vec{X}_i \quad (3.35)$$

$$\phi'_i(t + \Delta t) - \phi_i(t) = D_{\text{rot}} \frac{T_i(t)}{k_B T} \Delta t + \Phi_i. \quad (3.36)$$

The random fluctuations \vec{X}_i and Φ_i are gaussianly distributed with zero mean

$$\langle \vec{X}_i \rangle = 0 \quad (3.37)$$

$$\langle \Phi_i \rangle = 0, \quad (3.38)$$

and accordingly with the following covariances

$$\langle \vec{X}_i \vec{X}_j^T \rangle = 2\mathbf{D}_{ij} \Delta t \quad (3.39)$$

$$\langle \Phi_i \Phi_j \rangle = 2D_{\text{rot}} \Delta t. \quad (3.40)$$

The determination of the random fluctuations \vec{X}_i requires a Cholesky factorization of the hydrodynamic diffusion matrix $\mathbf{D} = \mathbf{L}\mathbf{L}^T$, where \mathbf{L} is a lower triangular matrix. In the second half-step the final system coordinates $\vec{R}_i(t + \Delta t)$ and $\phi_i(t + \Delta t)$ are obtained from the forces and torques \vec{A}_j calculated at the predicted system coordinates $\vec{R}'_i(t + \Delta t)$ and $\phi'_i(t + \Delta t)$ at time $t + \Delta t$:

$$\vec{R}_i(t + \Delta t) - \vec{R}'_i(t + \Delta t) = \sum_{j=0}^{\tilde{N}} \mathbf{D}_{ij}(t) \frac{-\vec{A}_j(t) + \vec{A}'_j(t + \Delta t)}{2k_B T} \Delta t \quad (3.41)$$

$$\phi_i(t + \Delta t) - \phi'_i(t + \Delta t) = D_{\text{rot}} \frac{-T_i(t) + T'_i(t + \Delta t)}{2k_B T} \Delta t. \quad (3.42)$$

The hydrodynamic diffusion tensor \mathbf{D} is not updated in every simulation step but only every 500 simulation steps to speed up the simulation. The speed up is significant due to the time-consuming Cholesky factorization of the hydrodynamic interaction matrix during updating and at the same time the dynamic properties remain according to [Klenin et al., 1998] still within statistical errors.

3.6 Parametrization

We discuss the introduced DNA/histone core model parameters and also general simulation parameters. If possible we relate the model parameters to experimental data.

3.6.1 DNA parameters

The choice of the stiffness parameter δ is a tradeoff between computational time and deviations from the equilibrium segment length (see [Jian et al., 1997]). Large values of the stiffness parameter δ allow for large deviations $\sigma = \sqrt{\langle s_i^2 \rangle - \langle l_0 \rangle^2}$ of the segment length s_i . In contrast small stiffness parameter values result in a significant change of the stretching forces during the simulation time step Δt , which sets an upper bound for the time step Δt . In the nucleosome simulations a stiffness parameter $\delta = 0.16$ is used, such that the expected value for $\sigma = 0.156 l_0$ represents a good compromise. The Young's modulus Y of the elastic rod is defined by the formula $F_i/A = Y(s_i - l_0)/l_0$, where F_i is the stretching force and A is the effective cross-sectional area of the rod. Often instead of the Young's modulus the stretch modulus YA (Y times A) of DNA is used, which is related to the stiffness parameter via $YA = k_B T / l_0 \delta^2$. For the used stiffness parameter we obtain a stretch modulus of ≈ 63.3 pN, which corresponds to a softer elastic chain than actual DNA.

The bending stiffness of DNA is determined by the energy associated with the deformation of hydrogen bonds and the electrostatic repulsion of negatively charged monomers of the DNA. While the first term is charge-independent, resulting in a bare mechanical persistence length, the second term is dependent on the actual salt concentration of the solution. The bare mechanical persistence length is recovered in the limit of high salt, yielding a value of ≈ 30 nm in experiments [Manning, 1981, Borochoy et al., 1981, Sobel and Harpst, 1991]. In the range of physiological salt conditions DNA has a total persistence length l_p of about 50 nm [Hagerman, 1988]. As only nonadjacent segments contribute to the electrostatic interaction energy, we therefore work with the total persistence length corresponding to a Kuhn length of $B = 2l_p = 100$ nm.

The torsional elasticity of the DNA polymer is described in the model with the torsional elastic constant C . Torsion constants have been quantitatively assessed by time-resolved fluorescence polarization anisotropy (FPA), the topoisomer distributions of ligated small circular DNA and cyclization of small DNAs as a function of length. The determined values for the torsional elastic constant range from 2.0×10^{-19} erg cm [Taylor and Hagerman, 1990], 2.2×10^{-19} erg cm [Heath et al., 1996] to $\approx 3.0 \times 10^{-19}$ erg cm [Horowitz and Wang, 1984, Shore and Baldwin, 1983]. According to [Heath et al., 1996] the latter high torsional elastic constants are obtained from experiments with small DNA rings, which may not be transferable to linear and larger circular DNA. For the simulations we adopt an intermediate value of $C = 2.5 \times 10^{-19}$ erg cm in the range of $2.0 - 3.0 \times 10^{-19}$ erg cm, as used in previous BD studies [Merlitz et al., 1998, Vologodskii et al., 1992].

For the hydrodynamic radius r_{HD} of DNA we set the value to 1.2 nm according to Ref. [Hagerman and Zimm, 1981].

The complete list of DNA model parameters can be found in Tab. (3.1).

Parameter	Description	Value
N	number of segments	30
l_0	equilibrium segment length	2.5 nm
δ	stiffness parameter	0.16
B	Kuhn length	100 nm
C	torsional rigidity constant	61.8 k _B T
r_{HD}	hydrodynamic DNA radius	1.2 nm

Table 3.1: DNA model parameter values (nucleosome simulation)

3.6.2 Histone octamer parameters

The decisive parameters regarding the nucleosome geometry in the model are the radius of the DNA superhelix $R^{(n)}$, the pitch $p^{(n)}$ defining the distance between neighboring DNA turns and the number of windings $N^{(n)}$. We take crystallographic data from Ref. ([Luger et al., 1997]) as a reference nucleosome system, which showed that the ideal superhelix fit to the double helix axis over 125 bp yields a superhelix radius $R^{(n)} = 4.18$ nm and a pitch $p^{(n)} = 2.39$ nm with 1.65 windings. As an additional 20 bp of DNA are organized in the nucleosome, we set the effective number of turns to the canonical value $N^{(n)} = 1.75$.

Based on the dimension of the histone core octamer [Arents et al., 1991] we employ a value of 3 nm for the hydrodynamic histone core radius $r_{HD}^{(n)}$.

The DNA/histone core potential is parameterized by an interaction strength ϵ . The adsorption energy density ϵ represents a free parameter, and is determined in this work by comparison between simulations and experiments. Due to the electrostatic screening at the physiological conditions a cut-off of 0.5 nm is set, which is of the order of the screening length κ^{-1} . Further to accommodate for the induced twist in the superhelical geometry, the potential energetically favors the alignment of the segment orientation with the preferred orientation \vec{a} on the superhelical path within the interval $[-\Theta_0, \Theta_0]$. We set the critical angle Θ_0 to $\pi/2$, while outside the interval the interaction energy is greatly reduced by the factor $k_0 = 0.1$.

The histone core model parameters are listed in Tab. (3.2).

3.6.3 Simulation parameters

In this work all simulations were performed at a constant temperature T of 293.15 K. The time step is fixed at $\Delta t = 6 \times 10^{-12}$ s. The surrounding solution has a viscosity of $\eta = 10^{-3}$ Pa s, an ionic strength $I = 150$ mM of monovalent ions and a dielectric constant $D = 80.18$ (at the indicated system temperature T).

Parameter	Description	Value
$R^{(n)}$	DNA superhelix radius	4.18 nm
$N^{(n)}$	number of turns	1.75
$p^{(n)}$	pitch	2.39 nm
$r_{\text{HD}}^{(n)}$	hydrodynamic histone core radius	3.0 nm
Θ_0	critical potential angle	$\pi/2$
k_0	potential coefficient	0.1
r_0	potential cut-off distance	0.5 nm

Table 3.2: Histone core parameter values (nucleosome simulation)

Parameter	Description	Value
Δt	simulation time step	6.0 ps
T	temperature	293.15 K
I	ionic strength	150 mM
η	viscosity	10^{-3} Pa s
D	dielectric constant	80.18

Table 3.3: Simulation parameter values (nucleosome simulation)

3.7 Initialization

In order to ensure that the system is in thermodynamical equilibrium, we relaxed the initial conformation to generate the starting conformation. Hereby the following protocol was applied:

- An initial conformation is created, where all segments are ordered in a straight line and the histone core $\vec{r}^{(n)}$ is positioned at a distance $R^{(n)}$ from the middle chain segment $\vec{r}_{N/2}^{(m)}$ (Fig. 3.7 (a)).
- In a second step a constant external force of 20 pN to the DNA end segments is applied until a maximum of 3 segments are interacting with the histone core for 10^5 simulation steps (Fig. 3.7 (b)). The i th segment is termed interacting if the interaction distance $|\vec{R}_i|$, is within the cutoff distance r_0 .
- In a last step this extended conformation is relaxed in 10^8 simulation steps with no external forces to an equilibrated conformation, where DNA follows a superhelical path around the histone core (Fig. 3.7 (c)).

The system reaches thermodynamic equilibrium, when the characteristic observables cease to show a systematic drift and have started to oscillate about steady mean values [Allen and Tildesley, 1989]. In (Fig. 3.5) the total energy of the nucleosome system and the contour length, the amount of DNA interacting with the histone protein, which will be introduced in section (5.2.1), have been recorded during the final relaxation step. The observables reach a plateau at a timescale of $\approx 2 \mu\text{s}$ or correspondingly $\approx 3 \times 10^6$ simulation steps, which represents an upper bound for the relaxation times. Therefore the number of simulated configurations in the trajectory to generate the starting conformations exceeds significantly the number of simulation steps to reach the plateau.

For the calculated observables we considered only measurements of trajectories beginning at the starting conformations, while skipping the initial data during the relaxation protocol.

The stretching simulations have been calculated on a AMD Opteron 2.4 Ghz system, such that e.g. a 3.6 ms Brownian dynamics simulation with 6×10^8 steps took ≈ 1 week of computer time.

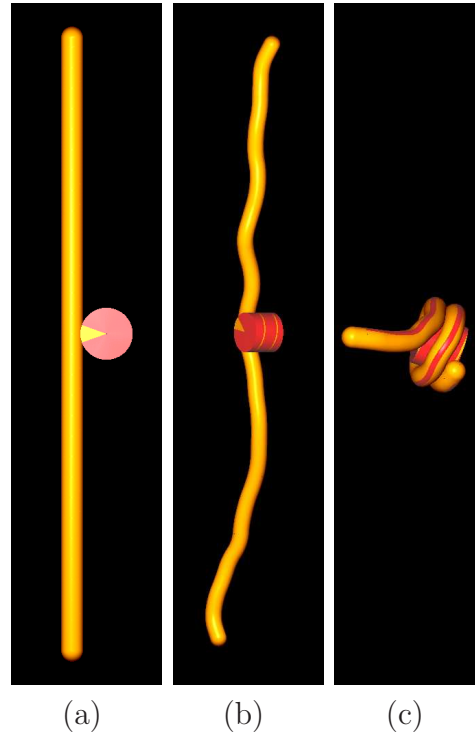


Figure 3.4: The figure series shows representative conformations during initialization: (a) initial conformation, (b) extended conformation with an external applied force of 20 pN and (c) relaxed starting conformation.

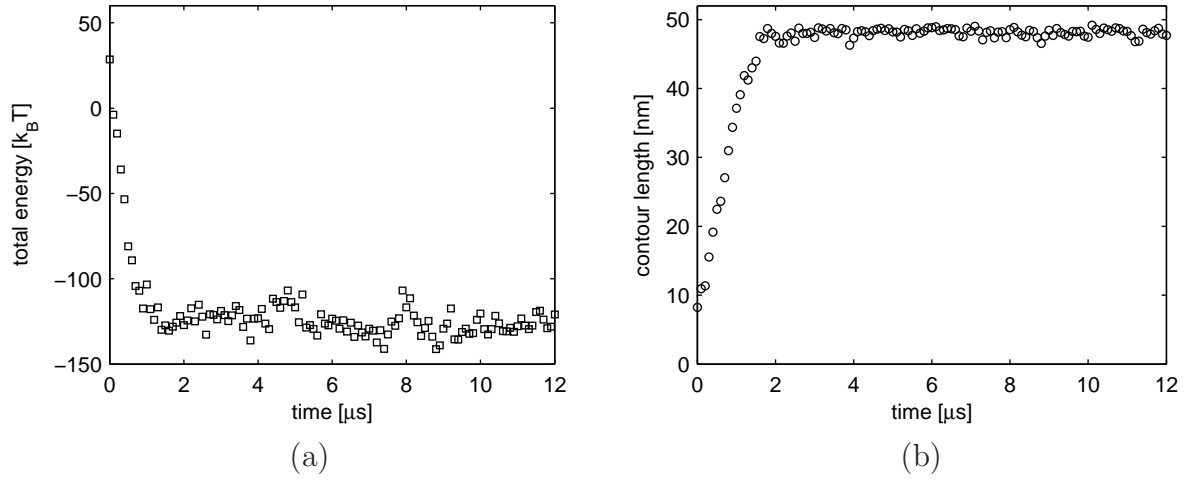


Figure 3.5: (a) The total energy of the nucleosome system has been monitored to estimate the relaxation times at which equilibrium is reached ($\epsilon = 8 k_B T \text{ nm}^{-1}$). Starting from an extended conformation (see Fig. (3.4b)) the total energy crosses over to a steady mean value at times $> 2 \mu s$ or correspondingly $\approx 3 \times 10^6$ simulation steps. (b) The amount of adsorbed DNA to the histone core as function of time indicates a similar relaxation to the nucleosome ground state.

3.8 Circular and superhelical DNA

So far, the simulation model was described within the framework of the nucleosome system, which consists of a linear DNA chain and the histone core. In this section the modifications according to [Klenin et al., 1998] for the simulation of circular and superhelical DNA are summarized.

The circular chain geometry has an additional constraint, that the vertices \vec{r}_0 and \vec{r}_N are identical. In superhelical dsDNA an important topological invariant is the number of times the two ssDNA wind around each other - the linking number Lk . If the contours C_1 and C_2 of both strands are known, the linking number can be given by the Gauss integral

$$Lk = \frac{1}{4\pi} \oint_{C_1} \oint_{C_2} \frac{[d\vec{r}(s_1) \times d\vec{r}(s_2)] \cdot (\vec{r}_1 - \vec{r}_2)}{|\vec{r}_1 - \vec{r}_2|^3}, \quad (3.43)$$

where s_1 and s_2 are the positions along the contours of C_1 and C_2 , respectively [Grosberg and Khokhlov, 1994]. The linking number Lk can be expressed as the sum of two geometrical quantities [White, 1969]

$$Lk = Tw + Wr. \quad (3.44)$$

The twist Tw describes the twisting of one strand around the other in a planar conformation, while the writhe Wr is a measure of the extent to which the DNA axis coils and folds in three dimensions. The linking number difference $\Delta Lk = Lk - Lk_0$

quantifies the amount of excess superhelicity introduced into the circular structure with respect to the relaxed B-DNA molecule. The torsionally relaxed B-DNA molecule has one right-handed twist per 3.4 nm. A related quantity to the linking number difference is the superhelical density

$$\sigma = \frac{\Delta Lk}{Lk_0}. \quad (3.45)$$

The linking number difference ΔLk is introduced in the simulation of circular DNA as an additional input parameter. The invariance of the linking number difference according to Eq. (3.44) is checked during the simulation.

3.8.1 Monte Carlo algorithm

A starting conformation for the BD simulation is generated by a Monte Carlo procedure [Klenin et al., 2000]. The Monte Carlo algorithm is derived from [Vologodskii et al., 1992] with modifications implemented in [Klenin et al., 2000]. The definition of the segments and beads is identical to the Brownian dynamics simulation. The energy terms have been also adopted, except that no deviations of the equilibrium segment length l_0 are allowed. The Monte Carlo algorithm uses two different Monte Carlo steps to allow for adequate sampling of conformation space:

(1) In a pivoting step, a subchain of 2-10 segments is randomly chosen, and rotated about its end-to-end vector by the angle β uniformly distributed in an interval $(-\beta_0, \beta_0)$. The fraction of this pivoting step is 2/3, and the overall acceptance rate is $\approx 50\%$.

(2) In a reptation step a randomly chosen subchain of 5 segments is exchanged with a randomly chosen subchain of 4 segments, if the end-to-end distance of the 5-segment subchain is not longer than 4 segments. Each subchain was deformed by changing the end-to-end distance such that it could be incorporated at the position of the other subchain. The deformation of a subchain was realized as a sequence of rotations of the individual segment vectors \vec{s}_i until the condition for the end-to-end distance was fulfilled. Here each subchain segment was rotated around the vector $\vec{s}_i \times \vec{X}$ by a small angle proportional to $|\vec{s}_i \times \vec{X}|$, where \vec{X} is the subchain end-to-end vector. The orientation of the inserted subchain was chosen such that the orientation of the center-of-mass with respect to the end-to-end axis coincides with the orientation of the center-of-mass of the exchanged subchain. The fraction of the reptation step is 1/3.

The acceptance of the MC pivoting step is the same as in the standard Metropolis algorithm. Regarding the reptational step the modifications of Ref. [Klenin et al., 2000], which take into account the entropy change by adjusting the end-to-end distance of the subchains, have been kept the same. From the initial conformation 10^8 Monte Carlo steps have been calculated to obtain the starting conformation for the Brownian dynamics simulation.

3.8.2 pUC18 plasmid

In order to study the dynamics of circular and superhelical DNA, we used the pUC18 plasmid as a model system. The pUC18 plasmid contains 2686 base pairs, therefore the

circular DNA was approximated by a closed chain of $N = 91$ linear segments of length $l_0 = 10$ nm. The bending persistence length $l_p = 50$ nm and the torsional rigidity at $C = 2.5 \times 10^{-19}$ erg cm were the same as for the nucleosome simulations. The same stretching modulus of 63.3 pN was used, therefore the stiffness parameter was reduced to $\delta = 0.08$ taking into account the longer DNA segments. The DNA linear charge density was renormalized according to the described procedure by Stigter [Stigter, 1977]. We studied the circular DNA at different superhelical densities $\sigma = \Delta Lk/Lk_0$ e.g. from relaxed DNA at $\sigma = 0$ to $\sigma \approx -0.037$. For linear DNA the same parameters as for circular DNA has been used. All simulations have been calculated at 0.1 M salt conditions and a temperature $T = 293.15$ K. The time step is set to $\Delta t = 1$ ns. Table (3.4) summarizes all used simulation parameters and Table (3.5) lists the parameters for the pUC18 plasmid.

Parameter	Description	Value
Δt	simulation time step	1.0 ns
T	temperature	293.15 K
I	ionic strength	100 mM
η	viscosity	1.0×10^{-3} Pa s
D	dielectric constant	80.18

Table 3.4: Simulation parameter values (circular DNA simulations)

Parameter	Description	Value
N	number of segments	91
l_0	equilibrium segment length	10.0 nm
δ	stiffness parameter	0.08
B	Kuhn length	100 nm
C	torsional rigidity constant	61.8 k _B T
r_{HD}	hydrodynamic DNA radius	1.2 nm
r_{ES}	electrostatic DNA radius	1.2 nm
q	charge factor	0.73

Table 3.5: DNA parameter values (circular DNA simulations)

3.9 Oligonucleosomes

In this work the coarse-grained model was extended to allow the simulation of multiple and interacting nucleosomes. In the following the modifications regarding the nucleosome-nucleosome and hydrodynamic interactions are described.

3.9.1 Nucleosome-Nucleosome interaction

In the preceding sections it was discussed that the shape of nucleosomes can be approximated by a cylindric geometry. An interaction potential between nucleosomes must therefore take into account explicitly the toroidal geometry of the nucleosome. We follow here an approach, which includes the geometry, and was adapted by [Wedemann and Langowski, 2002] to the context of nucleosomes. The basic idea is that the interaction between non-spherical molecules can be approximated by the overlap of two identical ellipsoidal Gaussians with arbitrary orientations \hat{u}_i and \hat{u}_j [Berne and Pechukas, 1972]. Hence the orientation-dependent expressions for strength and range of ellipsoid-shaped particles can be used in a classical Lennard-Jones potential [Lennard-Jones, 1931], which exhibits a more realistic distance dependence. In the simulation we use a Gay-Berne potential to model the interactions between nucleosomes [Gay and Berne, 1981], which is based on the original overlap model and includes modifications as described in [Kabadi, 1986a,b]. The expression for the nucleosome-nucleosome interaction potential between nucleosomes at positions \vec{r}_i and \vec{r}_j is finally given by:

$$U(\hat{u}_i, \hat{u}_j, \vec{r}) = 4\epsilon(\hat{u}_i, \hat{u}_j, \hat{r}) \left[\left(\frac{\sigma_0}{r - \sigma(\hat{u}_i, \hat{u}_j, \hat{r}) + \sigma_0} \right)^{12} - \left(\frac{\sigma_0}{r - \sigma(\hat{u}_i, \hat{u}_j, \hat{r}) + \sigma_0} \right)^6 \right]. \quad (3.46)$$

The unit vectors \hat{u}_i and \hat{u}_j describe the orientation of the symmetry axis of the interacting particles. In the case of nucleosomes the unit vectors point in direction of the cylinder axis \vec{c} of the respective nucleosome. The molecular separation $r = |\vec{r}|$ is defined by the intermolecular vector between the nucleosomes $\vec{r} = \vec{r}_i^{(n)} - \vec{r}_j^{(n)}$, while $\hat{r} = \vec{r}/r$ is the associated unit vector. Further $\epsilon(\hat{u}_i, \hat{u}_j, \hat{r})$ denotes the potential well depth and $\sigma(\hat{u}_i, \hat{u}_j, \vec{r})$ is the intermolecular separation at which the attractive and repulsive terms cancel.

In the modified overlap potential [Gay and Berne, 1981], Gay and Berne rectified two problems encountered in the original overlap model. First they corrected for the distance dependence of the potential well depth ϵ_0 by including besides the original term

$$\epsilon(\hat{u}_i, \hat{u}_j) = (1 - \chi^2(\hat{u}_i \hat{u}_j))^{-\frac{1}{2}}, \quad (3.47)$$

also a second interaction strength term, which is a function of \hat{u}_i and \hat{u}_j as well as \hat{r}

$$\epsilon'(\hat{u}_i, \hat{u}_j, \hat{r}) = 1 - \frac{\chi'}{2} \left(\frac{(\hat{r} \hat{u}_i + \hat{r} \hat{u}_j)^2}{1 + \chi'(\hat{u}_i \hat{u}_j)} + \frac{(\hat{r} \hat{u}_i - \hat{r} \hat{u}_j)^2}{1 - \chi'(\hat{u}_i \hat{u}_j)} \right), \quad (3.48)$$

such that the total potential well depth is given by the product

$$\epsilon(\hat{u}_i, \hat{u}_j, \hat{r}) = \epsilon_0 \epsilon^\nu(\hat{u}_i, \hat{u}_j) \epsilon'^\mu(\hat{u}_i, \hat{u}_j, \hat{r}). \quad (3.49)$$

The ratio of an energy well depth ϵ_s for a lateral configuration and ϵ_e for a longitudinal configuration of the interacting particles can be tuned by the well depth anisotropy parameter χ'

$$\chi' = \frac{1 - \left(\frac{\epsilon_e}{\epsilon_s}\right)^{1/\mu}}{1 + \left(\frac{\epsilon_e}{\epsilon_s}\right)^{1/\mu}}. \quad (3.50)$$

A second improvement upon the original overlap potential was to eliminate the dependence of the potential well width on the orientation by shifting the potential rather than scaling it. The distance in Eq. (3.46) at which attractive and repulsive terms cancel is given by

$$\sigma(\hat{u}_i, \hat{u}_j, \vec{r}) = \sigma_0 \left[1 - \frac{\chi}{2} \left(\frac{(\hat{r}\hat{u}_i + \hat{r}\hat{u}_j)^2}{1 + \chi(\hat{u}_i\hat{u}_j)} + \frac{(\hat{r}\hat{u}_i - \hat{r}\hat{u}_j)^2}{1 - \chi(\hat{u}_i\hat{u}_j)} \right) \right]^{-\frac{1}{2}} \quad (3.51)$$

with the constant σ_0 . The shape anisotropy of the potential is defined by the parameter

$$\chi = \frac{\sigma_{\parallel}^2 - \sigma_{\perp}^2}{\sigma_{\parallel}^2 + \sigma_{\perp}^2}. \quad (3.52)$$

Here σ_{\parallel} and σ_{\perp} signify the major and minor axes of the ellipsoids.

It has been shown that mononucleosomes can form a hexagonal-columnar phase [Leforestier and Livolant, 1997, Leforestier et al., 2001]. The measured mean distances in the liquid phase are 7.16 ± 0.65 nm between nucleosomes in a single column and 11.55 ± 1 nm between nucleosomes in two columns. The potential parameters can then be tuned in such a way that the potential minimas match the experimentally found inter-nucleosomal distances. The energy well depth ϵ_0 can be adjusted with comparison of phase transition temperature in computer simulations [Emerson et al., 1994]. The choice of parameters is taken according to Ref. [Wedemann and Langowski, 2002]. The complete set of parameters is listed in Tab. (3.6).

Fig. (3.6a) shows the nucleosome-nucleosome interaction potential as function of the internucleosomal distance and nucleosome configuration (lateral/longitudinal).

3.9.2 Excluded volume interaction

In systems with more than two nucleosomes the probability of histone core and DNA collisions increase. Therefore we account explicitly for the excluded volume of the histone core by including an additional potential between histone core and DNA beads, which prohibits e.g. the collisions of DNA segments with the histone core and introduces topological constraints for DNA/histone core motion. This is important as so

Parameter	Description	Value
ϵ_0	potential well depth	$0.25 \text{ k}_B \text{ T}$
σ_0	ellipsoid diameter	10.3 nm
χ	shape anisotropy parameter	-0.506
χ'	well depth anisotropy	-0.383
ν	well depth exponent (1st)	1
μ	well depth exponent (2nd)	2

Table 3.6: Nucleosome-nucleosome interaction parameter values

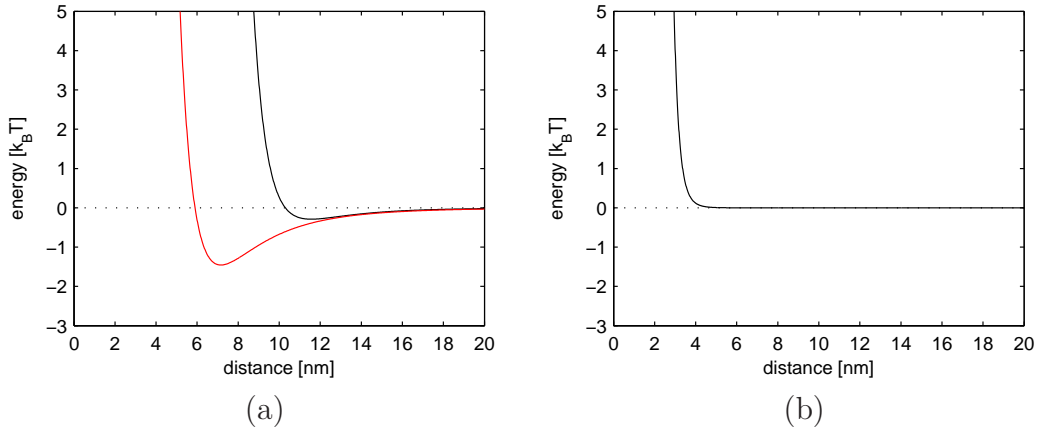


Figure 3.6: (a) The distance-dependence of the nucleosome-nucleosome interaction potential is shown for a lateral (*black*) and a longitudinal configuration (*red*) (b) Distance-dependence of excluded volume interaction (*black*).

far the DNA-histone core interaction was restricted to the predefined superhelical path along the cylinder surface. For the sake of simplicity we use hereby a Lennard-Jones potential given by

$$U_{\text{LJ}}(r) = k_{\text{ev}} \left(\left(\frac{\sigma_{\text{ev}}}{r} \right)^{12} - \left(\frac{\sigma_{\text{ev}}}{r} \right)^6 \right) \quad (3.53)$$

with the effective diameter σ_{ev} , while k_{ev} is an energy parameter controlling the steepness of the excluded volume potential. The excluded volume v_{ev} is defined with the help of the Mayer f-function [Rubinstein and Colby, 2003]

$$f(r) = \exp \left(-\frac{U_{\text{LJ}}(r)}{k_B T} \right) - 1 \quad (3.54)$$

by the following expression

$$v_{\text{ev}} = - \int f(r) d^3r = \int \left(1 - \exp \left(-\frac{U_{\text{LJ}}(r)}{k_B T} \right) \right) d^3r. \quad (3.55)$$

σ_{ev} and k_{ev} are adjusted in such a way that the excluded volume for the interaction potential $U_{\text{LJ}}(r)$ equals the excluded volume of a hard-core repulsion potential of a cylinder with a height 6 nm and diameter 6.5 nm [Arents et al., 1991], while at the same time the DNA-histone core potential is not significantly disturbed. The used parameters of the excluded volume interaction are tabulated in Tab. (3.7).

Parameter	Description	Value
σ_{ev}	effective diameter	6 nm
k_{ev}	potential prefactor	0.001 k _B T

Table 3.7: Excluded volume parameter values

The distance-dependence of the excluded volume interaction with parameters according to Tab. (3.7) is shown in Fig. (3.6b).

3.9.3 Internucleosomal forces and torques

In this section the forces and torques due to the internucleosomal potential and the excluded volume interaction are summarized.

The force acting on the i th nucleosome \vec{F}_i exerted from a j th nucleosome is calculated as the partial derivative with respect to the nucleosome position \vec{r}_i

$$\vec{F}_i = -\frac{\partial U}{\partial \vec{r}_i}. \quad (3.56)$$

The right-hand side of Eq. (3.56) may be evaluated to

$$\begin{aligned} \frac{\partial U}{\partial \vec{r}_i} = & 8\epsilon_0\epsilon(\hat{u}_i, \hat{u}_j) \left(\epsilon' \frac{\partial \epsilon'}{\partial \vec{r}_i} \left[\left(\frac{\sigma_0}{r - \sigma + \sigma_0} \right)^{12} - \left(\frac{\sigma_0}{r - \sigma + \sigma_0} \right)^6 \right] - \right. \\ & \left. \frac{3\epsilon'^2}{r - \sigma + \sigma_0} \left(\hat{r} - \frac{\partial \sigma}{\partial \vec{r}_i} \right) \left[2 \left(\frac{\sigma_0}{r - \sigma + \sigma_0} \right)^{12} - \left(\frac{\sigma_0}{r - \sigma + \sigma_0} \right)^6 \right] \right) \end{aligned} \quad (3.57)$$

with the terms

$$\begin{aligned} \frac{\partial \epsilon'}{\partial \vec{r}_i} = & -\frac{\chi'}{r} \left[\frac{\hat{r}\hat{u}_i + \hat{r}\hat{u}_j}{1 + \chi'(\hat{u}_i\hat{u}_j)} (\hat{u}_i + \hat{u}_j) + \frac{\hat{r}\hat{u}_i - \hat{r}\hat{u}_j}{1 - \chi'(\hat{u}_i\hat{u}_j)} (\hat{u}_i - \hat{u}_j) \right. \\ & \left. - \frac{(\hat{r}\hat{u}_i + \hat{r}\hat{u}_j)^2}{1 + \chi'(\hat{u}_i\hat{u}_j)} \hat{r} - \frac{(\hat{r}\hat{u}_i - \hat{r}\hat{u}_j)^2}{1 - \chi'(\hat{u}_i\hat{u}_j)} \hat{r} \right] \end{aligned} \quad (3.58)$$

and

$$\frac{\partial \sigma}{\partial \vec{r}_i} = \frac{\sigma_0 \chi}{2r} \left(1 - \frac{\chi}{2} \left(\frac{(\hat{r}\hat{u}_i + \hat{r}\hat{u}_j)^2}{1 + \chi(\hat{u}_i\hat{u}_j)} + \frac{(\hat{r}\hat{u}_i - \hat{r}\hat{u}_j)^2}{1 - \chi(\hat{u}_i\hat{u}_j)} \right) \right)^{-\frac{3}{2}} \quad (3.59)$$

$$\left[\frac{\hat{r}\hat{u}_i + \hat{r}\hat{u}_j}{1 + \chi(\hat{u}_i\hat{u}_j)} (\hat{u}_i + \hat{u}_j) + \frac{\hat{r}\hat{u}_i - \hat{r}\hat{u}_j}{1 - \chi(\hat{u}_i\hat{u}_j)} (\hat{u}_i - \hat{u}_j) - \frac{(\hat{r}\hat{u}_i + \hat{r}\hat{u}_j)^2}{1 + \chi(\hat{u}_i\hat{u}_j)} \hat{r} - \frac{(\hat{r}\hat{u}_i - \hat{r}\hat{u}_j)^2}{1 - \chi(\hat{u}_i\hat{u}_j)} \hat{r} \right]. \quad (3.60)$$

The torque acting on the i th nucleosome \vec{T}_i exerted by the j th nucleosome is calculated with the following expression

$$\vec{T}_i = -\hat{u}_i \times \left(\frac{\partial U}{\partial \hat{u}_i} \right). \quad (3.61)$$

The implemented equation for the torque is given by

$$\begin{aligned} \frac{\partial U}{\partial \hat{u}_i} = & 4\epsilon_0 \left(\left(\frac{\partial \epsilon}{\partial \hat{u}_i} \epsilon'^2 + 2\epsilon \epsilon' \frac{\epsilon'}{\partial \hat{u}_i} \right) \left[\left(\frac{\sigma_0}{r - \sigma + \sigma_0} \right)^{12} - \left(\frac{\sigma_0}{r - \sigma + \sigma_0} \right)^6 \right] \right. \\ & \left. + \frac{6\epsilon \epsilon'^2}{r - \sigma + \sigma_0} \frac{\partial \sigma}{\partial \hat{u}_i} \left[2 \left(\frac{\sigma_0}{r - \sigma + \sigma_0} \right)^{12} - \left(\frac{\sigma_0}{r - \sigma + \sigma_0} \right)^6 \right] \right), \end{aligned} \quad (3.62)$$

with the partial derivatives

$$\frac{\partial \epsilon}{\partial \hat{u}_i} = \chi^2 (\hat{u}_i\hat{u}_j) (1 - \chi^2 (\hat{u}_i\hat{u}_j))^{-\frac{3}{2}} \hat{u}_j, \quad (3.63)$$

$$\begin{aligned} \frac{\partial \epsilon'}{\partial \hat{u}_i} = & -\frac{\chi'}{2} \left[\frac{2(\hat{r}\hat{u}_i + \hat{r}\hat{u}_j)}{1 + \chi'(\hat{u}_i\hat{u}_j)} \hat{r} + \frac{2(\hat{r}\hat{u}_i - \hat{r}\hat{u}_j)}{1 - \chi'(\hat{u}_i\hat{u}_j)} \hat{r} \right. \\ & \left. - \frac{(\hat{r}\hat{u}_i + \hat{r}\hat{u}_j)^2}{(1 + \chi'(\hat{u}_i\hat{u}_j))^2} \chi' \hat{u}_j + \frac{(\hat{r}\hat{u}_i - \hat{r}\hat{u}_j)^2}{(1 - \chi'(\hat{u}_i\hat{u}_j))^2} \chi' \hat{u}_j \right] \end{aligned} \quad (3.64)$$

and

$$\frac{\partial \sigma}{\partial \hat{u}_i} = \frac{\sigma_0 \chi}{4} \left(1 - \frac{\chi}{2} \left(\frac{(\hat{r}\hat{u}_i + \hat{r}\hat{u}_j)^2}{1 + \chi(\hat{u}_i\hat{u}_j)} + \frac{(\hat{r}\hat{u}_i - \hat{r}\hat{u}_j)^2}{1 - \chi(\hat{u}_i\hat{u}_j)} \right) \right)^{-\frac{3}{2}} \quad (3.65)$$

$$\left[\frac{2(\hat{r}\hat{u}_i + \hat{r}\hat{u}_j)}{1 + \chi(\hat{u}_i\hat{u}_j)} \hat{r} + \frac{2(\hat{r}\hat{u}_i - \hat{r}\hat{u}_j)}{1 - \chi(\hat{u}_i\hat{u}_j)} \hat{r} - \frac{(\hat{r}\hat{u}_i + \hat{r}\hat{u}_j)^2}{(1 + \chi(\hat{u}_i\hat{u}_j))^2} \chi \hat{u}_j + \frac{(\hat{r}\hat{u}_i - \hat{r}\hat{u}_j)^2}{(1 - \chi(\hat{u}_i\hat{u}_j))^2} \chi \hat{u}_j \right]. \quad (3.66)$$

The contribution of the excluded volume interaction results in an additional force on the i th DNA bead exerted by the j th histone core:

$$\vec{F}_i^{(ev)} = -\frac{\partial U_{LJ}}{\partial \vec{r}_i} = -\frac{\partial U_{LJ}}{\partial r} \hat{r} \quad (3.67)$$

3.9.4 Hydrodynamic interactions in oligonucleosome model

Regarding the hydrodynamic interaction between different histone cores, we have to specify in addition to the valid definitions in section (3.4) also a rotational-rotational coupling between the histone cores. With the result from Goldstein [Goldstein, 1985] we define the rotational-rotational cross diffusional matrix for non-overlapping spheres

$$\mathbf{D}_{ij}^{rr} = \frac{1}{16\pi\eta r_{ij}^3} \left(-\mathbf{I} + 3 \frac{\vec{r}_{ij} \otimes \vec{r}_{ij}}{r_{ij}^2} \right). \quad (3.68)$$

Due to the repulsive part of the histone core-histone core interaction we can disregard the cases with overlapping spheres.

Chapter 4

Dynamics of circular DNA

This chapter is focused on the dynamics of single monomers in circular DNA. In plasmids, the circular DNA has mostly a superhelical conformation. Equilibrium properties of superhelical DNA were investigated and understood in great detail in experiments [Adrian et al., 1990, Strick et al., 1996], simulations [Vologodskii et al., 1992, Hammermann et al., 1998] and analytical theories [Marko and Siggia, 1995, Marko, 1997]. Dynamic light scattering measurements provided information on the motion of whole DNA rings and the dominant mode of their internal fluctuations [Kremer et al., 1993, Langowski et al., 1994]. Recently Fluorescence Correlation Spectroscopy (FCS) allowed also to monitor the dynamics on the level of individual monomers within polymers. Here we are interested in the effect of superhelicity and bent sequences in DNA rings on single monomer motion. In the first part time trajectories of circular DNA were simulated using the Brownian dynamics (BD) algorithm. The BD simulations are compared to analytical models of semiflexible polymers. The subsequent parts of the chapter are devoted to the effect of inserting permanent bends into the DNA sequence. Further the rotational motion of a fluorophore attached to a DNA monomer is analyzed, which is shown to modify the outcome of FCS measurements on the simulated DNA monomer trajectories.

4.1 Circular DNA

DNA conformations

The conformation of a DNA molecule in space is related to its internal twist [White, 1969]. If additional twist is introduced in the torsionally relaxed DNA state, which can not relax e.g. by the rotation of a free DNA end, then the DNA forms a supercoil. Two kinds of supercoiled conformations exist [Calladine et al., 2004]: (a) The circular DNA consists of a series of open spirals that wind around an imaginary toroid, which is known as solenoid, or (b) the DNA crosses over and under itself repeatedly with terminal loops, the so-called plectoneme. In bacterial plasmids typically the interwound structure was found. The solenoidal winding was observed where DNA is already highly curved, since the solenoid supercoil geometry requires high curvature of DNA. The curvature can be on account of either the base pair sequence or due

to wrapping around proteins e.g. in nucleosomes. Longer DNA strands promote the branching from a linear interwound structure to single and multiple Y-bifurcation of the plectoneme, but it is also known that branching is a function of superhelical density and the effective DNA radius, which corresponds to ionic conditions in the solution [Vologodskii et al., 1992].

With the Monte Carlo and Brownian dynamics algorithm circular DNA conformations have been generated. Representative DNA conformations taken from the ensemble are shown in Fig. (4.1). In the relaxed state with no additional torsional strain ($\Delta Lk = 0$), circular DNA adopts a random coil conformation. Increasing the superhelical density σ the DNA undergoes a structural transition from the random coil to a supercoiled plectoneme [Boles et al., 1990]. The transition involves the reduction of superhelical radius and the increase of the average number of DNA cross-overs as can be inferred from typical conformations in the $\Delta Lk = -4$ and $\Delta Lk = -10$ structure (see Fig. (4.1)b,c). For higher superhelical densities the structure becomes more regular. Here we refer to [Klenin et al., 1991, Vologodskii et al., 1992], where extensive and quantitative MC simulation studies of the equilibrium conformations of supercoiled DNA have been done. In the following sections we focus on the DNA dynamics.

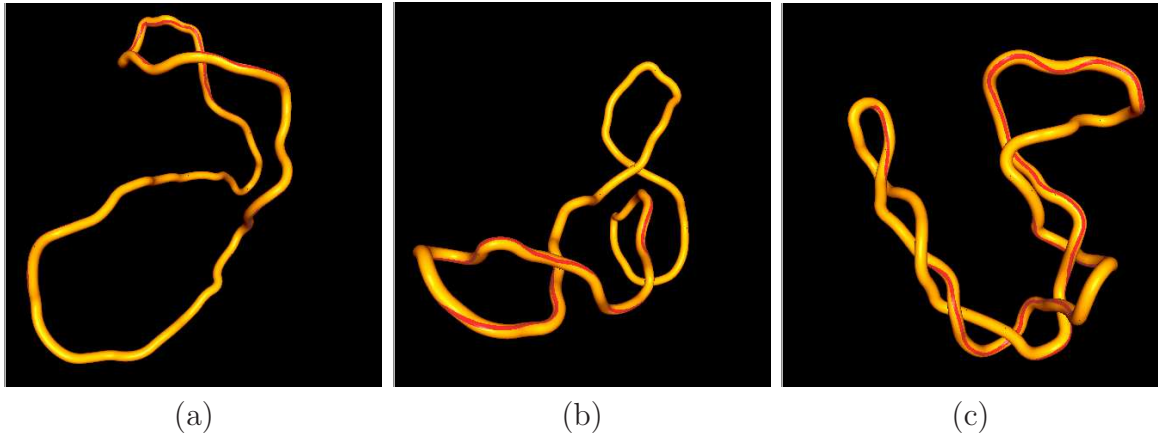


Figure 4.1: Representative conformations of 2.7 kbp circular DNA with increasing superhelical density $|\sigma|$. (a) $\sigma = 0$ ($\Delta Lk = 0$) (b) $\sigma \approx -0.015$ ($\Delta Lk = -4$) (c) $\sigma \approx -0.037$ ($\Delta Lk = -10$)

4.1.1 Brownian dynamics time trajectories

The BD simulation allowed us to calculate time trajectories of DNA rings. The polymer conformations described by the bead positions $\{\vec{r}_i\}$ and the segmental orientation $\{\vec{f}_i\}$ have been recorded at a set of M discrete time points $\{t\}$. For long time trajectories, positions and conformations have been saved every 1000th time step Δt . In order to resolve dynamics on shorter time scales, additional short time trajectories have been used, where conformations were recorded at every time step. For each set of parameters five long and five short time trajectories have been calculated with a length of 500 ms

and $100 \mu\text{s}$, respectively. The short time trajectories allowed us to obtain properties e.g. mean-square displacement of a labeled bead, in the time interval $[1 \text{ ns}, 1 \mu\text{s}]$, while the longer time trajectories were used in the time range from $1 \mu\text{s}$ to 50 ms . All calculated properties have been averaged over the simulated trajectories.

Translational diffusion coefficient

As a first step the translational diffusion coefficient D_t can be estimated from the slope of the center-of-mass trajectory. The center-of-mass \vec{r}_{cm} is defined as the average of the bead positions

$$\vec{r}_{\text{cm}}(t) = \frac{1}{N} \sum_{i=1}^N \vec{r}_i(t) \quad (4.1)$$

and the mean-square displacement (MSD) of the center-of-mass over a time interval τ is given by the following expression

$$\langle \vec{r}_{\text{cm}}^2(\tau) \rangle = \frac{1}{M} \sum_{\{t\}} [\vec{r}_{\text{cm}}(t + \tau) - \vec{r}_{\text{cm}}(t)]^2. \quad (4.2)$$

The MSD of the center-of-mass displays strictly normal diffusion on all time scales. A fit according to the normal diffusion equation $\langle \vec{r}_{\text{cm}}^2(\tau) \rangle = 6D_t\tau$ yields the translational diffusion coefficients $D_t = 3.9 \mu\text{m}^2\text{s}^{-1}$ at $\Delta Lk = 0$ and $D_t = 5.0 \mu\text{m}^2\text{s}^{-1}$ at $\Delta Lk = -10$. The higher translational diffusion coefficient at increasing linking number differences can be explained by the formation of a compact plectonemic structure (see Tab. (4.2)). In Ref. [Langowski et al., 1994] the pUC18 plasmid (2687 bp) was studied by dynamic light scattering (DLS) and in addition by computer simulations. The DLS experiments reported a translational diffusion coefficient in the range $D_t \approx 3.8 - 4.1 \mu\text{m}^2\text{s}^{-1}$ for $\Delta Lk = 0$ and $D_t \approx 4.7 - 4.8 \mu\text{m}^2\text{s}^{-1}$ for $\Delta Lk = -10$. Chain conformations were generated by Monte Carlo simulations based upon the program *corchy*, which incorporated electrostatic interactions only on the level of a hard-core potential. The diffusion coefficients of the chain configurations were computed using the modified Kirkwood approximation found by [De Haen et al., 1983], and supported the experimental findings, although the calculated value for the translational diffusion coefficient was shifted to slightly higher values $D_t \approx 4.8 - 5.3 \mu\text{m}^2\text{s}^{-1}$ for superhelical DNA. We conclude that the BD simulations in this work reproduce the data found in the MC simulations [Langowski et al., 1994] and are in good agreement with the DLS data.

Internal dynamics of single DNA monomers

Knowledge of the motion of individual monomers provides valuable insight into the internal structure, interactions and environment of polymers. In the simulations the position \vec{r}_i of a single, arbitrary bead was tracked. The internal motion of a bead $\langle \vec{r}_{\text{rel}}^2(\tau) \rangle$ as defined relative to the center-of-mass is as follows

$$\langle \vec{r}_{\text{rel}}^2(\tau) \rangle = \frac{1}{M} \sum_{\{t\}} [(\vec{r}_i(t + \tau) - \vec{r}_{\text{cm}}(t + \tau)) - (\vec{r}_i(t) - \vec{r}_{\text{cm}}(t))]^2. \quad (4.3)$$

The simulated data for the internal motion of the labeled bead are depicted in Fig. (4.2a). At small time scales the internal motion follows a power law $\langle \vec{r}_{\text{rel}}^2(\tau) \rangle \propto \tau^\alpha$. For different linking number differences ΔLk we found the exponents $\alpha \approx 0.74$ ($\Delta Lk = 0$) and $\alpha \approx 0.72$ ($\Delta Lk = -10$), where we fitted in the time range $10^{-7} \text{ s} < \tau < 10^{-5} \text{ s} \ll \tilde{\tau}_1$. Here $\tilde{\tau}_1$ denotes the longest relaxation time of the polymer. In order to quantify the effect of DNA circularization we studied also a linear DNA, which had the same contour length of 910 nm as for circular DNA. The monitored bead was positioned in the center of the DNA chain, such that forces on the bead are exerted symmetrically from both sides. This is comparable to the situation of a bead in circular DNA and allows to disregard DNA end effects. The fit yields an exponent $\alpha \approx 0.74$ for linear DNA.

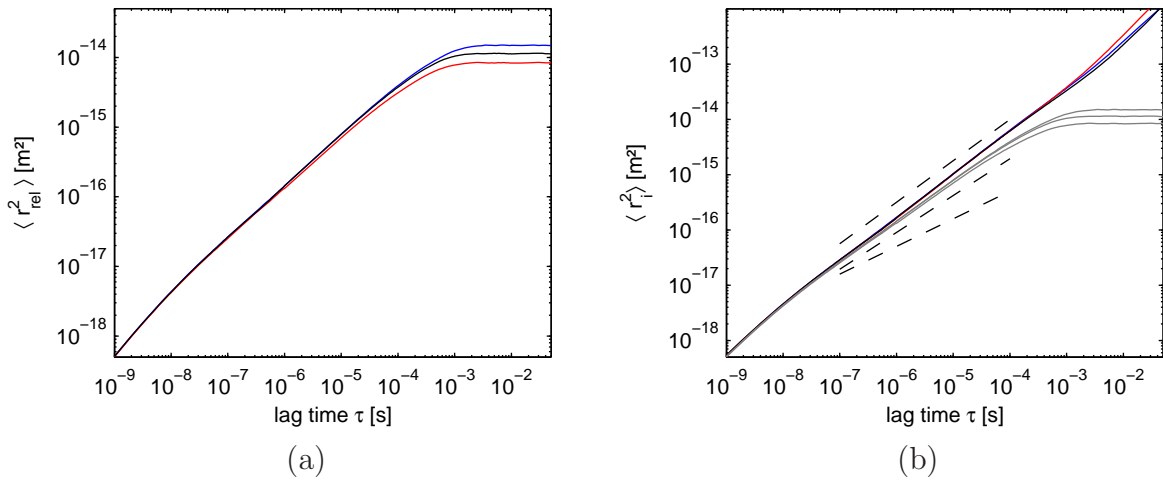


Figure 4.2: (a) The figure shows the MSD $\langle \vec{r}_{\text{rel}}^2 \rangle$ of the DNA monomer relative to the center-of-mass for circular DNA with different linking number differences $\Delta Lk = 0$ (solid blue), $\Delta Lk = -10$ (solid red) and a linear DNA (solid black). (b) The total MSD $\langle \vec{r}_{\text{i}}^2 \rangle$ is shown. The color coding is kept as in (a). The dashed line mark $\tau^{3/4}$ -, $\tau^{2/3}$ - and $\tau^{1/2}$ -power laws (from top to bottom) to guide the eye. In addition the contributions of the internal motions $\langle \vec{r}_{\text{rel}}^2 \rangle$ taken from (a) are renewed (grey).

All exponents are close to $3/4$, which is expected from polymer physics for the dynamics of linear semiflexible polymers [Kroy and Frey, 1997, Harnau et al., 1996]. The $3/4$ -power law is obtained as an approximation in the limit of a stiff chain at length scales below the persistence length, where the bending modes dominate and the stretching modes can be neglected. At times longer than the longest relaxation time $\tilde{\tau}_1$ the internal motion saturates at a constant value. The longest relaxation time in the case of the linear polymer is $\tilde{\tau}_1 \approx 1 \text{ ms}$ as calculated from the autocorrelation of the end-to-end vector. At very short times $\tau < 10^{-8} \text{ s}$ the exponent falls into the range between 0.8 and 0.9.

In Fig. (4.2a) the curve for the linear DNA matches the corresponding curve for circular DNA in the relaxed state for a broad range of times up to approximately $\tilde{\tau}_1$. Therefore the formation of a DNA ring represents only a small perturbation with respect to the linear DNA for the internal motion of a single bead.

Mean-square displacement of single DNA monomers

A quantity, which is directly accessible to experimental measurements, is the MSD of a labeled bead $\langle \vec{r}_i^2 \rangle$. The MSD is the superposition of the internal dynamics and the center-of-mass motion and is calculated in the simulation according to the following equation

$$\langle \vec{r}_i^2(\tau) \rangle = \frac{1}{M} \sum_{\{t\}} [\vec{r}_i(t + \tau) - \vec{r}_i(t)]^2. \quad (4.4)$$

At small times the motion of the monitored bead is determined predominantly by the internal motion, while the contribution of the center-of-mass diffusion remains small. The MSD obeys therefore approximately the 3/4-power law as shown in Fig. (4.2b). In turn for times $t \gg \tilde{\tau}_1$ beyond the longest relaxation times the contribution from the internal motion become negligible and the dynamics is dominated by the center-of-mass diffusion.

In order to study further the power law behavior of the MSD, a local time-dependent exponent $\beta(\tau)$ was defined. The MSD curves were fitted locally to $\langle r_i^2(\tau) \rangle \propto \tau^\beta$ in the interval $[0.1\tau, 10\tau]$ in vicinity of the lag time τ . The results are shown in Fig. (4.3).

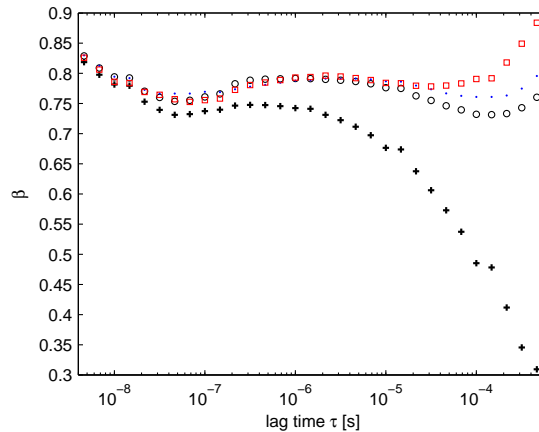


Figure 4.3: The time-dependent local exponent $\beta(\tau)$ of the MSD power-law $\langle r_i^2 \rangle \propto \tau^{\beta(\tau)}$ has been obtained by fitting in the time interval $[0.1\tau, 10\tau]$. The local exponent is depicted for the linear (*circle*) and the circular DNA for a linking number difference $\Delta Lk=0$ (*dot*) and $\Delta Lk = -10$ (*square*). In addition *crosses* mark the contribution of internal motion for linear DNA.

At long lag times the local exponent should approach unity, characterizing normal diffusion. Due to the required longer simulation times in calculating the local exponent, this limit is not fully reached, but the center-of-mass diffusion is superimposed by contributions of internal motion. In the framework of the Rouse and Zimm model as presented in section (2.1.2) the MSD scales in the limit $\tau \ll \tilde{\tau}_1$ with a power law $\tau^{1/2}$ and $\tau^{2/3}$, respectively [Doi and Edwards, 1986]. Recent single-molecule experimental studies on dsDNA dynamics in dilute solution lead to a controversy whether

the monomer motion is controlled by hydrodynamic interactions [Lumma et al., 2003, Winkler et al., 2006] as predicted by the Zimm model or not [Shusterman et al., 2004] as follows from the Rouse model. For linear end-labeled dsDNA fragments of different length L results consistent with the Zimm model have been experimentally observed only for very long polymers exceeding 10^4 bp [Petrov et al., 2006], which corresponds to the limit of flexible polymers $L \gg l_p$. In this study the experimental data was interpreted in the framework of the theory of Gaussian semiflexible polymers [Harnau et al., 1996], which comprises the Zimm regime for long polymers (see section (2.1.2)). In [Shusterman et al., 2004] the Zimm regime was also observed for the longest measured linear dsDNA molecule of 23.1 kbp, which corresponds to the common view on polymer dynamics. But in contradiction an additional Rouse regime on intermediate time scales was reported for dsDNA in the range from 2.4 to 23.1 kbp of studied molecule lengths. In a subsequent study [Shusterman et al., 2008] circular DNA constructs, in detail pUC18 plasmids, were measured with a similar FCS experimental setup. For the pUC18 plasmid, which is used here as a model system in the simulations, an exponent $\beta \approx 0.5$ typical of Rouse dynamics was found at intermediate times $\tau \approx 100 \mu s$. A recent study [Hinczewski et al., 2009] predicted also the existence of a sub-Zimm regime for end-monomer MSD in long DNA molecules, but could also not account fully for the observed Rouse regime.

Here, the BD simulations based on a homogeneously elastic chain do not display an intermediate regime as reported in [Shusterman et al., 2008], which could have been attributed to Rouse- or Zimm-like dynamics; the local exponent $\beta(\tau)$ remains on all time scales above 0.7. But we see a shallow minimum in the local exponent as proposed recently in [Hinczewski et al., 2009], reflecting the decrease in the internal dynamics of the semiflexible polymer for the linear and circular DNA before the crossover from the stiff-rod limit to the flexible chain limit and normal diffusion. The minimum is observed for lag times $\approx 100 \mu s$. Circularization of DNA diminished the effect, and additional torsional stress at higher superhelical densities further reduces the depth of the local minimum. In circularized DNA due to the compaction the transition to normal diffusion sets in at smaller time scales, therefore superimposing the local minimum.

Amplitude of internal motion

The internal motion of individual monomers in the DNA coil is restricted and reaches its maximal MSD eventually for sufficient times as shown in Fig. (4.1.1). The relative amplitude of internal fluctuations a can be calculated in the saturated constant regime at times $\tau > \tilde{\tau}_1$. In the limit $\tau \rightarrow \infty$ the internal motion of a bead $\langle \vec{r}_{\text{rel}}^2(\tau) \rangle$ is related to the amplitude and can be simply described by the MSD of two independent variables x_1 and x_2 distributed uniformly in the interval $[-a, +a]$, which is bounded by the amplitude of internal motion:

$$\lim_{\tau \rightarrow \infty} \langle \vec{r}_i^2(\tau) \rangle = \frac{3}{4a^2} \int_{-a}^{+a} dx_1 \int_{-a}^{+a} dx_2 (x_1 - x_2)^2 = 2a^2. \quad (4.5)$$

Taking into account the independent degree of freedom in x-,y- and z-directions yields an additional factor 3 in the equation. The amplitudes $a = 86.1 \text{ nm}$ ($\Delta Lk = 0$) and

$a = 65.5 \text{ nm}$ ($\Delta Lk = -10$) were obtained by fitting $2\langle a^2 \rangle$ in the saturated regime. The decrease can be rationalized due to the more interwound, tighter structure for higher superhelical densities, which restricts the motion of the individual segments. Earlier it has been showed that the amplitude of internal motions decreases approximately by a factor 2 as a function of increasing superhelical density [Langowski et al., 1994] from $\sigma = 0$ to $\sigma = -0.05$. The decrease is nonmonotonic and passes a local maximum at $\sigma \approx -0.03$.

The same DLS experiment [Langowski et al., 1994] showed that the internal diffusion coefficient, which has been qualitatively interpreted as a measure of the motions of the smallest rigid DNA subunit in the superhelix, remained unchanged for most of the superhelical densities. Only well beyond a superhelical density $\sigma = -0.04$ a significant increase of the internal diffusion coefficient with respect to the relaxed state has been observed. In the simulations the MSD of the internal motion (see Fig. 4.2a) displays no acceleration of the dynamics up to the investigated superhelical density $\sigma \approx -0.037$. The ratio of the MSD for the $\Delta Lk = -10$ superhelix and the relaxed DNA ring as calculated in Tab. (4.1a) deviates on all intermediate time scales at the most 4 % from unity.

$\tau [\text{s}]$	10^{-7}	10^{-6}	10^{-5}	10^{-4}	10^{-3}
(a)	0.98	0.97	0.97	0.97	1.04
(b)	0.98	0.96	0.96	0.94	1.00
(c)	1.07	1.11	1.13	1.12	1.09

Table 4.1: Mean-square displacement ratio of circular DNA at linking number differences $\Delta Lk = -10$ to $\Delta Lk = 0$. The cases for circular DNA (a) without a permanently bend sequence, with a permanently bent sequence, where the monitored bead has been positioned (b) in 25 % of the contour length L relative to the bent sequence and (c) directly at the bent sequence.

Acceleration of sites in end loops

Circular DNA undergoes a structural transition from a random coil at low superhelical densities σ to a supercoiled plectoneme [Boles et al., 1990] at high superhelical densities. The supercoiled plectoneme can be roughly subdivided into a stem region where two DNA strands are closely interwound and end loop regions, where the DNA makes a turn, forming a loop. A representative structure of a plectoneme can be found in Fig. (4.1c). In the following section we have studied the effect on the dynamics, if the monitored DNA section can be assigned either to a position in the stem region or an end loop of the plectoneme.

End loops have been identified by using a method developed in [Klenin et al., 1995].

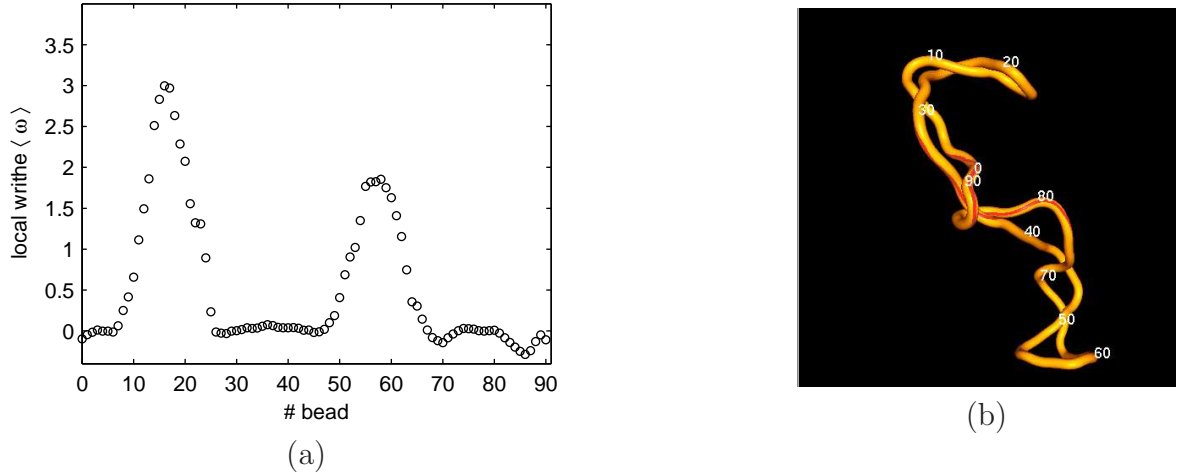


Figure 4.4: According to [Klenin et al., 1995] the local writhe ω can be used to identify end loops in DNA conformations, as the end loop position is characterized by a maximum in the number of tail cross-overs. Fig. (a) shows the local writhe ω dependent on the bead position for the DNA conformation in Fig. (b). The numbers indicate the spatial position of the corresponding beads as counted in Fig. (a).

The method defines in analogy to the definition of the writhe Wr along the total contour [Doi and Edwards, 1986] a local writhe $\omega(j)$ in the vicinity of a segment j . The Gaussian integral describes then the average number of cross-overs between the two tails of k segments at the segment j :

$$\omega(j) = \frac{1}{2} \int_{\vec{r}_{j-k}}^{\vec{r}_j} \int_{\vec{r}_{j+1}}^{\vec{r}_{j+k+1}} (d\vec{r}_1 \times d\vec{r}_2) \frac{\vec{r}_1 - \vec{r}_2}{|\vec{r}_1 - \vec{r}_2|^3}. \quad (4.6)$$

Here we set the number of segments belonging to a tail $k = 18$, which corresponds to approximately 3-4 persistence lengths. The Gaussian integral can be evaluated as shown in [Klenin and Langowski, 2000] to compute the writhe in circular DNA. In Fig. (4.4a) the local writhe ω has been calculated with help of Eq. (4.6) as a function of the bead position in the circular DNA. In addition the actual DNA conformation is depicted in Fig. (4.4b). The maxima of local writhe correspond to the two end loops as seen in the DNA conformation. From visual inspection of ≈ 100 independent conformations it can be stated that in general segments which are characterized by high local writhe ω belong to the end loops in superhelical conformations.

In order to relate the motion of an individual bead to its positioning within a stem region or an end loop, bead trajectories were analyzed. The 500 ms-trajectories of the labeled bead were divided into time intervals of 10 ms. For each time interval the average local writhe $\langle \omega \rangle$ was calculated. Simultaneously also the MSD $\langle \vec{r}_i^2(\tau) \rangle$ for different lag times τ was obtained. Fig. (4.5a) shows the relation between the MSD and the average local writhe. Both quantities display correlations for intermediate times as

expressed by high correlation coefficient

$$\rho = \frac{\text{cov}(\text{MSD}, \langle \omega \rangle)}{\sigma_{\text{MSD}} \sigma_{\langle \omega \rangle}}, \quad (4.7)$$

where $\text{cov}(\text{MSD}, \langle \omega \rangle)$ denotes the covariance of MSD and local writhe and σ the corresponding standard deviations. The regression coefficient $\rho \approx 0.89, 0.87, 0.69$ and 0.23 decreases continuously for the set of lag times $\tau = 10^{-6} \text{ s}, 10^{-5} \text{ s}, 10^{-4} \text{ s}$ and 10^{-3} s . From the figure we infer that at higher average local writhe, which is related to an end loop positioning of the labeled bead, the MSD is increased. For example for a lag time of $100 \mu\text{s}$ the MSD of a DNA monomer in an end loop with a local writhe $\langle \omega \rangle = 1.5$ is increased by 30% relative to a non-loop region characterized by the local writhe $\langle \omega \rangle = 0$. This can be rationalized by comparison with linear polymers. The BD simulations demonstrated clearly that if the labeled bead is positioned at the end of a linear DNA molecule the internal motion increased relative to the bead positioned at the DNA center (see Fig. (4.5b)). This can be verified also in the framework of the Gaussian semiflexible chain model, described in section (2.1.2). If the contour coordinate is shifted from the center position $s = 0$ to the polymer ends $s = \pm L/2$, then the calculated contributions from the normal modes and corresponding eigenfunctions ψ_k are such that the resulting internal motion is accelerated. In circular DNA we observe a similar effect for DNA monomers in end loops.

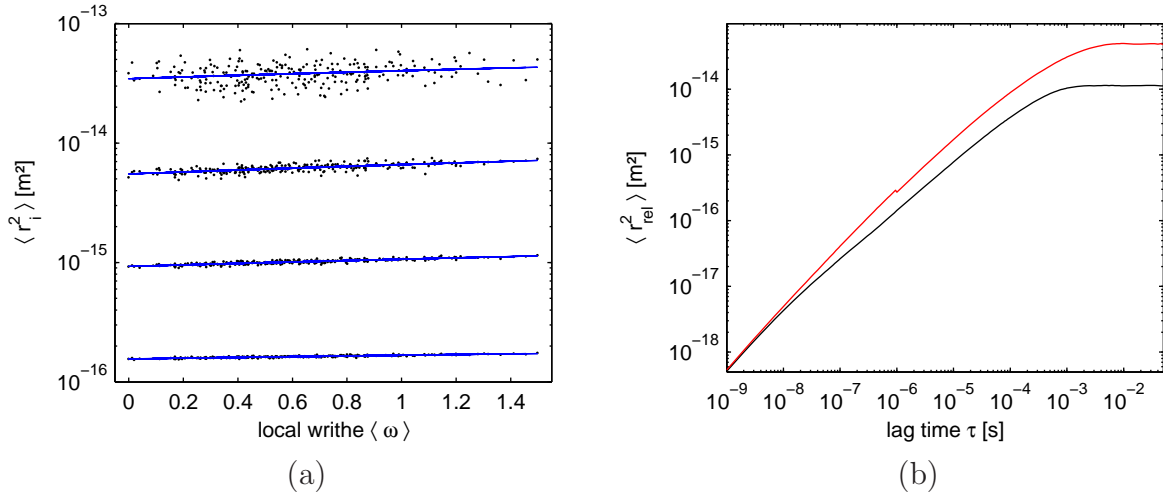


Figure 4.5: (a) Mean-square displacement $\langle r_i^2(\tau) \rangle$ as a function of the mean local writhe ω has been calculated for 10 ms-time intervals from trajectories of labeled beads. The MSD has been evaluated at different lag times $\tau = 10^{-6} \text{ s}, 10^{-5} \text{ s}, 10^{-4} \text{ s}$ and 10^{-3} s (from bottom to top). (b) The internal motion $\langle \vec{r}_{\text{rel}}^2 \rangle$ is compared for linear DNA with the labeled bead in the DNA center (black) and DNA end (red).

4.2 Comparison to analytical solution

4.2.1 Gaussian semiflexible chain model

Macromolecules exhibit a broad range of flexibility from very flexible molecules (e.g. ssDNA), semiflexible molecules (e.g. dsDNA) to rigid objects (e.g. microtubule). Equilibrium properties of semiflexible polymers are often investigated by the Kratky-Porod model [Kratky and Porod, 1949] or the Gaussian chain model [Doi and Edwards, 1986] (see section 2.1.1). A description of flexible macromolecules dynamics is provided by the framework of the Rouse-Zimm model [Rouse, 1953, Bueche, 1954, Zimm, 1956]. An approach for the dynamics of a Gaussian semiflexible chain has been presented in [Harnau et al., 1995, 1996] by Harnau, Winkler and Reineker (HWR model), which has the advantage that it is valid for the complete range of polymer stiffness.

In order to validate the simulation, dynamic properties like the internal motion and the time correlation of the segment vector have been calculated analytically within this approach. Details of the calculation of the equation governing the internal motion $\langle \vec{r}_{\text{rel}}(\tau)^2 \rangle$ of a Gaussian semiflexible chain can be found in [Harnau et al., 1996], and the main points are briefly summarized in section (2.1.2).

The following parameters have been used to allow the direct comparison with the simulation results. We considered a linear chain of contour length $L = 910$ nm. Further a thickness of the molecule $d = 2.4$ nm is assumed to exclude self-interactions. The temperature T and viscosity η has been set to identical values as used in the simulations. In the evaluation of the sum in Eq. (2.19) a final cutoff for the mode number $\Lambda = 150$ has been set. The properties have been calculated at the center of the DNA molecule for a contour coordinate $s = 0$.

In the analytical HWR model the segment vector $\vec{e}_i(t)$ can be approximated by the normalized difference vector of two points at the continuous contour coordinates s and s' on the polymer:

$$\vec{e}_i(t) = \frac{\vec{r}(s, t) - \vec{r}(s', t)}{|\vec{r}(s, t) - \vec{r}(s', t)|}. \quad (4.8)$$

Analogously to the derivation of Eq. (2.19) the expansion of $\vec{r}(s, t)$ in terms of the eigenfunctions allowed us to obtain the temporal correlation function of the segment vectors $\langle \vec{e}_i(t) \vec{e}_i(0) \rangle$:

$$\langle \vec{e}_i(t) \vec{e}_i(0) \rangle = \frac{k_B T}{\pi \eta} \sum_{l=1}^{\infty} \tau_l \exp\left(-\frac{t}{\tau_l}\right) [\psi_l^2(s) - 2\psi_l(s)\psi_l(s') + \psi_l^2(s')] \quad (4.9)$$

The equation has been evaluated by setting the separation of the two points on the contour to l_0 (or equivalently $s' = s + l_0$), which corresponds to the equilibrium segment length in the discrete simulation model.

The deviations of the internal motion calculated for the HWR model relative to simulation results do not exceed 22 % and approximate very well the saturated regime at large times. A close agreement has been found also for the reorientation of the segment vector with time between HWR model and BD simulation (see Fig. (4.6b)). Considering the simplicity of the analytical model e.g. preaveraging of the hydrodynamic tensor

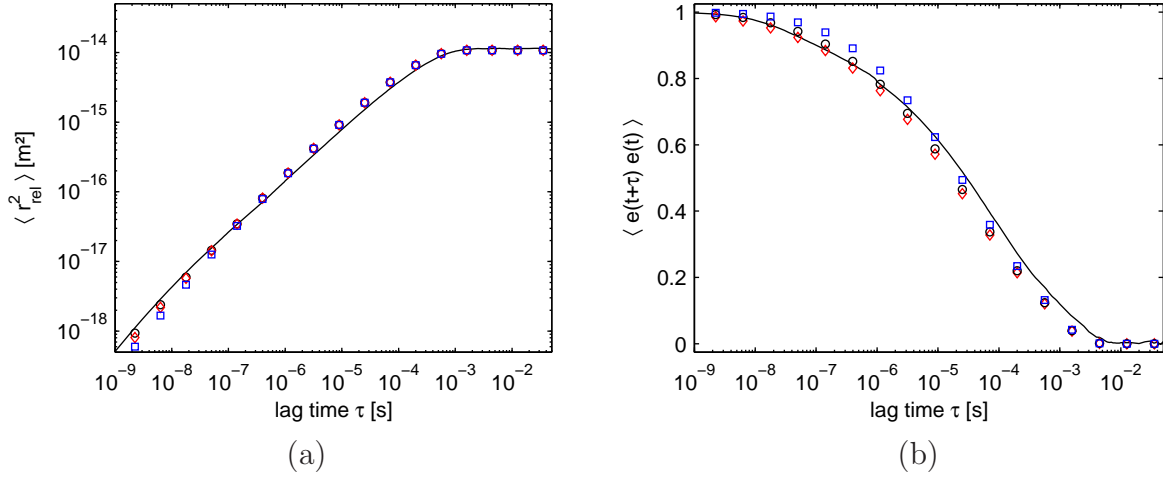


Figure 4.6: (a) The figure shows the MSD $\langle r_{\text{rel}}^2 \rangle$ of the DNA monomer relative to the center-of-mass for linear DNA (*solid*). The symbols indicate the analytical prediction for the internal motion of a linear Gaussian semiflexible chain. Besides the curves for a mode cutoff $\Lambda = 150$ (*circle*), also the curves for $\Lambda = 91$ (*diamond*) and $\Lambda = 45$ (*square*) were included in the figure. (b) The temporal correlation of the segment vector was calculated $\langle \vec{e}_i(t + \tau) \vec{e}_i(t) \rangle$ as obtained by the simulation (*line*) and the analytical solution according to Eq. (4.9) (*symbols*). The separation onto the contour was set to $l_0 = 5$ nm (*diamond*), $l_0 = 10$ nm (*circle*) and $l_0 = 20$ nm (*square*).

and no fitting parameters, the deviations between the simulation and the HWR model remain relatively small. Therefore we conclude that the simulation of linear DNA is reasonably well described by the analytical model. Consequently we have shown that the BD simulation of the discrete DNA model can be used to compute dynamic properties of semiflexible polymers. This validation encourages us to apply the BD simulation to the dynamics of superhelical DNA, for which no consistent analytical theory is still available.

Discretization

The analytical approach allows us to make some statements regarding the effect of discretization. The monomer motions at small length scales or equivalently at short times are the most sensitive to the discrete nature of the DNA model. We can mimic the discretization by setting the high-frequency cutoff Λ to smaller values, therefore excluding the contributions of the highest normal modes. Since each mode is associated with a certain length scale, the cutoff approximates the influence of the discrete segment length in the simulation. Consequently motions on smaller length scales, corresponding to modes beyond the cutoff, are disregarded. As seen in Fig. (4.6a) significant deviations for the internal motion $\langle r_{\text{rel}}^2 \rangle$ by changing the cutoff Λ to smaller values arise only in the limit of small times $t < 10^{-7}$ s.

The segment vector \vec{e}_i is closely connected with the chosen equilibrium segment length

l_0 , therefore it is necessary to study the effect of discretization of the simulated polymer. Within the HWR model the correlation $\langle \vec{e}_i(t + \tau) \vec{e}_i(t) \rangle$ can be calculated according to Eq. (4.9) as function of the separation l_0 on the contour. Here the following values for the separation were considered: $l_0 = 5$ nm, $l_0 = 10$ nm and $l_0 = 20$ nm. From Fig. (4.6b) we can infer that for large times t due to the exponential term the differences vanish. On the other hand for very short times the contributions of the modes, which are relevant on the length scale of discretization, become negligible. Therefore differences between the discretizations are visible only on intermediate time scales. A finer resolution with a segment length $l_0 = 5$ nm added only small corrections with respect to the segment length $l_0 = 10$ nm.

Thus, we have verified that the HWR model coincides reasonably well with the BD simulation. In a second step we have also checked with the analytical description that the effect of discretization does only introduce minor corrections to the polymer dynamics. The used value of $l_0 = 10$ nm for the segment length throughout the simulations is therefore a good trade-off between computational time and accuracy.

4.2.2 Barkley-Zimm model

The reorientation of the DNA molecule as outlined in section (2.1.3) can be described by DNA as a uniform elastic rod that bends and twists in a viscous medium in the framework of the Barkley-Zimm theory. Barkley and Zimm applied the theory to experimental data of nanosecond fluorescence spectroscopy, which allows to measure the DNA rotation. Dyes such as ethidium bind to DNA by intercalation between two base pairs, such that the transition dipole moment of ethidium lies in the plane of the dye. The dye is excited with polarized light, and consequently the decay of the emitted fluorescence intensity of the horizontal and perpendicular components relative to the initial polarization vector is monitored, which allows to determine the reorientation of the fluorescent dye embedded in DNA with time. The established lifetime of DNA-intercalated ethidium bromide is about $\approx 20 - 25$ ns, therefore it is assumed that the main contributions to the fluorescence decay arise from very fast motions. In a realization of this kind of experiment [Wahl et al., 1970] a rapid decay of the fluorescence polarization was identified with a decay time $\tau \approx 28$ ns. The Barkley-Zimm theory predicts the general shape of the fluorescence decay curves. Further it was shown that the contributions from bending remain small at the nanosecond timescale, which can be rationalized as rotations around the helical axis take place on shorter time scales as for rotations perpendicular to the helical axis.

Since reorientations of the helical axis are much slower than rotations around the helical axis, we restrict the considerations onto only the twisting motions for time scales of nanoseconds and neglect the small contributions from bending of the helical axis. The orientation of DNA is recorded within the BD simulation with the \vec{f} -vector, which lies in the plane perpendicular to the segment vector in the local reference frame. Then the distribution $\psi(\gamma, \tau | \gamma_0, 0)$ as given by Eq. (2.22) allows to describe analytically the temporal correlations of the \vec{f} -vector. The equation expresses how the rotation angle

γ on a specific site on DNA is distributed as a function of time, starting with a given initial rotation angle γ_0 and the system in thermal equilibrium. It should be noted that the angle between $\vec{f}(\tau)$ and $\vec{f}(0)$ is exactly given by the difference $\gamma(\tau) - \gamma_0$ of the rotation angle at lag time τ and the initial angle. The following expression was derived to calculate the temporal correlation:

$$\begin{aligned} \langle \vec{f}(\tau) \vec{f}(0) \rangle &= \langle \cos(\gamma(\tau) - \gamma_0) \rangle \\ &= \int_{-\infty}^{\infty} d\gamma \psi(\gamma, \tau | \gamma_0, 0) \cos(\gamma(\tau) - \gamma_0). \end{aligned} \quad (4.10)$$

These parameters were assumed in the calculations: DNA of length $L = 910$ nm and the circular DNA cross-section is defined according to the hydrodynamic DNA radius $r_{\text{HD}} = 1.2$ nm. Further the same torsional rigidity $C = 2.5 \times 10^{-19}$ erg cm as in the DNA model was chosen. In Eq. (2.23) the sum is truncated at $\Lambda' = 150$, which corresponds to a wave length $l_{\Lambda'} = 2\pi/\lambda_{\Lambda'} = L/\Lambda' < l_0$ and a time scale $\tau_{\Lambda'} = 1/\sigma\lambda_{\Lambda'}^2 \ll 10^{-9}$ s.

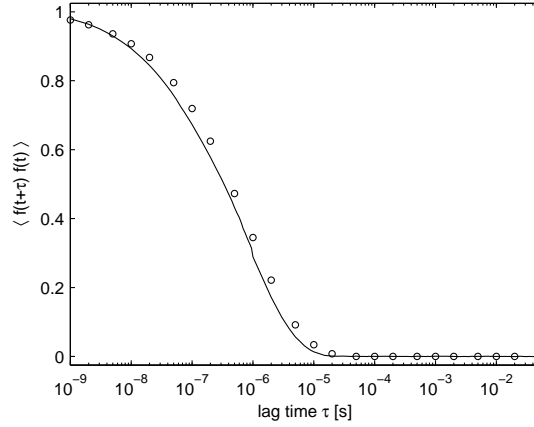


Figure 4.7: The comparison between the temporal correlation $\langle \vec{f}(t + \tau) \vec{f}(t) \rangle$ for linear DNA as calculated from the simulation data (*line*) and Barkley-Zimm model of the torsional DNA motions (*circles*) is shown.

In Fig. (4.7) the reorientation of the \vec{f} -vector due to twisting motions as calculated from the analytical model together with the simulation data is depicted. We conclude from the good agreement between the simulation data and the analytical calculations, that the reorientation of the \vec{f} -vector on the nanosecond timescale in the simulation can be explained solely by twisting motions.

4.3 Circular DNA with permanently bent sequences

In a preceding section it was argued that DNA segments, which are located temporally in end loops, are accelerated. This finding might indicate that the experimentally observed acceleration of dynamics with increasing linking number difference in [Shusterman et al., 2008] might stem from the shift of the labeled position towards the end

loop regions. For the studied pUC18 plasmid it is known that it contains naturally curved sequences [Muzard et al., 1990, Kremer et al., 1993]. The effect of a permanently bent sequence is to organize the global structure by increasing the probability at high superhelical densities for an end loop in vicinity of the bent sequence [Kremer et al., 1993]. Direct evidence for the positioning of sequence-directed bends at end loops has been obtained by electron microscopy [Laundon and Griffith, 1988]. In the following we want to address the question to what extent the insertion of a bent sequence effects the single monomer dynamics.

DNA conformations with permanently bent sequences

BD simulations of circular DNA with an inserted bent sequence have been performed. A permanently bent sequence was introduced into the DNA chain by assigning at three adjacent joints a bending angle θ^* of 40° lying in the same bending plane ($\phi^* = 0^\circ$), such that the sequence spans a total bending angle of 120° .

In Fig. (4.8) it is checked that for relaxed DNA the mean local writhe equals $\langle\omega\rangle = 0$. Introducing additional torsional strain the mean local writhe $\langle\omega\rangle$ is shifted by a constant value, such that the probability for end loop formation is distributed uniformly along the DNA chain. In the case of an insertion of a bent sequence at arbitrary bead positions $i = 0, 1$ and 2 , the bent sequence is correlated with the maximum of the average local writhe. In addition as reported in [Kremer et al., 1993, Klenin et al., 1995] an 'echo' peak of the mean local writhe appeared at the opposing position at approximately 50 % of the contour length L relative to the bent sequence. As shown for DNA without an inserted bent sequence, the maximum in local writhe corresponded to end loops. The 'echo' peak position depends on the overall DNA length as for longer DNA molecules the probability of branching increases. The formation of an 'echo' end loop at the opposing DNA position is consistent with no or small probability of branching.

We investigated the dynamics of single monomers as a function of the distance from the bent sequence, using two basic configurations:

- In one configuration of the system the labeled bead was placed directly at the bent sequence, such that the labeled bead remained a longer fraction of time in end loops.
- For the second configuration the fact was considered that an 'echo' end loop appeared at the opposing position at $\approx 50\%$ of the contour length relative to the bent sequence in unbranched superhelical conformations. Therefore in order to probe the dynamics in the stem region of the plectonemic structure, the labeled bead has been positioned at $\approx 25\%$ of the contour length relative to the bent sequence. The symmetrical positioning between the bent sequence favouring end loops and the 'echo' loop lead to a reduced probability of an end loop formation at the labeled bead.

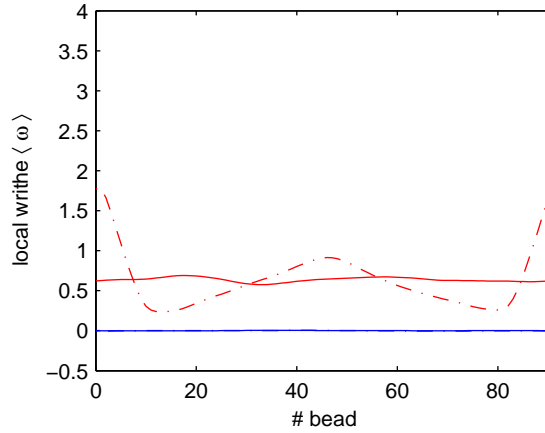


Figure 4.8: Mean local writhe $\langle \omega \rangle$ as a function of the bead position. Circular DNA in the relaxed state (*blue*) and at $\Delta Lk = -10$ (*red*) was calculated with inserted permanently bent sequences at bead positions 0-2 (*dot-dashed*) and without bent sequences (*solid*). For relaxed DNA ($\Delta Lk = 0$) with and without bent sequences the curves have zero mean local writhe ($\langle \omega \rangle = 0$).

Translational diffusion coefficient

The translational diffusion coefficients are obtained by repeating the same calculations as done for unbent circular DNA. The slope of the center-of-mass MSD yields a translational diffusion coefficient $D_t = 4.9 \mu\text{m}^2\text{s}^{-1}$ for $\Delta Lk = -10$ and $D_t = 4.4 \mu\text{m}^2\text{s}^{-1}$ in the case of relaxed DNA.

The size of the molecule can be characterized by the square radius of gyration:

$$\langle R_g^2 \rangle = \frac{1}{N} \sum_{i=1}^N \sum_{j=1}^N \langle (\vec{r}_i - \vec{r}_j)^2 \rangle. \quad (4.11)$$

MC simulations as described in section (3.8.1) were performed with 10^8 simulation steps. In the radius of gyration calculation according to Eq. (4.11) only every 1000th DNA conformation was included. Tab. (4.2) summarizes the results for DNA rings with and without bent sequences and different linking number differences.

$\langle R_g^2 \rangle^{1/2}$ [nm]	unbent	bent
$\Delta Lk = 0$	84.5	82.7
$\Delta Lk = -4$	69.0	68.8
$\Delta Lk = -10$	63.6	62.1

Table 4.2: Radius of gyration $\langle R_g^2 \rangle^{1/2}$ calculated from MC simulations for circular DNA with and without bent sequences at different linking number differences.

The size of the polymer decreases with increasing superhelical density $|\sigma|$. The bent sequence induced only an additional minor shrinking of the polymer size.

Internal motion of single DNA monomers

In Fig. (4.9a) the MSD $\langle r_{\text{rel}}^2 \rangle$ of the DNA monomer relative to the center-of-mass with an intrinsically bent sequence is plotted versus time. The positioning of the labeled bead directly at the bent sequence enhanced its internal motion, while for the second configuration with the labeled bead at a separation of $\approx 25\%$ of the contour length from the bent sequence the MSD is reduced. The separation of the MSD curves for the two considered configurations is more pronounced at higher superhelical densities. This can be explained by the formation of a plectonemic structure with a stem region and terminal end loops. For circular DNA without permanently bent sequences we already showed that the monomer motion in the vicinity of an end loop is accelerated. Further the probability of end loops is increased directly at the bent sequence, as the naturally curved sequence favours energetically the end loop formation. Therefore the labeled bead at the bent sequence remains in end loops for a larger fraction of time, and displays consequently faster dynamics. On the other hand in the second configuration the labeled bead is positioned predominantly in the stem region between the terminal loops. The motion is therefore suppressed due to the tight interwound structure, which is created by the DNA itself.

Mean-square displacement of single DNA monomers

The total MSD is the superposition of internal motion and center-of-mass diffusion, which is depicted in Fig. (4.9b).

For superhelical DNA at $\Delta Lk = -10$ the accelerated internal motion at the bent site is overlaid by the fast translational diffusion due to the compact size of the polymer. Therefore the two motions cooperatively reinforce the acceleration of about 12 – 13% of the MSD compared to the relaxed DNA at intermediate times $\tau = 10 - 100 \mu\text{s}$ (see Tab. (4.1)). On the other hand the difference between the MSD curves for $\Delta Lk = 0$ and $\Delta Lk = -10$ is diminished due to the opposing trends of the center-of-mass diffusion and the internal dynamics, when the labeled bead is positioned at 25% of the contour length away from the bead.

4.4 Polarization effects

In a recent study the single monomer dynamics of specially labeled superhelical DNA have been measured with fluorescence correlation spectroscopy (FCS) [Shusterman et al., 2008]. Classical experimental techniques, such as dynamic light scattering or transient electric birefringence deliver information only on large-scale shape fluctuations of macromolecules. FCS [Elson and Magde, 1974, Magde et al., 1974] is a powerful experimental method that allows to measure the dynamics of molecules in a variety of sample system. It has been used to measure (anomalous) diffusion [Wachsmuth et al., 2000, Weiss et al., 2004], flow [Magde et al., 1978, Koehler et al., 2000], fast rotational

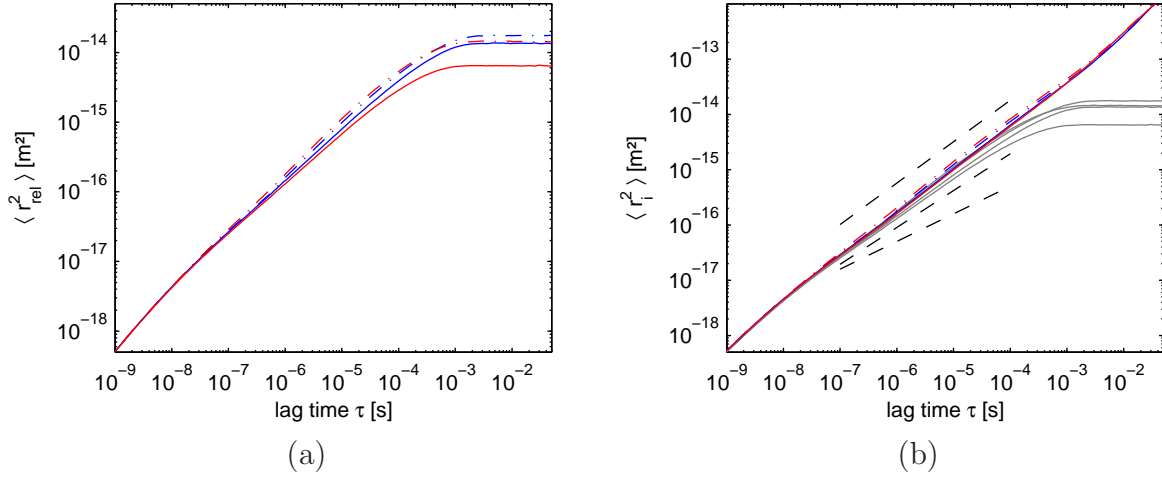


Figure 4.9: (a) The figure shows the MSD $\langle r_{\text{rel}}^2 \rangle$ of the DNA monomer relative to the center-of-mass for a superhelix with an intrinsically bent sequence. $\Delta Lk = 0$ (*blue*), $\Delta Lk = -10$ (*red*), at the bent sequence (*dot-dashed*), in a distance of $25\%L$ relative to the bent sequence (*solid*). (b) The total MSD $\langle r^2 \rangle$ is shown. The color coding is kept as in (a). The dashed line mark $\tau^{3/4}$ -, $\tau^{2/3}$ - and $\tau^{1/2}$ -power laws (*from top to bottom*) to guide the eye. In addition the contributions of the internal motions $\langle r_{\text{rel}}^2 \rangle$ taken from (a) are renewed (*grey*).

motion [Kask et al., 1987, 1989], photophysical properties [Widengren et al., 1995] and diverse chemical reactions [Elson and Magde, 1974] both in vitro and in vivo, i.e. in living cells. FCS is capable of resolving the internal dynamics of molecules that are larger than the focal volume [Lumma et al., 2003, Shusterman et al., 2004]. It is based on a correlation analysis of the fluorescence photons emitted by molecules that move in a tiny laser focus (typical volume of 1 femtolitre) inside the sample.

In the following the BD simulations is adapted to model FCS experiments. Therefore the motion of the fluorophore's dipole moment is explicitly taken into account and the effects of fluorophore excitation with partially polarized light are considered.

4.4.1 Fluorophore's dipole moment dynamics

At first the dynamics of the fluorophore's dipole moment was studied. The dipole vector of the fluorophore is represented by a constant vector \vec{p}_i in the local coordinate system $(\vec{f}_i, \vec{g}_i, \vec{e}_i)$ of an arbitrary, single segment i and can be expressed generally as a superposition of the \vec{e}_i - and \vec{f}_i -vector. The underlying assumption is that the dipole vector is rigidly attached to one DNA segment and follows strictly the translational and rotational motion of the segment. A schematic view of the fluorophore attachment to superhelical DNA is depicted in Fig. (4.10).

In the FCS experiments with superhelical DNA [Shusterman et al., 2008] a single fluorophore is attached to the DNA by binding it to a third DNA strand that subsequently forms a triple helix according to the protocol developed in [Pfannschmidt et al., 1996]. One end of the intercalating strand is then fixed covalently to the DNA ring. Under

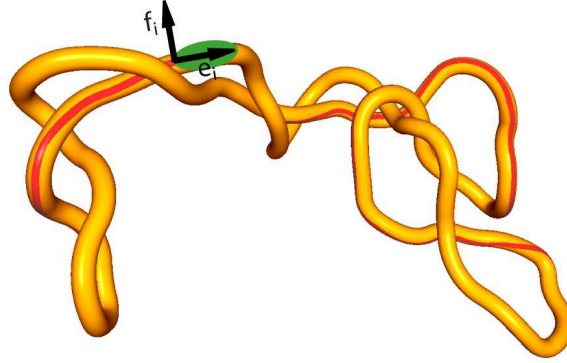


Figure 4.10: A representative superhelical conformation at a linking number difference $\Delta Lk = -10$ is shown. Schematically a fluorophore (green oval) is attached to the DNA. The fluorophore's orientation is described by the local coordinate system $(\vec{f}_i, \vec{g}_i, \vec{e}_i)$.

certain experimental conditions this structure is known to be quite stable, which should make the fluorophore's dipole moment follow the DNA ring dynamics. When the triple helix is destabilized the fluorophore is connected to the DNA by a freely moving 10 nucleotide linker and thus the dipole moment's direction should no longer correlate with the DNA conformation.

The rotating dipole moment is known to introduce an additional decay term into the FCS autocorrelation, which is related to the dipole vector angular correlations $\langle \vec{p}_i(t + \tau) \vec{p}_i(t) \rangle$. We considered from all possible orientations of the dipole vector \vec{p}_i in the local reference frame, two basic configurations. In the first configuration the dipole vector \vec{p}_i is aligned in the direction of the segment vector \vec{e}_i , and in the second configuration the dipole vector lies in the plane perpendicular to the segment vector, parallel to the unit vector \vec{f}_i . The general case can then be deduced from the two studied orientations.

- From Fig. (4.11a) one can infer that the decay curve for a relaxed DNA circle at 25% L from the bent sequence remains mostly unchanged compared to linear DNA. This correlation curves match also perfectly those for circular DNA without intrinsic bends (not shown in Fig. (4.11)).

In contrast if additional torsional strain is added into DNA rings the dipole vector decorrelates faster ($\vec{p}_i \parallel \vec{e}_i$), which is even enhanced if the fluorophore is attached directly at the bent sequence. Bent sequences increase the formation probability of end loops, which are related to faster motion of beads \vec{r}_i within end loop. Since the segment vector $\vec{e}_i = (\vec{r}_i - \vec{r}_{i-1})/|\vec{r}_i - \vec{r}_{i-1}|$ is a function of \vec{r}_i , the reorientation of the dipole vector along the direction of the segment vector is also accelerated.

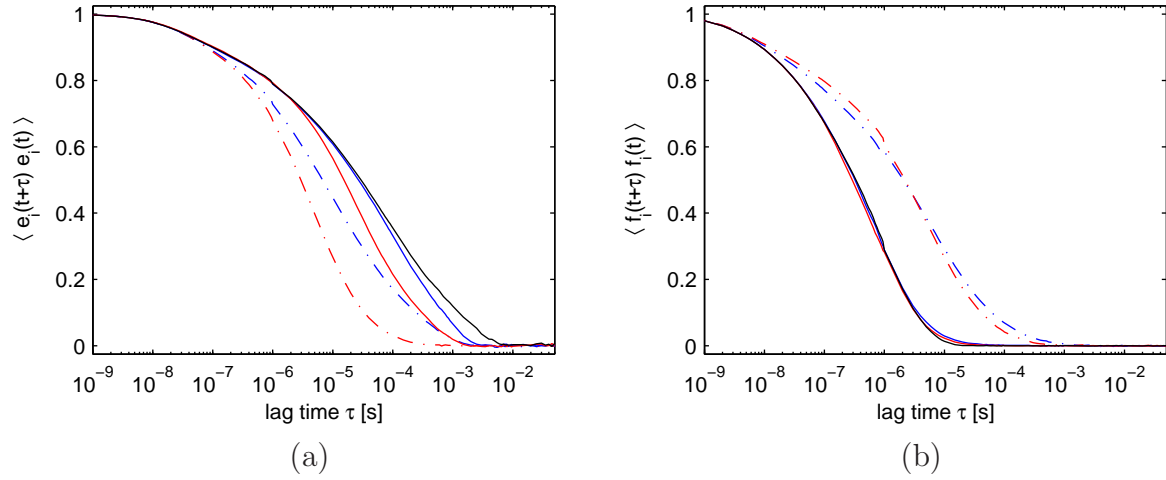


Figure 4.11: The figure shows the calculated angular correlation of the dipole vector $\langle \vec{p}_i(t+\tau) \cdot \vec{p}_i(t) \rangle$. The labeled bead was positioned directly at the bent sequence (*dot-dashed*), while in a second case the labeled bead was introduced in a distance of 25% of the total DNA contour length from the bend (*solid*) ($\Delta Lk = 0$ (*blue*); $\Delta Lk = -10$ (*red*)). For comparison a linear DNA fragment is included (*solid black*). In (a) the dipole vector \vec{p}_i was aligned parallel to the helix axis ($\vec{p}_i \parallel \vec{e}_i$) and in (b) perpendicular to the helix axis ($\vec{p}_i \parallel \vec{f}_i$).

For the considered configurations the decay of the angular correlation occurs on time scales of 10..100 μ s.

- The dynamics of the dipole vector perpendicular to the helical DNA axis ($\vec{p}_i \parallel \vec{f}_i$) is clearly separated by two orders of magnitude from the case of the dipole vector parallel to the helical DNA axis ($\vec{p}_i \parallel \vec{e}_i$) (see Fig. (4.11)). For this configuration circular DNA without bent sequences or a shifted positioning of the labeled bead relative to the bent sequence exhibited no difference from linear DNA. In contrast at the bent sequence the decorrelation of the \vec{f}_i -vector is slowed down to time scales comparable to those of the segment vector \vec{e}_i , which indicates that the motions are not independent from each other. An explanation of this coupling might be provided by considering that at equilibrium the segments in the bent sequence make a total bend of 120° in a plane configuration. Torsional stress on a segment in the bent sequence, makes it rotate around the axis of adjacent segments, since the neighboring segments are not coaxial. Thus displacing the segment from the bending plane in which the DNA was initially located. But the rotation of segments out of the equilibrium bending plane is counteracted by bending forces, therefore as a consequence suppressing the twisting motion. As a result of the coupling of twisting and bending motions, the decorrelation of the \vec{f}_i -vector occurs then due to rotation of the whole bent sequence, which is much slower.

4.4.2 FCS simulation

In the following the BD simulation results were compared with experimental FCS data. This part of the work was done in collaboration with J.Krieger. The simulated trajectories were used to calculate the expected fluorescence intensity $I(t)$ for a labeled DNA diffusing through the focus of a FCS setup. The fluorescence intensity $I(t)$ and the normalized autocorrelation curve $g(\tau) = \langle I(t + \tau) I(t) \rangle / \langle I \rangle^2$ were calculated with a FCS simulation toolbox, developed by J.Krieger [Krieger, 2009].

Here we shortly summarize the basic principles of the FCS simulation toolbox. Each trajectory is a time series of the spatial positions of a single bead $\vec{r}_i(t)$ to which the fluorophore is attached. It may also contain the orientations $\hat{p}_i(t)$ ($|\hat{p}_i(t)| = 1$) of the fluorophore's dipole vector, which can be represented as a superposition of the vectors \vec{e}_i and \vec{f}_i in the local reference frame. The dipole vector accounts for the interaction of (partially) polarized excitation light with the fluorophore. If a fraction $F_{\text{pol}} \in [0, 1]$ of the excitation light is linearly polarized, parallel to a unit vector $\hat{e}_{\text{ex}} = (1, 0, 0)$, then according to [Aragón and Pecora, 1975] the excitation probability is reduced:

$$f_{\text{pol}}(\hat{p}_i(t)) = (1 - F_{\text{pol}}) + F_{\text{pol}} \cdot (\langle \hat{e}_{\text{ex}}, \hat{p}_i(t) \rangle)^2 \leq 1, \quad (4.12)$$

where $\langle \cdot, \cdot \rangle$ denotes the Euclidean scalar product. The number of detected photons $N_{\text{phot}}(t) \propto I(t)$ is calculated by first estimating the average number $\overline{N}_{\text{phot}}(t)$ of photons expected in one simulation step $[t, t + \Delta t_{\text{FCS}}]$. Then $N_{\text{phot}}(t)$ is drawn from a Poissonian distribution with average $\overline{N}_{\text{phot}}(t)$. This procedure accounts for the counting statistics of the photon detection. The expected photon number is given as

$$\overline{N}_{\text{phot}}(t) = \overline{N}_0 \cdot \Delta t_{\text{FCS}} \cdot \sum_{i=1}^K q_{\text{f}} \cdot q_{\text{det}} \cdot h(\vec{r}_i)^2 \cdot f_{\text{pol}}(\hat{p}_i(t)). \quad (4.13)$$

Here K denotes the number of fluorophores near the laser focus, \overline{N}_0 is the maximum number of possibly detected photons per fluorophore and time step, while q_{f} and q_{det} are the quantum efficiencies of fluorescence and detection, respectively. The form of the excitation and detection profile, which are assumed to be identical and completely overlapping, is described by

$$h(x, y, z) = \exp \left(-2 \cdot \frac{x^2 + y^2}{w_{\text{xy}}^2} - 2 \cdot \frac{z^2}{\gamma_{\text{FCS}}^2 w_{\text{xy}}^2} \right). \quad (4.14)$$

The lateral width of the profile is w_{xy} and $\gamma_{\text{FCS}} = w_z/w_{\text{xy}}$ is its aspect ratio, where w_z is the focal width in z direction.

The photophysical dynamics such as bleaching or triplet blinking are neglected in the system as the goal is to observe the effects of the DNA motion. The photophysics could be introduced into the simulation by making the fluorescence efficiency q_{f} time dependent and changing it for every particle with a suitable simulation. A full simulation, but without the effects of polarization has been described in [Dix et al., 2006]. In real

experiments care has to be taken to discriminate inevitable photophysical effects from the other contributions to the measured correlation function. The typical timescale of the triplet dynamics is $[0.1\mu\text{s}, 10\mu\text{s}]$ [Widengren et al., 1995], which is near the expected effect of rotational dynamics.

For the simulations the trajectories were shifted in time and space so that they pass the focus consecutively. Each trajectory of length M was shifted to satisfy $\vec{r}_i(M/2) \equiv 0$. This ensures that in average there is less than one particle in the focus which mimics real experiments in strongly diluted solutions. In order to still obtain reasonable photon statistics from only few trajectories that were simulated, the fluorescence efficiency was raised to an unrealistically high value of $q_f = 10$. The simulations were compared for $q_f < 1$ and $q_f = 10$ finding that this change improved the statistics but did not change the results in any other respect. Refer to Tab. 4.3 for an overview of the FCS simulation parameters used to generate the data.

Parameter	Description	Value
Δt_{FCS}	FCS simulation time step	$1 \mu\text{s}$
$T_{\text{trajectory}}$	single trajectory length	0.5 s
\overline{N}_0	absorbed photons per molecule	$\approx 6 \cdot 10^6 \text{ s}^{-1}$
w_{xy}	lateral width of excitation profile	$0.5 \mu\text{m}$
q_f	fluorescence quantum yield	10
q_{det}	detection efficiency	0.1
$\hat{\epsilon}$	excitation light polarization	$(1, 0, 0)$
γ_{FCS}	focus aspect ratio	1

Table 4.3: FCS simulation parameter values for DNA simulations.

FCS autocorrelation curves

In the FCS study [Shusterman et al., 2008] the temporal kinetics of single monomer MSD in DNA rings with defined degrees of superhelicity was presented. A pUC18 plasmid was tagged with a fluorophore according to the procedure described in section (4.4.1). The FCS setup yielded the autocorrelation function $g(\tau)$, which contained information about the motion of a single DNA segment.

As described in [Petrov et al., 2006, Shusterman et al., 2008] for independent point sources of fluorescence subject to random forces, moving in a Gaussian focus, the following relation holds between $g(\tau)$ and $\langle r_i^2(\tau) \rangle$

$$g(\tau) = g_0 \left(1 + \frac{2 \langle r_i^2(\tau) \rangle^2}{3 \omega_{\text{xy}}^2} \right)^{-1} \left(1 + \frac{2 \langle r_i^2(\tau) \rangle}{3 \gamma^2 \omega_{\text{xy}}^2} \right)^{-\frac{1}{2}}. \quad (4.15)$$

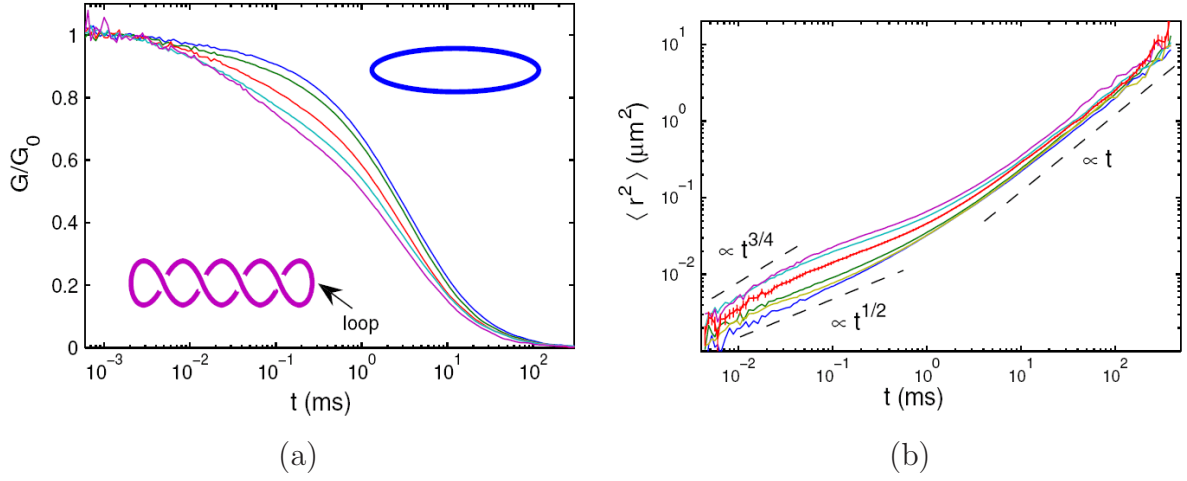


Figure 4.12: Experimental FCS data on superhelical dynamics have been measured by Shusterman et al. (a) FCS correlation functions for pUC18 topoisomers with ΔLk : 0 (blue), -1 (green), -2 (red), -3 (cyan), and -4 (magenta). Insets show schematically the relaxed (top right) and plectonemic (bottom left) DNA conformations. (b) Temporal dependences of segmental MSD for different linking numbers ΔLk . (Adopted from [Shusterman et al., 2008])

In the equation g_0 is a normalization constant, determined from the behavior of $g(\tau)$ at short time scales. Eq. (4.15) was used to convert the autocorrelation function into the MSD $\langle r_i^2(\tau) \rangle$.

In Fig. (4.12a) the experimental FCS autocorrelation curves from [Shusterman et al., 2008] are included, while Fig. (4.12b) depicts the corresponding calculated MSD with help of Eq. (4.15). The following findings were obtained in the experimental study. The introduction of superhelicity leads to progressively faster dynamics on all time scales, including the long time regime corresponding to coil diffusion and the short time regime corresponding to segmental motion within the DNA coil. Three different regimes were identified: (a) a long time regime in which the labeled segment obeys the normal diffusion law, (b) an intermediate regime at $\tau \approx 100 \mu s$ displaying subdiffusive motion of the labeled segment within the polymer coil and (c) at short times the motion is governed by dynamics of stiff polymers. Interestingly, on intermediate time scales the segmental dynamics showed characteristics reminiscent of a Rouse model. According to the Rouse model the MSD obeys a power-law $\propto t^{1/2}$ as summarized in section (2.1.2).

The FCS simulation toolbox allowed to generate from the BD trajectories as input data the corresponding FCS correlation curves. The resulting correlation curves are displayed in Fig. (4.13), which are normalized to satisfy $g(\Delta t_{FCS}) = 1$. In agreement with the simulated BD trajectories for circular DNA without intrinsic bent sequences the FCS correlation curves showed no separation depending on the superhelical density for short lag times τ (see Fig. (4.13a)). Only at longer times $\tau > \tilde{\tau}_1$ the correlation curves differ due to different translational diffusion coefficients D_t . If a bent sequence is inserted into DNA and the fluorophore is positioned at the bend, the FCS curves

split up at intermediate times (see Fig. (4.13b)). The curves are ordered according to the linking difference number, showing the slowest decorrelation for relaxed DNA and fastest for the structure with 10 additional twists. If the fluorophore is excited with 50 % partially polarized light the differentiation still persisted. For an increased focus aspect ratio $\gamma_{\text{FCS}} = 5$, which corresponds to a focus volume of an ellipsoid shape, the splitting decreased, but the FCS correlation curves were still clearly distinguishable.

Excitation with partially polarized light

As discussed in section (4.1) the MSD $\langle r_i^2(\tau) \rangle$ did display only two characteristic regimes, the dynamics of stiff polymers at short times and normal diffusion at long times. In contradiction Shusterman et al. [Shusterman et al., 2008] claimed that a third regime appeared at intermediate times. Here it was investigated if excitation of the fluorophore with partially polarized light can generate such kind of effect. The reasons for partial polarization of the excitation light in experiments may be manifold, but for example partial polarization in the focus may originate if a non-polarization maintaining fiber is used in the experimental setup.

In order to compare the results the same approach was applied as used for the experimental data to extract the MSD $\langle \vec{r}_i^2(\tau) \rangle$. The employed transformation between the correlation function and MSD is given by Eq. (4.15).

The results of the transformation applied to circular DNA with a fluorophore attached directly at the bent sequence, are summarized in Fig. (4.13d). If the fluorophore is excited with totally unpolarized light still only two regimes corresponding to the known stiff-rod limit ($\langle \vec{r}_i^2(\tau) \rangle \propto \tau^{3/4}$) and the normal diffusion ($\langle \vec{r}_i^2(\tau) \rangle \propto \tau$) are visible. The MSD curve for the plasmid with $\Delta Lk = -10$ lie on all time scales above the curve for the relaxed state considering the case of the labeled bead directly at the bent sequence. Excitation of the fluorophore with partially polarized light results in the appearance of a cross-over regime in between the stiff-rod limit and the translational diffusion. In the limit of long times τ the MSD curves still merge with the curves obtained by excitation with unpolarized light. The slope of the intermediate regime depends on the fraction of linearly polarized light F_{pol} , but the additional regime is independent of whether a bend has been inserted and of the position of the observed bead. For a 50% partial polarization of the excitation light the cross-over regime follows approximately a power law ($\langle \vec{r}_i^2(\tau) \rangle \propto \tau^{1/2}$) in the time range $\tau \approx 10 \dots 10^3 \mu\text{s}$. The time scale is in agreement with that of the experimentally found intermediate regime and therefore the rotational dynamics of the fluorophore's dipole moment might provide an explanation for the observation of a Rouse-like regime.

In conclusion the simulated FCS correlation curves exhibit the acceleration of the monomer with increasing superhelical density as claimed in the FCS experiment. But the statement has to be constrained by the condition that the fluorophore must be positioned in vicinity of the bent sequence. Overall the effect is significantly smaller than observed in the experiment. A possible explanation is that additional contributing terms to the correlation function e.g. triplet term, may alter the course of the curve

due to the normalization $g(t_{\text{FCS}}) = 1$ of the correlation curve.

We observed also an intermediate regime for excitation with partially polarized light, which can be attributed to the cross-over from rotational dynamics of the dipole vector to translational diffusion. The contributions of polarized excitation are commonly not visible in FCS experiments, as the decorrelation time of the dipole vector is well below the fastest resolvable time scale. For the simulations presented here, the dipole vector dynamics ($\vec{p}_i \parallel \vec{e}_i$) are slow enough to become accessible in experiments. Thus, we conclude that the intermediate regime originates from the visibility of two well separated decay terms for the translational and the rotational motion in the autocorrelation curve and polarization effects have to be taken into account in the analysis and interpretation of FCS data.

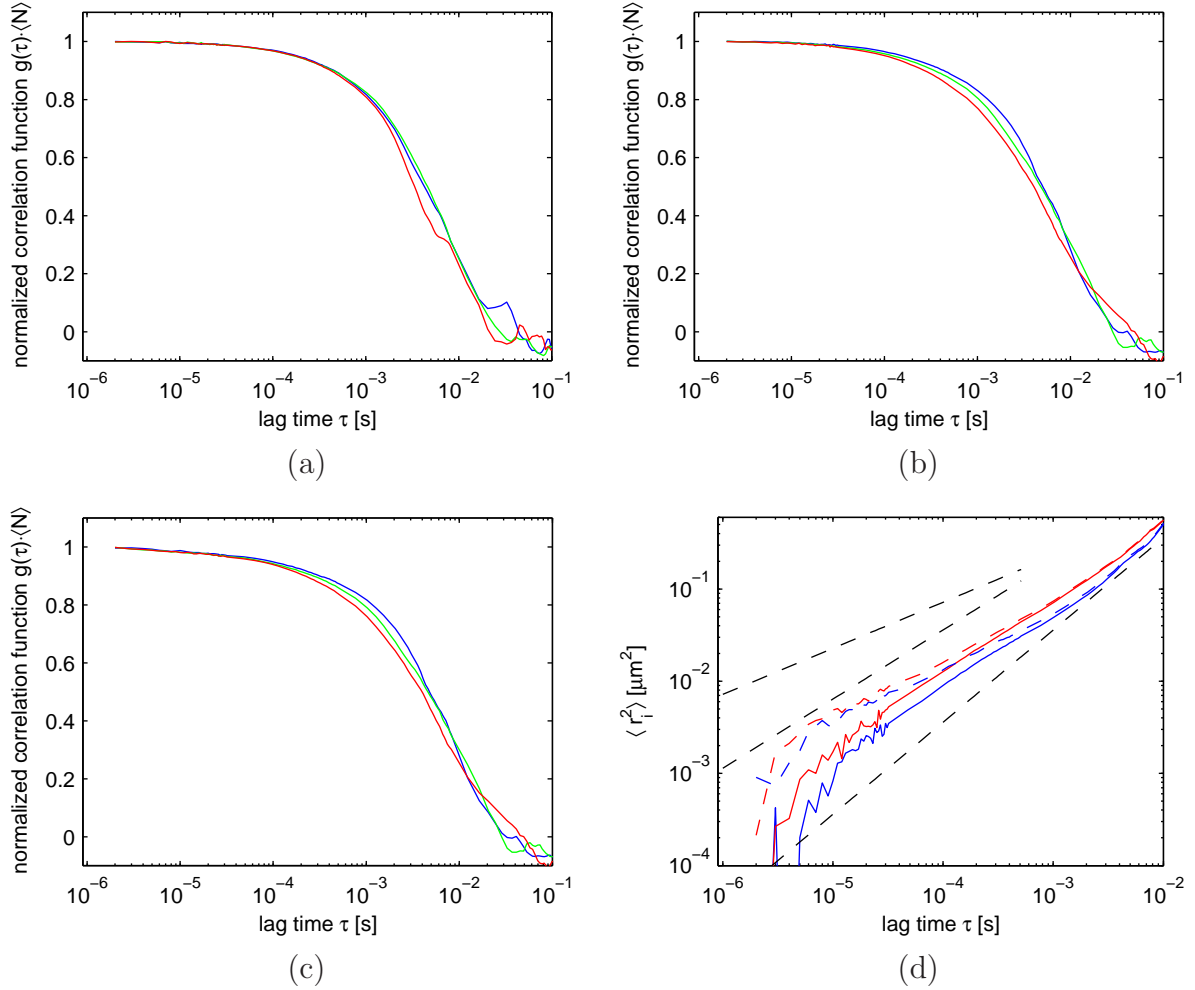


Figure 4.13: Figures (a)-(c) shows normalized correlation curves from the FCS simulation toolbox by J.Krieger for different linking number differences $\Delta Lk = 0$ (*blue*), $\Delta Lk = -4$ (*green*) and $\Delta Lk = -10$ (*red*). In (a) circular DNA without an intrinsic bend was studied, while the data for circular DNA directly at the bent sequence is shown for excitation (b) without polarized light and (c) with 50 % partially polarized light. The dipole vector was aligned in direction of the segment ($\vec{p}_i \parallel \vec{e}_i$). (d) The FSC correlation curves were converted into MSD as described in the text for the cases in (b) (*solid lines*) and (c) (*dashed lines*).

Chapter 5

Nucleosome dynamics

The previous chapter was devoted to the dynamics of circular DNA, which is a common form to store genetic information in bacteria and archaea. In eukaryotic cells, DNA is organized into a chromatin fiber with its basic packing unit, the nucleosome. This chapter focuses on the dynamics of conformational changes in nucleosomes. In the first part of the chapter equilibrium fluctuations of DNA from the histone core are considered, and equilibrium constants for DNA site exposure are determined within the nucleosome model. In the second part stretching experiments of single nucleosomes have been simulated, which allow to probe the intrinsic energy barriers and kinetic rate constants of the DNA unwrapping transition. At the end of the chapter stretching simulations are applied to oligonucleosomes.

5.1 DNA fluctuations at equilibrium

DNA sequences inside the nucleosome are largely inaccessible to many proteins due to the steric occlusion as a consequence of the proximity of DNA to the histone octamer. But regulatory proteins have to gain access to these buried DNA stretches in order to fulfill their biological function such as transcription, replication and repair. In vivo it is known that ATP-dependent remodeling enzymes facilitate the accessibility to nucleosomal DNA [Saha et al., 2006]. Alternatively it was proposed that nucleosomes are dynamic structures, which can spontaneously undergo conformational fluctuations, in which DNA is transiently released from the histone core [Polach and Widom, 1995]. Accessibility of target sites for regulatory proteins on nucleosomal DNA at equilibrium has been demonstrated by using restriction enzyme accessibility assays [Polach and Widom, 1995, Anderson and Widom, 2000]. Therefore Polach et al. inserted sites specific to a restriction enzyme at defined positions within the nucleosome. They obtained position-dependent equilibrium constants for target site exposure, which were in the range of $\approx 1 \times 10^{-2}$ to 4×10^{-2} for probe sites 3-15 bp relative to the end of DNA, which is organized in the nucleosome core particle. For probe sites buried deeper in the nucleosome (≈ 27 to 45 bp from the nucleosomal DNA end) the equilibrium constants were $\approx 5 \times 10^{-4}$ to 3×10^{-3} and $\approx 1 \times 10^{-5}$ to 1×10^{-4} for sites (54-72 bp from the nucleosomal DNA end) near the nucleosome symmetry axis or so-called dyad axis (located 72 bp from the nucleosomal DNA end).

Complementary experiments with Fluorescence Resonance Energy Transfer (FRET) also observed equilibrium fluctuations of DNA breathing. FRET can be used as a ruler on the molecular scale by measuring the distance-dependent energy transfer efficiency between an excited donor fluorophore to an acceptor molecule [Förster, 1948]. For nucleosomes it is possible to determine conformational distributions within an ensemble of molecules and the mononucleosome dynamics between different conformational states. Koopmans et al. [Koopmans et al., 2007] reported that a small fraction of intact nucleosomes ($\approx 3\%$) showed DNA breathing, which is consistent to the DNA detachment of 10 bp or less and a mean lifetime in the unwrapped state of 120 ms.

In the following BD trajectories have been calculated, in order to quantify fluctuations in the amount of DNA adsorbed to the histone core at equilibrium. For each data point we simulated a total of 9 trajectories, each with a simulated time of 3 ms. The key parameter, which was varied was the DNA-histone core adsorption energy density ϵ . It is used to reflect the varying strength of interactions between DNA and the histone core in the nucleosome. Several mechanisms in the cell influence the DNA affinity to the histone core.

- It is known that histone tail modifications play a central role not only in chromatin condensation on a large scale, but also in the nucleosome stability. Histone tail modification e.g. acetylation, where an acetyl group is attached to residues of the N-terminal histone tails, consequently reduces the overall positive charge of the histone core. In single-pair FRET it was shown that for end-labeled DNA acetylation leads to an opening of the nucleosome structure [Gansen et al., 2009].
- Studies also showed sequence-dependent binding affinities of DNA to histone core proteins [Lowary and Widom, 1998]. The nucleosome stability was found to be affected by the sequence [Gemmen et al., 2005]. Further the positioning of nucleosomes on DNA is related to the histone acetylation status and the DNA sequence [Krajewski, 2002].

Therefore the variability in the biological system is accounted for by a range of adsorption energy densities $\epsilon = \{6, 7, 8\} \text{ k}_\text{B}\text{T nm}^{-1}$ in this work.

The contour length of the adsorbed DNA is defined as the total length of the interacting segments. A segment is termed interacting, if the interaction distance $|\vec{R}_i|$ is within the cutoff distance r_0 , as defined in section (3.7). $P(n)$ is defined as the probability for being in a state with n interacting segments or the corresponding average contour length. The calculated probabilities are depicted in Fig. (5.1a). The effect of stronger interaction between the histone core and DNA, reflected by a higher adsorption energy density, is a shift towards a higher mean adsorbed contour length: 44.9 nm ($\epsilon = 6 \text{ k}_\text{B}\text{T nm}^{-1}$), 47.3 nm ($\epsilon = 7 \text{ k}_\text{B}\text{T nm}^{-1}$) and 47.8 nm ($\epsilon = 8 \text{ k}_\text{B}\text{T nm}^{-1}$). At the same time fluctuations allowing spontaneous unwrapping of the first turn are significantly suppressed, as can be inferred from Fig. (5.1a), since the probability distribution is narrowed.

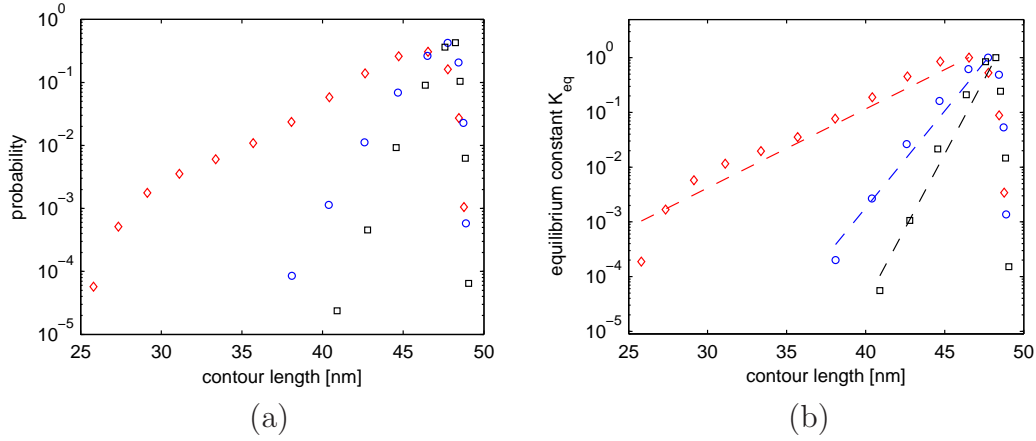


Figure 5.1: (a) Probability distribution of contour length adsorbed to the histone core at different adsorption energy densities $\epsilon = 6 \text{ k}_B\text{T nm}^{-1}$ (red diamonds), $\epsilon = 7 \text{ k}_B\text{T nm}^{-1}$ (blue circles), $\epsilon = 8 \text{ k}_B\text{T nm}^{-1}$ (black squares) (b) Equilibrium constants K_{eq} dependent on the amount of adsorbed DNA are shown. Dashed lines indicate fitting curves for the equilibrium constant.

The accessibility of DNA can be quantified by equilibrium constants $K_{\text{eq}}(n)$ depending on the number of interacting segments n . The equilibrium constant is given by the ratio between the probability $P(n)$ and the probability $P^{(\text{max})}$ at the reference state, which is defined as the most probable state.

The equilibrium constant is related to the energy associated with the DNA conformation $\Delta E^{(\text{conf})}$ in the nucleosome

$$K_{\text{eq}} = \exp\left(-\frac{\Delta E^{(\text{conf})}}{k_B T}\right). \quad (5.1)$$

The simplest assumption for the change in energy due to DNA detachment from the histone core is a linear function in the contour length of adsorbed DNA l , which reads $\Delta E^{(\text{conf})} = \epsilon^{(\text{net})} (l^{(\text{max})} - l)$. Here $\epsilon^{(\text{net})}$ denotes a net adsorption energy density and $l^{(\text{max})}$ is the contour length of adsorbed DNA in the reference state. The fit for the simulated equilibrium constants to Eq. (5.1) in the range $K_{\text{eq}} \leq 1$ yielded the following net adsorption densities $\epsilon^{(\text{net})} \approx 0.3 \text{ k}_B\text{T nm}^{-1}$, $\epsilon^{(\text{net})} \approx 0.8 \text{ k}_B\text{T nm}^{-1}$ and $\epsilon^{(\text{net})} \approx 1.3 \text{ k}_B\text{T nm}^{-1}$ in increasing order of the total energy adsorption densities. The net adsorption energy does not represent the pure adsorption energy but instead the net gain in energy due to adsorption to the histone core complex reduced by contributions from bending and electrostatic repulsion.

We did not observe for the considered short simulation times of 3 ms any contour length fluctuations corresponding to unwrapping of the second turn. This can be rationalized in a first approximation by the fact that the first DNA senses the presence of the second DNA turn, which is equally charged, therefore exerting an electrostatic

repulsion force on the first turn [Kulić and Schiessel, 2004]. The unwrapping of the first turn is therefore facilitated, while the second turn is more strongly bound to the histone core.

In order to relate the DNA fluctuations to experimental data, a probability $\tilde{P}(i)$ for each i th DNA segment to interact with the histone core was calculated. Therefore an equilibrium constant for site exposure $(1 - \tilde{P}(i)) / \tilde{P}(i)$ could be assigned to each DNA site. In Fig. (5.2) the simulated equilibrium constant for site exposure were compared to experimental values as reported by [Polach and Widom, 1995]. The experimentally measured equilibrium constants fall into the range of simulated data for energy adsorption densities between $6 \text{ k}_B\text{T nm}^{-1}$ and $7 \text{ k}_B\text{T nm}^{-1}$. The BD simulations are consistent with observed DNA fluctuations, which allow proteins to gain access to DNA target sites in the nucleosome.

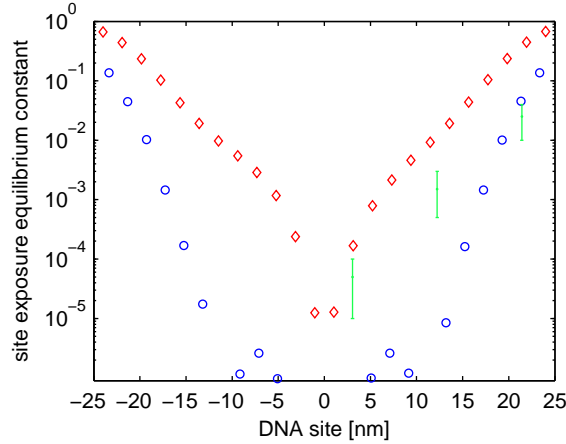


Figure 5.2: Equilibrium constant of DNA site exposure dependent on the site position relative to the dyad axis in the nucleosome ($\epsilon = 6 \text{ k}_B\text{T nm}^{-1}$ (red diamonds) and $\epsilon = 7 \text{ k}_B\text{T nm}^{-1}$ (blue circles)) Included are experimentally measured site exposure equilibrium constant (green) from [Polach and Widom, 1995] as described in the text.

5.2 Nucleosome stretching simulations

For the BD simulations in the following section nucleosomes were analyzed under the application of an external force. An external force facilitates the unwrapping of DNA in the nucleosome, which results in a faster dynamics of the unwrapping transition. Only the shift from relative slow transition times at zero external force to faster time scales under external force, makes it possible to study the unwrapping in experiments as well as simulations.

5.2.1 Nucleosome conformations

During the unwrapping from the initial to the final state the nucleosome system traverses several transitional conformations. The initial state was prepared according to the protocol described in section (3.7). The resulting starting point for the BD simulations is an equilibrated conformation, where DNA is wrapped tightly around the protein complex. The contour length of adsorbed DNA is then given by the calculated distributions in (5.1). A typical initial conformation is depicted in Fig. (5.4a) with a mean adsorbed contour length ≈ 48 nm for an energy adsorption density $\epsilon = 8 \text{ k}_\text{B} \text{ T nm}^{-1}$.

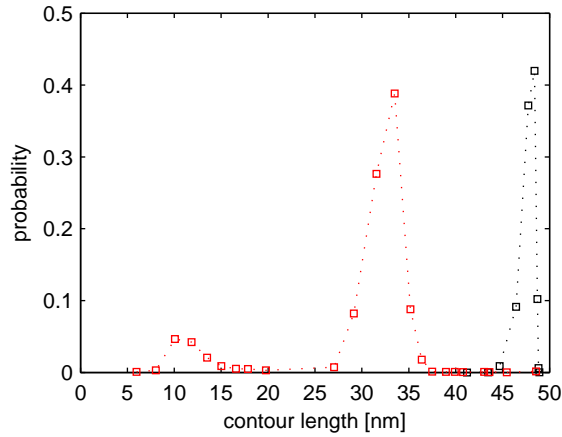


Figure 5.3: The probability distribution of contour length adsorbed to the histone core is shown in the presence and absence of an applied external force. The state at zero external force (*black squares*) and a constant external force of 15 pN (*red squares*) were considered ($\epsilon = 8 \text{ k}_\text{B} \text{ T nm}^{-1}$).

The effect of a constant external force applied to the DNA ends is to shift the adsorbed contour length probability distribution towards the unwrapped state. A comparison of the probability distribution of the ground state and a simulation with a constant external force of 15 pN is shown in Fig. (5.3). At 15 pN a second peak emerges at ≈ 10 nm adsorbed DNA contour length corresponding to the nearly unwrapped nucleosome state, while the peak at $\approx 30 - 35$ nm represents states with approximately one fully wrapped DNA turn. In contrast, nucleosome conformations with half windings are suppressed. At sufficiently large forces the system can therefore be approximated by a two-state system with one state representing the wrapped state with one wrapped DNA turn and a second unwrapped state with nearly no DNA bound to the histone core. A major part of this work is to quantify the kinetics of the transition between the two states based on the simulations. More precisely a goal is to determine the kinetic escape rate $k(F)$ from the wrapped state s_w to the unwrapped state s_u as a function of the applied external force:

$$s_w \xrightarrow{k(F)} s_u$$

In the following simulations were carried out at a constant stretching velocity. From time $t = 0$ the DNA end segments were displaced relative to each other with a constant stretching velocity \vec{v} . The absolute value is denoted by $v = |\vec{v}|$. In the work a range of stretching velocities $v = \{0.0025, 0.005, 0.01, 0.05, 0.1, 0.5, 1.0\} \text{ cm s}^{-1}$ were used to test the conformational transition. Fig. (5.4) shows the temporal evolution of the nucleosome conformation taken from the BD time trajectory at selected time points. The snapshots were taken for a stretching velocity $v = 0.1 \text{ cm s}^{-1}$. Simultaneously the amount of adsorbed DNA contour length to the histone core was recorded during the unwrapping transition, which is summarized in Fig. (5.5).

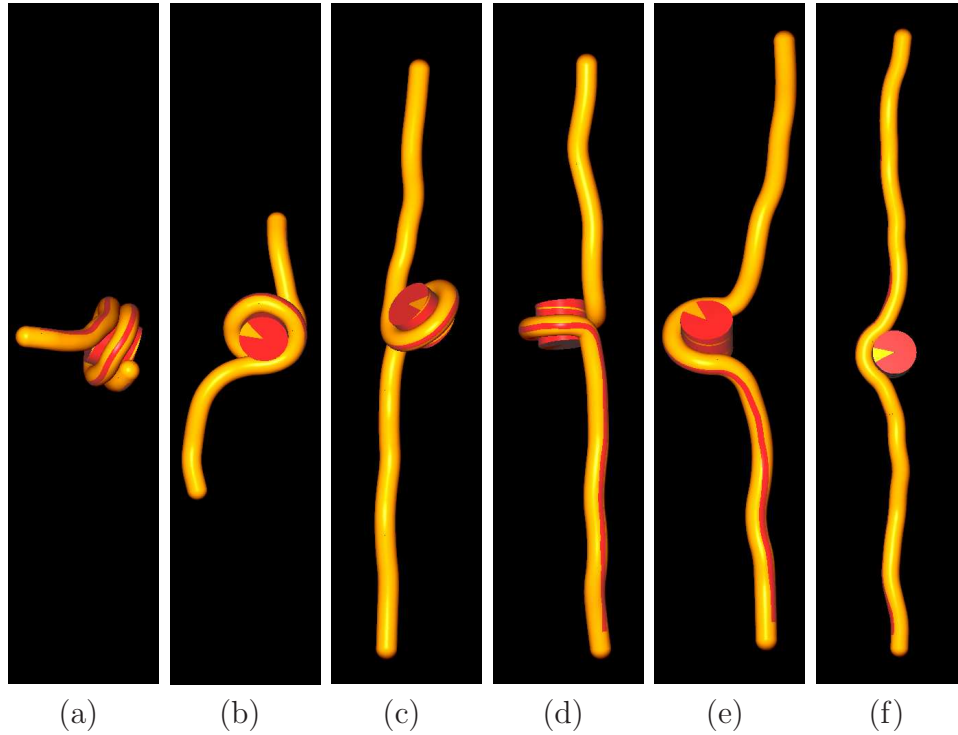


Figure 5.4: Representative nucleosome conformations during stretching. (a) relaxed starting conformation at $t = 0 \mu\text{s}$, (b) $t = 46.0 \mu\text{s}$, (c) $t = 83.5 \mu\text{s}$, (d) $t = 84.0 \mu\text{s}$, (e) $t = 84.3 \mu\text{s}$ and (f) $t = 100 \mu\text{s}$.

In the initial phase the histone core is reorientated and the linker DNA is aligned in direction of the stretching velocity \vec{v} (see Fig. (5.4b)). The DNA remained fully attached to the histone core and the adsorbed contour length is constant in the first section of the contour length-time diagram (5.5). From this time point we could identify three distinct steps, in which DNA is released:

- (a) The further pulling of the DNA ends results in a gradual detachment of the outer DNA turn from the histone core. In this step approximately 16 nm of

nucleosomal DNA are released, until the amount of adsorbed DNA levels off at a constant value.

- (b) In contrast, the inner DNA turn unwinds in a sudden event. In this step about $\approx 17 - 22$ nm of DNA are released. In order to reach the extended state the histone core has to rotate out of the plane, in which the DNA wraps around the histone core. The external force can then act to detach the DNA ends still bound to the histone core. This effect of rotating out-of-plane to reach the unwrapped state has been already postulated by Cui et al. [Cui and Bustamante, 2000]. The time scale associated with this process is in the range of μ s, which is significantly faster than the unwinding of the first DNA turn.
- (c) The DNA is not totally detached from the histone core as shown in Fig. (5.4f), but still leaving $\approx 11 - 14$ nm of DNA. Further application of force is needed to peel the remaining DNA from the histone core.

The released amount of DNA is directly related to the geometry of the nucleosome, which is defined by the radius of the DNA superhelix $R^{(n)}$, the pitch $p^{(n)}$ and the number of turns $N^{(n)}$. The first step (a) corresponds to the unwinding of $\lesssim 3/4$ turn of the DNA superhelix, which amounts to ≈ 20 nm for the assumed ideal geometry parameters. The remaining DNA turn of ≈ 26 nm stores the amount of DNA, which is released in the two subsequent steps (b)-(c).

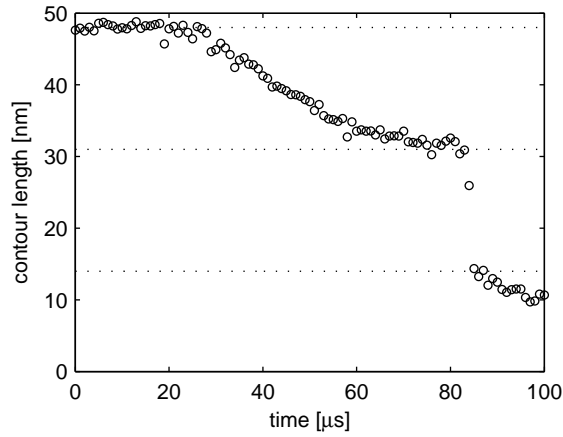


Figure 5.5: A representative time-dependent contour length curve of adsorbed DNA onto the histone core is shown ($\epsilon = 8 k_B T \text{ nm}^{-1}$). Pulling the DNA ends at a constant velocity $v = 0.1 \text{ cm s}^{-1}$ results in a gradual DNA release from the outer DNA turn of the nucleosome core particle. The inner DNA turn is released in a disruptive event on a timescale below μ s. The dashed lines indicate the mean equilibrium contour length (≈ 48 nm), mean contour length before disruption (≈ 31 nm) and mean contour length after disruption (≈ 14 nm).

5.2.2 Force-extension curves

A further step in the analysis was to measure force-extension curves for the unwrapping process. During the simulation the force F in direction \hat{x} of the stretching velocity \vec{v} or the external force \vec{F}^{ext} were calculated at the DNA end segments ($i = 0, N$). Simultaneously the extension x defined as the DNA end-to-end distance $(\vec{r}_N - \vec{r}_0) \cdot \hat{x}$ was recorded.

In order to obtain smooth force-extension curves, the forces were averaged over the extension within a bin width Δx . The bin width was chosen to adopt the value of the segment equilibrium length l_0 , such that a sufficient number $N^{(\text{meas})}$ of force measurements is assured within each bin. For example, at a constant stretching velocity v the mean dwell time for x to be found within Δx amounts to $\Delta x/v$, yielding the number of force measurements $N^{(\text{meas})} = f^{(\text{meas})} \Delta x/v$, where $f^{(\text{meas})}$ denotes the force measurement frequency. Even at the highest applied stretching velocity $v = 1 \text{ cm s}^{-1}$ the estimated number of force measurements remains $N^{(\text{meas})} > 40$, which guarantees good statistics.

According to the measurement and averaging protocol discussed in the preceding paragraph, force-extension curves have been obtained at defined stretching velocities and adsorption energy densities. The resulting force-extension curves are shown in Fig. (5.6) and Fig. (5.7). As considered before, the first part of the force-extension curve for extensions below $\approx 20 \text{ nm}$ is associated with the pulling of the free, nonadsorbed linker DNA. Subsequently, the force-extension curve exhibit two distinct regimes, a low-force regime, which is followed by a high-force regime at greater DNA end-to-end extensions.

- (a) In the low-force regime the measured force remains nearly constant. The regime can be identified with the unwrapping of the first DNA turn.
- (b) In the high-force regime the calculated force at the DNA ends increases linearly with the extension until the inner DNA turn unwraps abruptly. This single event is accompanied by a sudden drop in the calculated force. The local maximum of the force is referred to as the rupture force.
- (c) Beyond the force peak the forces increase linearly.

Low-force regime

From the first part of the force-extension curves in the force plateau, the mean force can be obtained. This quantity signifies the mean force, which is needed to detach the outer DNA turn from the histone core. Since the linker DNA length is about 25 nm , only extensions x in the range from $20 \text{ nm} \leq x < 40 \text{ nm}$, corresponding to detachment of the first DNA turn as confirmed by visual inspection of generated nucleosome conformations (see Fig. (5.4b)), have been considered in the calculation of the mean average unwrapping force. The upper limit is defined by the onset of the linear slope of the measured force and the full detachment of the first DNA turn as shown representatively in Fig. (5.4c).

We performed the analysis of BD trajectories with different initialized parameter sets.

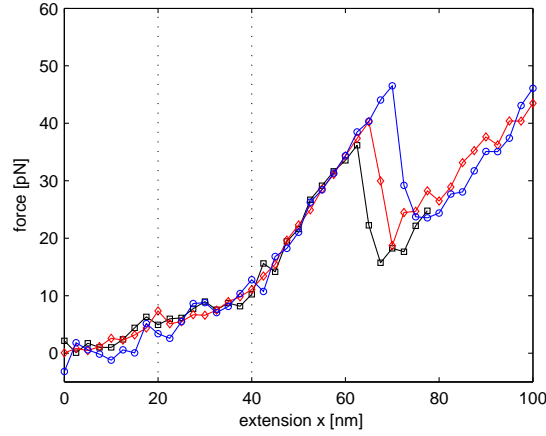


Figure 5.6: Representative force-extension curves were recorded during the stretching simulation. In this set of simulations the stretching velocities was varied between $v = 2.5 \times 10^{-3} \text{ cm s}^{-1}$ (*black squares*), $v = 1.0 \times 10^{-2} \text{ cm s}^{-1}$ (*red diamonds*) and $v = 1.0 \times 10^{-1} \text{ cm s}^{-1}$ (*blue circles*), while the adsorption energy density was held constant at $\epsilon = 8 k_B T \text{ nm}^{-1}$. Dashed lines indicate the different regimes: orientation of linker DNA and nucleosome, low-force regime and the onset of the high-force regime (*from left to right*).

Depending on the adsorption energy density the analysis yielded mean average unwrapping forces of 2.1 pN ($\epsilon = 6 k_B T \text{ nm}^{-1}$), 5.3 pN ($\epsilon = 7 k_B T \text{ nm}^{-1}$) and 7.3 pN ($\epsilon = 8 k_B T \text{ nm}^{-1}$).

High-force regime

As pointed out in section (2.2) single-molecule force spectroscopy involves the measurement of forces by sensing the displacements of a probe. For small deflections of the probe from its equilibrium position the force is linearly proportional to the displacement and acts as a spring with an elastic constant k_s . Furthermore, the probe must be coupled by a linker molecule to the system, which introduces an additional stiffness k_m . The effective spring constant is then given by the serial coupling of the two springs $1/k_{\text{eff}} = 1/k_m + 1/k_s$. In the simulation the DNA end segments are directly displaced, which would correspond to a very stiff elastic constant $k_s \gg 1$, therefore the effective spring constant is specified only by the linker DNA.

In the recorded force-extension curves the effective spring constant k_{eff} can be determined in the high-force regime, in which the force increases linearly with the extension. The effective spring constant $k_{\text{eff}} = dF/dx$ was extracted from the curves by a chi-square fit to the force-extension curves in the range from $x \geq 40 \text{ nm}$ up to the peak force attained at rupture. The average slope of the curves was identified with the effective spring constant. The effective spring constant was estimated to have a mean value of $k_{\text{eff}} \approx 1.2 \text{ pN nm}^{-1}$, which approximates reasonably well the linear force regime of all force-extension curves (with the standard deviation $\sigma_{k_{\text{eff}}} < 1 \text{ pN nm}^{-1}$).

The local maximal force at rupture or shortly the rupture force is a quantity, which implicitly contains information about the energy landscape along the transition pathway. In detail the dependence of the rupture force on the stretching velocity and adsorption energy density was studied. From the representative force-extension curves in Fig. (5.6) one can infer that the system responds to a slower stretching velocity of the DNA ends with a decreasing rupture force. The observed velocity dependence is in agreement with predictions of the DFS theory (see section (2.2)).

The analogue figure for the adsorption energy density parameter is shown in Fig. (5.7). The effect of a smaller adsorption energy density ϵ as a measure of the weakened interaction strength between DNA and the protein complex results in smaller values of observed rupture forces during stretching.

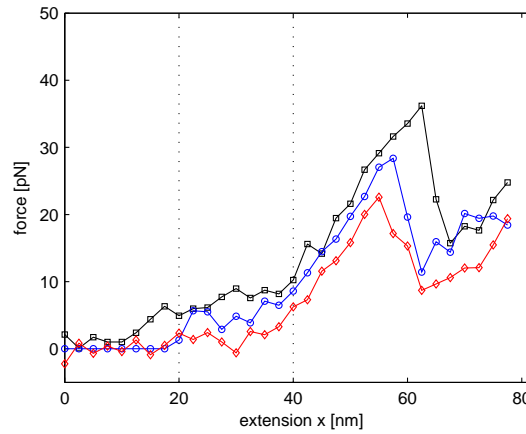


Figure 5.7: Representative force-extension curves have been recorded during the stretching simulation at different adsorption energy densities $\epsilon = 6 \text{ k}_B\text{T nm}^{-1}$ (*diamonds*), $\epsilon = 7 \text{ k}_B\text{T nm}^{-1}$ (*circles*), $\epsilon = 8 \text{ k}_B\text{T nm}^{-1}$ (*squares*). The stretching velocity was held constant at $v = 2.5 \times 10^{-3} \text{ cm s}^{-1}$.

5.3 Dynamic Force Spectroscopy

Dynamic Force spectroscopy allows to investigate rupture forces or force spectra and the analysis of those provides information about bond strength, lifetimes and energy landscapes along the transition pathway. Here the Dynamic Force Spectroscopy theory as presented in section (2.2) was applied to the simulated transition in the nucleosome system. The transition starts from a partially wrapped state as represented by Fig. (5.4c) and passes to a fully unwrapped state shown in Fig. (5.4f). Kinetic rate constants and energy barriers of the transition were extracted.

Phenomenological model

In a first step we analyzed the simulated rupture force spectra in the framework of the phenomenological model (see section (2.2.1)), which is a common way in DFS experiments [Brower-Toland et al., 2002, Pope et al., 2005] to obtain transition parameters. In DFS experiments the key parameter is the force loading rate r_f . In the high-force regime the force obeys Hooke's law and is a linear function of the extension $F = k_{\text{eff}}x$ with the determined effective spring constant as prefactor. The force loading rate is then simply proportional to the stretching velocity and all quantities can be expressed by the force loading rate:

$$r_f = \frac{dF}{dt} = k_{\text{eff}} \frac{dx}{dt} = k_{\text{eff}}v. \quad (5.2)$$

We proceeded by averaging for each parameter set the measured rupture forces, which yielded the mean rupture force $\langle F^{(s)} \rangle$. Further the variance of rupture force $\left(\sigma_F^{(s)}\right)^2$ was calculated. Here the quantities are indexed with an 's' to indicate that the data has been acquired in the simulation.

With the help of Eq. (2.30), which relates the mean rupture force $\langle F \rangle$ to the force loading rate r_f , the escape rate at zero external force k_{off} and the reaction distance d can be determined. Since the phenomenological model predicts a linear dependence of the mean rupture force on $\log(r_f)$, a linear function was fitted to the mean rupture force data on a logarithmic scale. The mean rupture forces together with the fitted functions are depicted in Fig. (5.8). The simulated rupture force data reflects the known connection between mean rupture force and force loading rate/stretching velocity as stated in the last section.

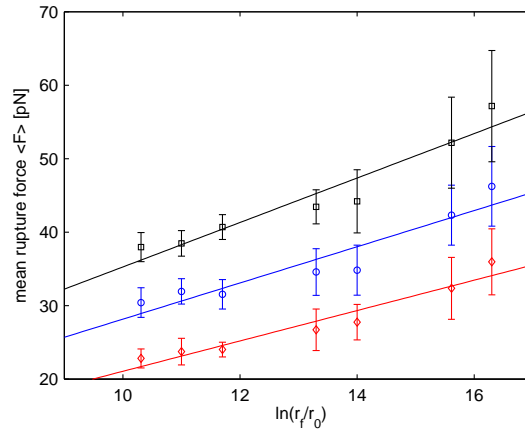


Figure 5.8: Rupture forces fitted with the phenomenological model. The fitting parameters are listed in Tab. 5.1

The fit parameters describing the nucleosome disruption kinetics k_{off} and energy landscape d are summarized in Tab. (5.1). The energy barrier E_b is not directly accessible

by the method, but can be deduced from an estimate of the intrinsic escape rate k_0 (see Eq. (2.24)). The intrinsic escape rate is dominated by the slowest process involved in the initial unwrapping of DNA from the nucleosome. In this case the time scale of the dominant process is of the order of the rotation of a nucleosome-sized sphere. In literature the following estimated values for the intrinsic escape rate are listed, e.g. $k_0 \approx 10^5 - 10^6 \text{ s}^{-1}$ taken from [Kulić and Schiessel, 2004] or $k_0 \approx 10^6 - 10^8 \text{ s}^{-1}$ [Pope et al., 2005]. Adopting the latter estimates in the calculations, the energy barriers were included in Tab. (5.1). In general, we found with the phenomenological model faster escape rates at zero external force $k_{\text{off}} \approx 10^{-1} - 10^{-2} \text{ s}^{-1}$ and lower energy barriers $E_b \approx 15 - 22 \text{ k}_B\text{T}$ as compared to experimentally found values.

	d [nm]	$k_{\text{off}} [\text{s}^{-1}]$	$E_b [\text{k}_B\text{T}]$		
$k_0 [\text{s}^{-1}]$			1.0×10^6	1.0×10^7	1.0×10^8
$\epsilon = 6 \text{ k}_B\text{T nm}^{-1}$	1.96	2.3×10^{-1}	15.3	17.6	19.9
$\epsilon = 7 \text{ k}_B\text{T nm}^{-1}$	1.64	5.5×10^{-1}	16.7	19.0	21.3
$\epsilon = 8 \text{ k}_B\text{T nm}^{-1}$	1.34	3.6×10^{-2}	17.2	19.5	21.8

Table 5.1: Transition parameters for the phenomenological model

The phenomenological model is in agreement with simulated mean rupture force within the standard deviations, but several inconsistencies remain with the measured simulation data.

- The phenomenological theory predicts that the variance of rupture force σ_F^2 is independent of the force loading rate r_f . But from Fig. (5.8) it is evident that the variance of force from the simulated data set is a non-constant function of the force loading rate.
- The mean rupture forces can be extrapolated according to the phenomenological model to slower force loading rates for which experimental DFS data is available. The resulting mean rupture forces are not consistent with the experimental mean rupture forces for the considered range of energy adsorption densities, as determined by equilibrium fluctuations.

An explanation for the discrepancy is that the phenomenological approach for the diffusive barrier crossing is strictly only valid in the range of small forces $F \ll F_c$ [Lin et al., 2007]. Here F_c denotes the critical force, as defined in section (2.2) at which the barrier to escape vanishes. At small forces or correspondingly small force loading rates the details of the underlying energy landscape of the potential are not important, as the escape dynamics is determined mainly from the reduction of the energy barrier. But at high forces the fluctuations of the energy minimum and transition state coordinate x_{\pm} under an increasing external force have to be explicitly taken into account. Since the equation $F_c = E_b/d$ defines the critical force, now the force range consistent with

the phenomenological model, can be specified. For the parameters defining the energy landscape listed in Tab. (5.1) and an assumed intrinsic escape rate $k_0 = 10^6 \text{ s}^{-1}$ the critical forces are approximately 36.4 pN ($\epsilon = 6 \text{ k}_\text{B} \text{ T nm}^{-1}$), 46.9 pN ($\epsilon = 7 \text{ k}_\text{B} \text{ T nm}^{-1}$) and 58.9 pN ($\epsilon = 8 \text{ k}_\text{B} \text{ T nm}^{-1}$). For the highest force loading rates the rupture forces (see Fig. (5.8)) are clearly in the strong pulling limit $1 - F/F_c \ll 1$, but the limit is valid in good approximation to the total range of simulated force loading rates accessible to computer simulations.

Based on the fact that the variance of the rupture force varied with the force loading rate, we conclude that the phenomenological model can not be applied, even if it describes the mean rupture force data reasonably well. Furthermore, the estimated parameters show that the measured rupture forces are close to the critical force. This indicates that the estimated parameters are not consistent with the assumption of weak pulling forces for the phenomenological model. A priori there exists no criterion to decide in which limit the simulations were carried out, but the results point at the conclusion that the force loading rate is within the strong pulling regime.

Model-dependent approach

In the strong pulling regime, close to the critical force $1 - F/F_c \ll 1$, alternative classes of analytical models exist, which assume explicitly a defined potential model disturbed in the presence of an applied force field. Therefore we also analyzed the simulation rupture force data with a method which has been proposed by Dudko [Dudko et al., 2003] and described in a general form in reference [Dudko et al., 2006]. It originates from Garg's formalism [Garg, 1995], which is summarized in detail in section (2.2.2).

In the approach taken by Dudko et al. the energy barrier E_b is an additional free parameter, besides the reaction distance d and escape rate at zero external force k_{off} , already present in the phenomenological model. The transition parameters (E_b, d, k_{off}) are identified with the set of parameters, which minimizes the deviations between the analytical solution and the simulation data. A similar procedure to analyze the pulling of a multimodule titin molecule was done in [Szabo and Hummer, 2003].

The deviation of the analytical solution for the mean rupture force Eq. (2.38) with a specified set of parameters from the simulation results can be quantified by the χ_F^2 function. χ_F^2 is defined as the sum

$$\chi_F^2 = \sum_{\{r_F\}} \frac{[\langle F^{(s)}(r_F) \rangle - \langle F^{(a)}(r_F) \rangle]^2}{[\sigma_F^{(s)}(r_F)]^2}, \quad (5.3)$$

where $\langle F^{(s)}(r_F) \rangle$ and $\langle F^{(a)}(r_F) \rangle$ are the simulated and analytical average rupture forces at the considered n force loading rates of the set $\{r_F\}$, respectively. The 'a'-index indicates the predictions of the analytical solution for the quantities, in order to differentiate it from the simulated values. In Eq. (5.3) the quadratic deviations between the

simulated and analytical mean rupture forces are weighted by the inverse of the variance of simulated rupture force $\left[\sigma_F^{(s)}\right]^2$, since the variance is non-uniform for different force-loading rates.

It has to be remarked that the model-dependent approach extends the number of parameters, as compared to the phenomenological model, by an additional free parameter. The parameter value space, where each point defines a possible set of parameters (E_b, d, k_{off}) , is therefore 3-dimensional. In order to make precise predictions about the transition parameters, we included the variance of rupture forces in the analysis. It allows to further narrow the parameter value space to a subspace of parameters consistent with the simulated data. Here we used the fact that the variance of rupture forces is a function of the force loading rate and contains additional information.

Analogously a quantity χ_σ^2 can be defined for the standard deviations of the mean rupture forces:

$$\chi_\sigma^2 = \sum_{\{r_F\}} \frac{[\sigma^{(s)}(r_F) - \sigma^{(a)}(r_F)]^2}{\sigma_\sigma^2}, \quad (5.4)$$

which is a measure for the deviations between the simulated and analytical variance of rupture forces. Here $\sigma^{(s)}(r_F)$ and $\sigma^{(a)}(r_F)$ denote the simulated and calculated standard deviations at the respective force loading rates. σ_σ is the assumed uniform statistical error of the standard deviation. Statistical errors of the standard deviations have been assumed to have a value of 15% relative error of the maximal standard deviation, e.g. at an adsorption energy density $\epsilon = 8 \text{ k}_B\text{T nm}^{-1}$ this corresponds to $\approx 1.1 \text{ pN}$.

The 3-dimensional parameter value space has been restricted by imposing the constraint $\text{RMSD} < 1$ for each point in the parameter value space. The root-mean-square deviation (RMSD) has been obtained by calculating the RMSD of the mean force $\text{RMSD}_F = \sqrt{\chi_F^2/n}$ and the RMSD of the standard deviation of the mean force $\text{RMSD}_\sigma = \sqrt{\chi_\sigma^2/n}$. The maximum of the two independently calculated root-mean-square deviations $\text{RMSD} = \max(\text{RMSD}_F, \text{RMSD}_\sigma)$ is used with the stated condition to find the parameter values, which are simultaneously consistent with the simulated mean rupture forces and standard deviations of the mean rupture force.

The root-mean-square deviation RMSD was evaluated at discrete points in the parameter value space $(E_b, d, \log_{10}(k_{\text{off}}))$. The discrete points in the parameter value space were positioned equidistantly on a grid. The separations between grid points $\Delta E_b = 0.05 \text{ k}_B\text{T}$, $\Delta d = 0.02 \text{ nm}$ and $\Delta \log_{10}(k_{\text{off}}) \approx -0.37$ in the direction of the energy barrier E_b -, reaction distance d - and escape rate k_{off} -axis respectively, were chosen sufficiently small to guarantee smooth transitions of the sampled RMSD function between adjacent grid points. In Fig. (5.9), (5.10), (5.11) the maximum range of parameters consistent with a given RMSD is determined as function of the adsorption energy density. Therefore the minimum RMSD was projected along one out of three axis onto planes of the two remaining parameters E_b , d and k_{off} . The cutoff for the RMSD was set according to the imposed constraint to unity.

For this choice e.g. in the case of an adsorption energy density $\epsilon = 8 \text{ k}_B\text{T nm}^{-1}$,

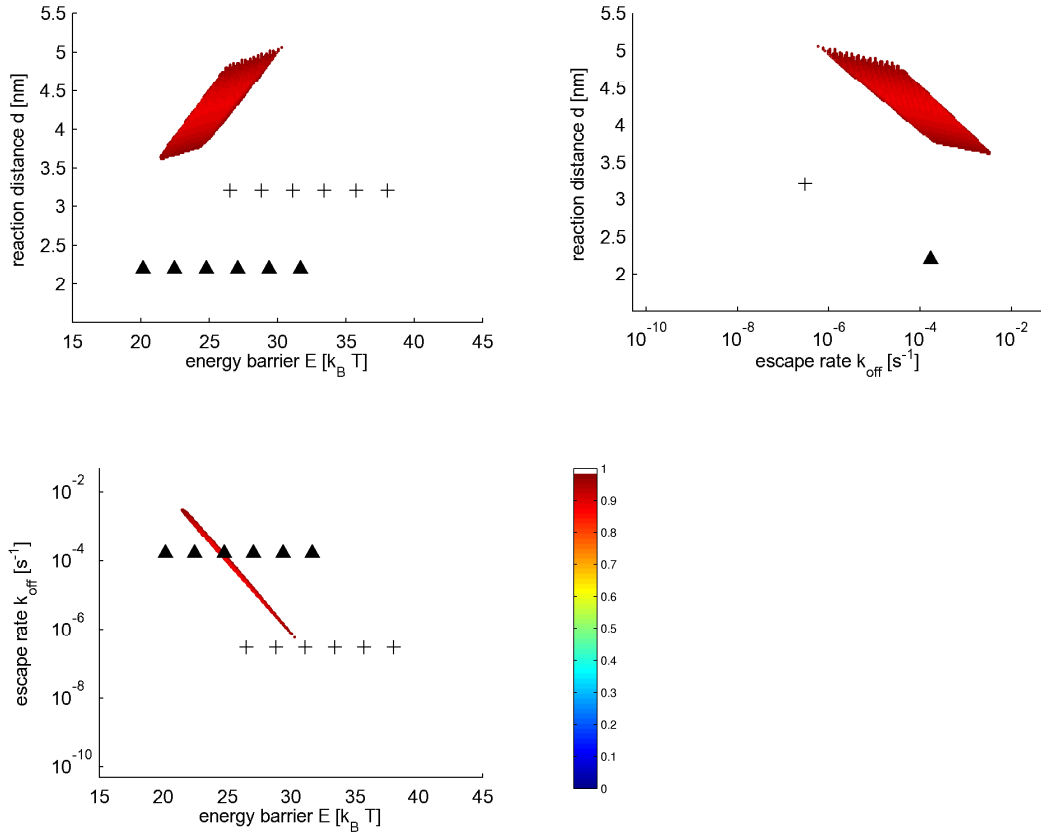


Figure 5.9: Shown are contour surfaces of RMSD calculated as the maximum of RMSD_F and RMSD_σ for the mean and standard deviation of rupture forces, respectively. In order to identify the bounds on the transition parameters E_b , d and k_{off} , the minimum RMSD was projected onto the (E_b-d) -, (E_b-k_{off}) - and $(k_{\text{off}}-d)$ -planes of the 3-dimensional parameter value space. The energy adsorption density was set to $\epsilon = 6 k_B T \text{nm}^{-1}$. Results from DFS experiments were included from [Brower-Toland et al., 2002] (*crosses*) and [Pope et al., 2005] (*diamonds*). The corresponding energy barriers have been calculated according to Eq. (2.24) for the set of intrinsic escape rates $k_0 \in \{10^5 \text{ s}^{-1}, 10^6 \text{ s}^{-1}, 10^7 \text{ s}^{-1}, 10^8 \text{ s}^{-1}, 10^9 \text{ s}^{-1}, 10^{10} \text{ s}^{-1}\}$.

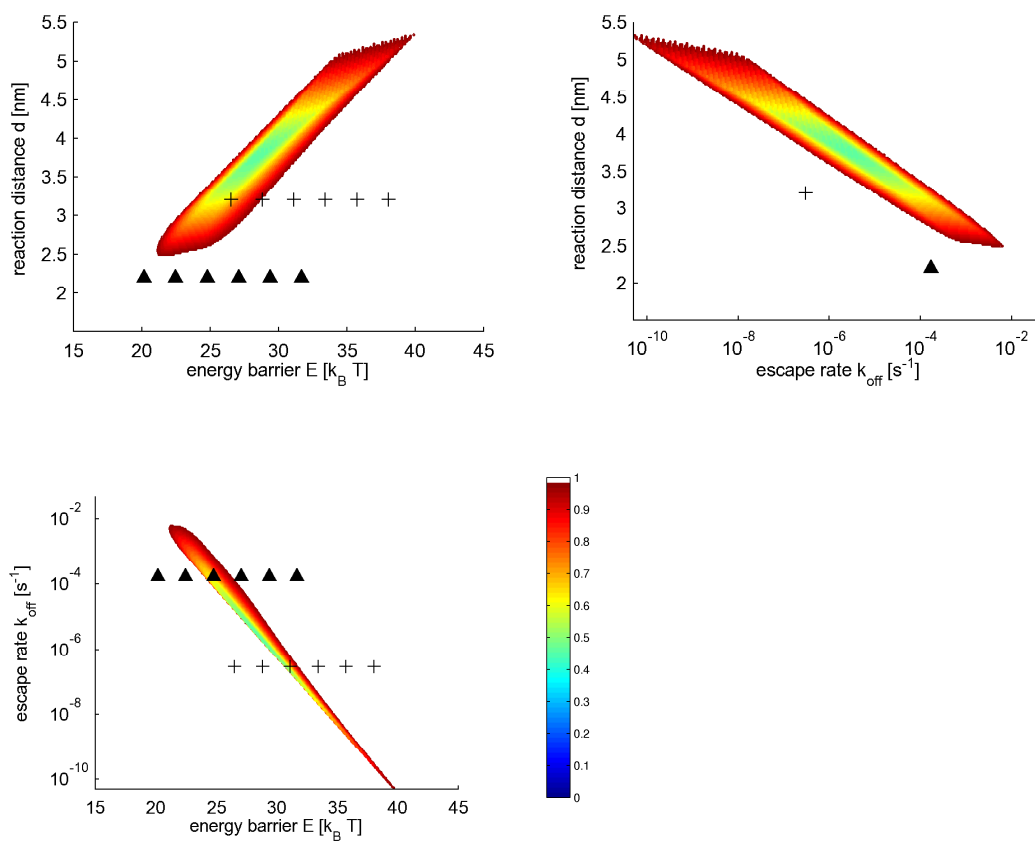


Figure 5.10: Contour surfaces of RMSD as described in Fig. (5.9), are shown. The energy adsorption density was set to $\epsilon = 7 k_B T \text{nm}^{-1}$.

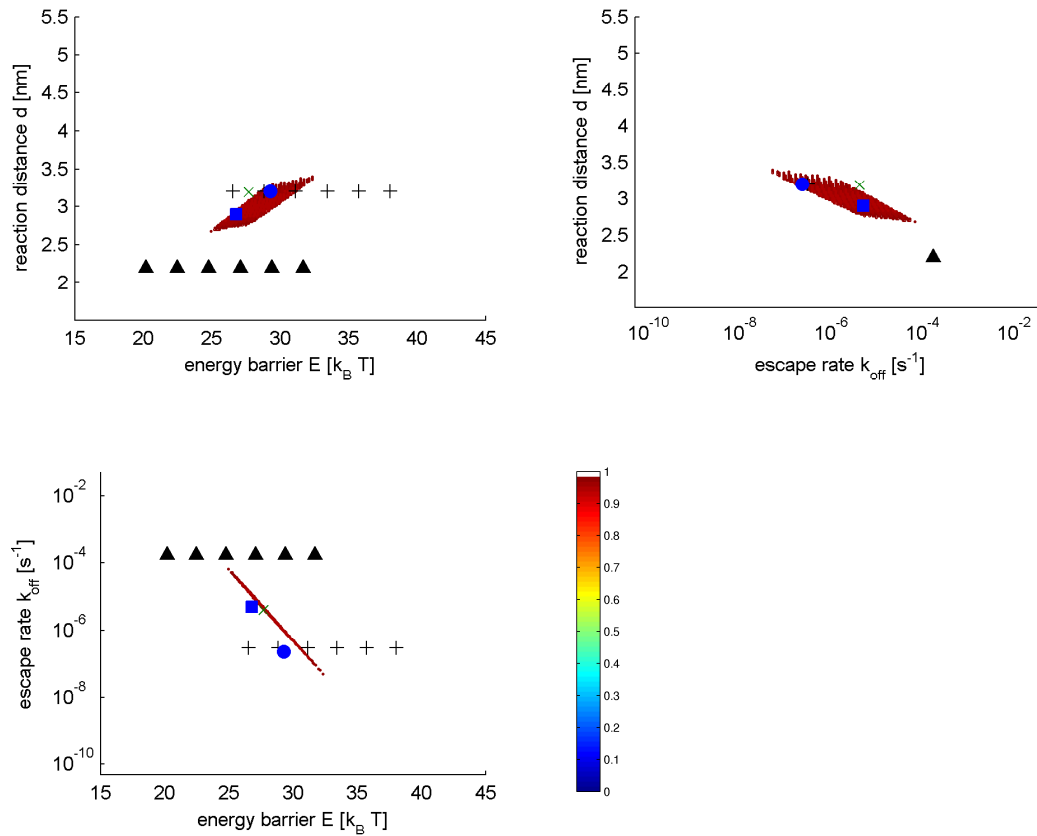


Figure 5.11: Contour surfaces of RMSD as described in Fig. (5.9), are shown. The energy adsorption density was set to $\epsilon = 8 k_B T \text{ nm}^{-1}$. In addition the transition parameters obtained by the rupture force distribution of single nucleosome (*green crosses*) and dinucleosome (first rupture (*blue circles*) and second rupture (*blue squares*)) stretching are included.

we estimated the parameters to be within the limits $24.9 \text{ k}_B\text{T} \leq E_b \leq 34.0 \text{ k}_B\text{T}$, $2.5 \text{ nm} \leq d \leq 3.5 \text{ nm}$ and $1.0 \times 10^{-4} \text{ s}^{-1} \leq k_{\text{off}} \leq 3.0 \times 10^{-8} \text{ s}^{-1}$. The transition parameters exhibited minimal deviations from the simulated data or a minimal RMSD for an energy barrier $E_b = 28.6 \text{ k}_B\text{T}$, a reaction distance $d = 3.02 \text{ nm}$ and an escape rate $k_{\text{off}} = 1.91 \times 10^{-6} \text{ s}^{-1}$. The optimal transition parameters are tabulated in Tab. (5.2).

	$E_b [\text{k}_B\text{T}]$	$d [\text{nm}]$	$k_{\text{off}} [\text{s}^{-1}]$
$\epsilon = 6 \text{ k}_B\text{T nm}^{-1}$	26.4	4.36	2.61×10^{-5}
$\epsilon = 7 \text{ k}_B\text{T nm}^{-1}$	28.4	3.76	2.91×10^{-6}
$\epsilon = 8 \text{ k}_B\text{T nm}^{-1}$	28.6	3.02	1.91×10^{-6}

Table 5.2: Transition parameters for the model-dependent approach

The projected RMSD (see Fig. (5.9), (5.10), (5.11)) revealed strong correlations between the three transition parameters of the model for all considered cases. The escape rate scales exponentially with the energy barrier as expected from Kramers theory, while the reaction distance scales linearly with the energy barrier.

Further one can infer from the series of Fig. (5.9), (5.10) and (5.11) a gradual shift of the parameter value space, which fulfills the constraint $\text{RMSD} < 1$. With increasing adsorption energy density the allowed parameter value space is displaced towards higher energy barriers and consequently slower escape rates, while simultaneously the reaction distances decrease.

The optimal values found for the transition parameters as tabulated in Tab. (5.2) has been used with the analytical Eq. (2.38) to calculate the mean rupture force curves. The analytical curves are shown together with the simulated mean rupture forces in Fig. (5.12a). Based on the same set of parameters, the variance of rupture forces according to Eq. (2.39) was calculated in Fig. (5.12b).

A check for the self-consistency of the model-dependent approach was done. Since the critical force is given in the model-dependent approach by $F_c = E_b/\nu d$, where $\nu = 2/3$, the resulting critical forces are 36.8 pN ($\epsilon = 6 \text{ k}_B\text{T nm}^{-1}$), 45.9 pN ($\epsilon = 7 \text{ k}_B\text{T nm}^{-1}$) and 57.5 pN ($\epsilon = 8 \text{ k}_B\text{T nm}^{-1}$). The measured rupture forces are therefore within the strong pulling regime $1 - F/F_c \ll 1$. As a consequence the results satisfy the basic assumption of strong pulling and the application of the model-dependent approach is valid. Beyond the critical force the mechanical limit is reached, and at that point the model-dependent approach breaks down.

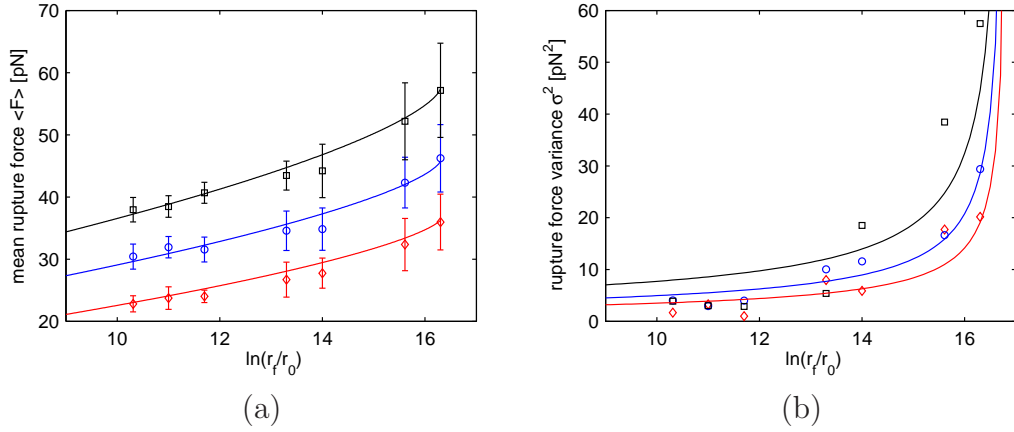


Figure 5.12: (a) Simulated mean rupture forces as a function of the force loading rate r_f are shown for adsorption energy densities $\epsilon = 6 \text{ k}_B\text{T nm}^{-1}$ (red diamonds), $\epsilon = 7 \text{ k}_B\text{T nm}^{-1}$ (blue circles) and $\epsilon = 8 \text{ k}_B\text{T nm}^{-1}$ (black squares). Analytical solutions of the mean rupture forces derived from the model-dependent approach with parameters according to Tab. (5.2) are indicated by lines. (b) Simulated variance of the mean rupture force (red diamonds, blue circles, black squares) and the analytical solution of the mean rupture force variance (lines) with the same parameters as in (a). $r_0 = 1 \text{ pN nm}^{-1}$ is an arbitrary scale on the force loading rate axis.

5.3.1 Rupture force distribution

So far in the analysis only the mean and the variance of the rupture force was used, but naturally the complete distribution of rupture forces contains further information about the studied system. By comparison with the simulation the analytical solution for the rupture force distribution $P_1(F)$ at a given force loading rate r_f serves as a further method to validate the results. In the model-dependent approach, described in section (2.2.2), the escape rate $k(F)$ reads [Dudko et al., 2006]

$$k(F) = k_{\text{off}} \left(1 - \frac{\nu F d}{E_b}\right)^{1/\nu-1} \exp \left[E_b \left(1 - \left(1 - \frac{\nu F d}{E_b}\right)^{1/\nu}\right) \right]. \quad (5.5)$$

The distribution of rupture forces at a given force loading rate r_f can then be obtained analytically with the help of Eq. (2.28)

$$P_1(F) = \frac{k(F)}{r_f} \exp \left(\frac{k_{\text{off}}}{dr_f} \right) \exp \left[- \left(\frac{k(F)}{dr_f} \right) \left(1 - \frac{\nu F d}{E_b}\right)^{1-1/\nu} \right], \quad (5.6)$$

which is valid according to [Dudko et al., 2006] for not too high force loading rates. From a set of $N_{\text{data}} = 105$ BD trajectories, the rupture forces in the force-extension curves have been identified, and subsequently a rupture force histogram was generated. The analytical rupture force distribution was matched with the simulated distribution by a simulated annealing MC method. The simulated annealing MC algorithm is based on Ref. ([Corana et al., 1987]) and was adapted from an implementation by J.Krieger.

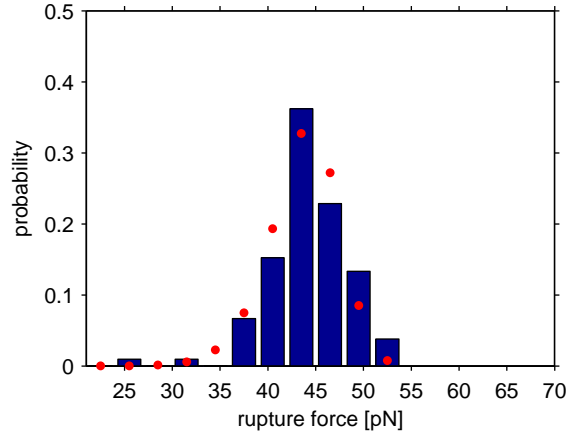


Figure 5.13: Probability distribution $P_1(F)$ of rupture forces is shown for a stretching velocity of 0.1 cm s^{-1} ($\epsilon = 8 \text{ k}_B\text{T nm}^{-1}$). The histograms have been generated from $N = 105$ simulated rupture events with a bin width $\Delta F = 3 \text{ pN}$. The fit (*circles*) to the rupture force distribution yields the parameters $E_b = 27.7 \text{ k}_B\text{T}$, $d = 3.19 \text{ nm}$, $k_{\text{off}} = 4.1 \times 10^{-6} \text{ s}^{-1}$

The simulated rupture force histogram together with the best analytical fit is shown in Fig. (5.13). The found transition parameters $E_b = 27.7 \text{ k}_B\text{T}$, $d = 3.19 \text{ nm}$ and $k_{\text{off}} = 4.1 \times 10^{-6} \text{ s}^{-1}$ are reasonably close to the parameters determined by the alternative method, which supports the applied parameter estimation protocol.

5.3.2 Links to DFS experiments

In this section the findings obtained by BD simulations are compared with available experimental data on nucleosome disruption. A stepwise release of DNA in three stages has likewise been observed in DFS studies [Pope et al., 2005, Brower-Toland et al., 2002]. Brower-Toland et al. used chromatin arrays with purified core histones on a 3684 bp DNA, containing 17 repeating units of the 5S rRNA nucleosome positioning element, which corresponds approximately to the DNA length in the presented single nucleosome stretching simulations. In agreement with the simulations at first the outer DNA turn was released gradually. In this step unwrapping forces beneath 15 pN were sufficient to release about 76 bp of DNA, consistent with the calculated mean forces in the low-force regime. The second stage of disruption involved the sudden release of the next 80 bp, while then still about 11 bp were bound to the histone core. From the BD trajectories we observed also (see Fig. (5.5)) the effect that DNA remained bound to the histone core in the last stage of stretching, as the bending energy of the attached DNA segments is exceeded by the energetic gain due to the DNA-histone core interaction. The general results are supported by [Pope et al., 2005], who reported on reconstituted chromatin fibers unwrapping events with discrete force peaks and step lengths of extension centered at 60 nm, which have been associated with the disruption of entire nucleosomes, and at 30 nm, corresponding to partial nucleosome disruption

events. The salt conditions of 150 mM NaCl were comparable to the settings in our simulations.

The rupture forces obtained by the BD simulation were checked against the experimental rupture forces in stretching experiments. This is achieved with the extrapolation of the analytical solution to slower force loading rates into the range of typical stretching experiments. The same transition parameters for the analytical mean rupture force solution of the model-dependent approach were taken as tabulated in Tab. (5.2). The extrapolated mean rupture forces as functions of the force loading rate and energy adsorption density together with the experimental data are shown in Fig. (5.14).

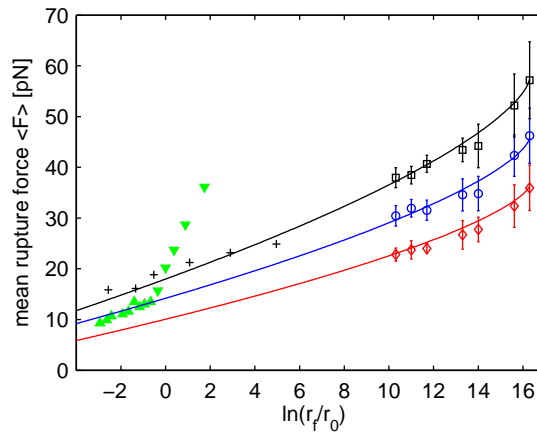


Figure 5.14: Extrapolation of the analytical solution to intermediate force loading rates for $\epsilon = 6 \text{ k}_B\text{T nm}^{-1}$ (*diamonds*), $\epsilon = 7 \text{ k}_B\text{T nm}^{-1}$ (*circles*), $\epsilon = 8 \text{ k}_B\text{T nm}^{-1}$ (*squares*). Experimental data taken from [Pope et al., 2005] show the most probable rupture forces F^* (for low-force (*triangles up*) and high-force loading rate (*triangles down*) distributions) and from [Brower-Toland et al., 2002] (*crosses*) is included in the figure.

Pope et al. [Pope et al., 2005] studied the chromatin fiber at different force loading rates and identified three different rupture force distributions with individual energy barriers and escape rates. A high-force population has been related to the presence of a linker histone B4, while the remaining two rupture force distributions with no linker histone occur at a low and a high force loading rate, respectively. Brower-Toland et al. used a more well defined system without the presence of linker histone-like proteins B4, HMG1, HMG2 and other non-histone chromatin-associated proteins, which resulted in a single rupture force population.

Experimental DFS data is available only for the most probable force. Due to the asymmetry of the rupture force distribution, the most probable force F^* is related to the mean rupture force $\langle F \rangle$ by a constant term $k_B T \gamma / d$ according to Eq. (2.31) in the slow pulling regime. We note that rigorously the experimental data must be shifted to be compared to the mean rupture force, but for the experimental conditions in [Brower-Toland et al., 2002, Pope et al., 2005] the shift does not exceed $\approx 1 \text{ pN}$ and allows

therefore direct comparison.

We found that the analytical mean rupture force solution at $\epsilon \approx 7 - 8 k_B T \text{ nm}^{-1}$ displays the best approximation to the experimental DFS studies. In detail, the rupture force population measured by Brower-Toland can be represented by the ($\epsilon = 8 k_B T \text{ nm}^{-1}$)-curve. For the second experimental data set, only the low-force loading rate distribution is explained by the presented nucleosome model. The expectation is that the low-force loading rate distribution represents the unperturbed natural system at best. We can speculate that the high-force loading rate distribution is obtained by selection of a different reaction pathway during the unwrapping transition, which would signify an altered energy landscape as defined by energy barrier and reaction distance along the new pathway. Possible alternative reaction pathways could be the release of a H2A-H2B dimer and formation of a subnucleosomal particle in the unwrapping process, which might be induced at high forces or in the case that the histone protein complex is non-equilibrated due to finite relaxation times at the relative higher force loading rates. The initial loss of a H2A-H2B dimer in the first stage for nucleosome disruption was proposed as an alternative model in the same DFS study [Pope et al., 2005] and is supported by atomic force microscopy data of subnucleosomal particles with stable wrapping of $\approx 25 \text{ nm}$, and $\approx 50 \text{ nm}$ corresponding to a complete nucleosomal particle [Nikova et al., 2004].

According to Ref. [Dudko et al., 2003], internal degrees of freedom e.g. as in this case the release of a H2A-H2B dimer during the unwrapping process, can explain for multiple rupture force distributions and have been also observed in experiments [Liphardt et al., 2001]. We remark that the presented analytical models are based on the assumption that unwrapping occurs along a single 1-dimensional path, but complex molecules may have a distribution of conformational states, which depend on the applied force. But naturally the internal degrees of freedom can not be described within the presented simulation model.

Based on the first experimental data set by Brower-Toland et al., the phenomenological model yields a reaction distance $d = 3.2 \text{ nm}$ and an escape rate $k_{\text{off}} = 3 \times 10^{-7} \text{ s}^{-1}$. In contrast, the low force loading rate population in the second data set by [Pope et al., 2005] was characterized by a lower reaction distance $d = 2.2 \text{ nm}$ and a faster kinetic rate $k_{\text{off}} = 1.7 \times 10^{-4} \text{ s}^{-1}$. The energy barrier follows then from the formula for thermally activated escape from a potential given by Eq. (2.24). In order to allow for comparisons, we considered a range of intrinsic escape rates k_0 from 10^5 s^{-1} to 10^{10} s^{-1} . The experimental data points from the first study were found to be within the determined bounds for the transition parameters, if the adsorption energy density was set to $\epsilon = 8 k_B T \text{ nm}^{-1}$ (see Fig. (5.11)). At the same time the intrinsic escape rate lay in the interval $k_0 \in [10^6 \text{ s}^{-1}, 10^7 \text{ s}^{-1}]$, which corresponds well to the upper bound set by the slowest process, the rotational motion of the histone core complex. For the second experimental DFS study the measured transition parameters were in proximity to the found parameter value space in Fig. (5.10) and Fig. (5.11), if an adsorption energy density of $\epsilon \approx 7 - 8 k_B T \text{ nm}^{-1}$ is assumed.

Interestingly, the found energy adsorption densities $7 - 8 \text{ k}_B\text{T nm}^{-1}$ for DFS experiments are slightly higher compared to $6 - 7 \text{ k}_B\text{T nm}^{-1}$ as indicated by the equilibrium DNA fluctuations. Since DFS experiments probe prominently DNA-protein interactions deep inside the nucleosome, this might indicate in reality weaker interactions between the histone proteins and the outer DNA turn, and a stronger affinity near the nucleosome dyad axis. Crystallographic data also supports relative stronger binding in proximity of the dyad axis (superhelical locations $\text{SHL} \pm 0.5, \pm 3.5$) [Davey et al., 2002, Luger and Richmond, 1998].

For the sake of completeness we note further DFS studies. In Ref. [Brower-Toland et al., 2005] the contributions of histone tails and acetylation has been investigated using mechanical disruption similar to the preceding study with intact nucleosomes [Brower-Toland et al., 2002]. The general effect of acetylation and histone tail removal was first a reduction of wrapped DNA length and second a decrease of the rupture force, e.g. $\approx 3 \text{ pN}$ if all histone tails were removed. Since acetylation/histone tail removal changes the overall charge state of the nucleosome, this relates in terms of the nucleosome model to simulations at a lower adsorption energy density.

A further study used periodic arrays of nucleosomes assembled on heterogeneous, non-repetitive DNA with the help of histone chaperone and ATP-dependent chromatin assembly and remodeling factors (ACF) [Gemmen et al., 2005]. They reported a much broader distribution of rupture forces ($F \approx 5 - 65 \text{ pN}$), than compared to the more regular 5S rRNA positioning sequence of [Brower-Toland et al., 2002].

The adsorption energy density in the histone octamer model represents only the upper bound on the interaction strength, while on average the effective adsorption energy density $\epsilon^{(\text{eff})}$ due to fluctuations from the ground state is much lower. Calculations at equilibrium as performed in section (5.1) for an energy adsorption energy $\epsilon = 8 \text{ k}_B\text{T nm}^{-1}$ yield a reduced effective adsorption energy density of $6.3 \text{ k}_B\text{T nm}^{-1}$. The effective adsorption energy density is defined as the average of the total DNA-histone core interaction energy $E^{(n)}$ per contour length of all interacting DNA segments. DNA is a semiflexible polymer, which is characterized by a large persistence length of 50 nm , and at the same time must be wound around a cylinder with radius 4.18 nm . Consequently the bending requires a relative huge amount of energy, which amounts to a bending energy density of $1.2 \text{ k}_B\text{T nm}^{-1}$, defined in an analog way to $\epsilon^{(\text{eff})}$. Also the Coulomb repulsion between two adjacent DNA strands on different windings in the nucleosome adds a major contribution in energy. The simulation yields a mean value of $\approx 77 \text{ k}_B\text{T}$ for the electrostatic energy, which is effective if both turns are wound around the histone core. Both terms reduce further significantly the effective adsorption energy, such that the net binding energy $\epsilon^{(\text{net})}$ (see section (5.1)) is much lower. An important quantity regarding the nucleosome stability is the binding energy. The binding energy represents the difference in the total energy between the DNA-histone core complex and the dissociated state of DNA and histone core. At $\epsilon = 8 \text{ k}_B\text{T nm}^{-1}$ the binding energy amounts to $\approx -189 \text{ k}_B\text{T}$, while the values for different interaction strengths can be found in Tab. (5.3).

ϵ [k _B T nm ⁻¹]	$\epsilon^{(\text{eff})}$ [k _B T nm ⁻¹]	ΔE [k _B T]
6	5.2	-141
7	5.8	-168
8	6.3	-189

Table 5.3: Effective adsorption energy density $\epsilon^{(\text{eff})}$ and total binding energy ΔE .

In Ref. [Brower-Toland et al., 2002] it was postulated that chemical interaction sites, presumed to be near the DNA positions +35 bp to +45 bp from the nucleosome dyad axis (or SHL = ± 3.5), are necessary to explain for the high rupture forces. In contrast, in the presented nucleosome model the DNA-protein interaction is non-localized, but uniformly distributed. Further it was only assumed that the interaction potential follows a superhelix along the surface of a toroid, as implied by crystallographic data. We showed that the assumed toroidal geometry is sufficient to reproduce the characteristic force-extension curves without invoking specific, localized interactions.

The appearance of an energy barrier, which stabilizes the inner DNA turn from unwrapping can be understood with the following considerations. According to Kulić et al. [Kulić and Schiessel, 2004] the interplay of the net adsorption energy, which takes into account the bending and electrostatic energy of DNA attached to the histone core, the bending energy of the free DNA arms and the gain in potential energy by pulling out the DNA ends against an external force, is sufficient to explain the origin of the energy barrier. In the analytical model from Kulić et al. a superhelical DNA path inside the nucleosome is assumed, which is comparable to the model used in this work. The resulting energy terms describe the competition of adsorption and applied external force as well as a geometric term accounting for loss and gain of potential energy due to variation of free DNA linker length. The varying length of free DNA arms results simply from desorption of DNA from the histone octamer and also from rotation of the nucleosome complex. The last term is due to the bending stiffness of the free DNA arms.

5.3.3 Complete dynamic force spectrum

The experimental data on nucleosome disruption is available only at relative slow force loading rates, while computational time restricts BD simulation to fast force loading rates. Therefore an important question to answer is whether the extrapolation of the analytical solution over several magnitudes of order is justified. Recently Lin et al. demonstrated that the phenomenological model and the model-dependent approach are valid at slow and fast force loading rates, respectively [Lin et al., 2007]. Further both models represent limiting cases of more general expressions in an unified model [Friddle, 2008]. The generalized expression for the mean rupture force reads

$$\langle F \rangle = F_c \left(1 - \left(1 - \frac{k_B T}{E_b} \exp \left(\frac{k_{\text{off}} k_B T}{r_F d} \right) E_1 \left(\frac{k_{\text{off}} k_B T}{r_F d} \right) \right)^{\frac{2}{3}} \right) \quad (5.7)$$

and the rupture force variance is given by

$$\sigma_f^2 = \left[\frac{k_B T}{d \left(1 + \frac{k_{\text{off}} k_B T}{r_f d} \right)} \right]^2 \left[1 - \frac{k_B T}{E_b} \exp \left(\frac{k_{\text{off}} k_B T}{r_f d} \right) E_1 \left(\frac{k_{\text{off}} k_B T}{r_f d} \right) \right]^{-\frac{2}{3}}. \quad (5.8)$$

In Fig. (5.15) we compared the analytical solutions of the mean rupture force and the rupture force variance for the model-dependent approach and the unified model in the complete force spectrum. Fig. (5.15a) verifies that the extrapolated solution of the model-dependent approach follows the unified model down to force loading rates as slow as $5 \times 10^{-4} \text{ pN s}^{-1}$, which encompasses the range of experimental force loading rates. Eq. (5.8) is asymptotically correct at high and low force loading rates, but underestimates the variance in-between as stated by Friddle, and also relative to the model-dependent approximation. We thus conclude that the analytical solution at high force loading rates found by the model-dependent approach remains valid for the rupture force spectrum ranging from high-force loading rates to slower force loading rates accessible in DFS experiments.

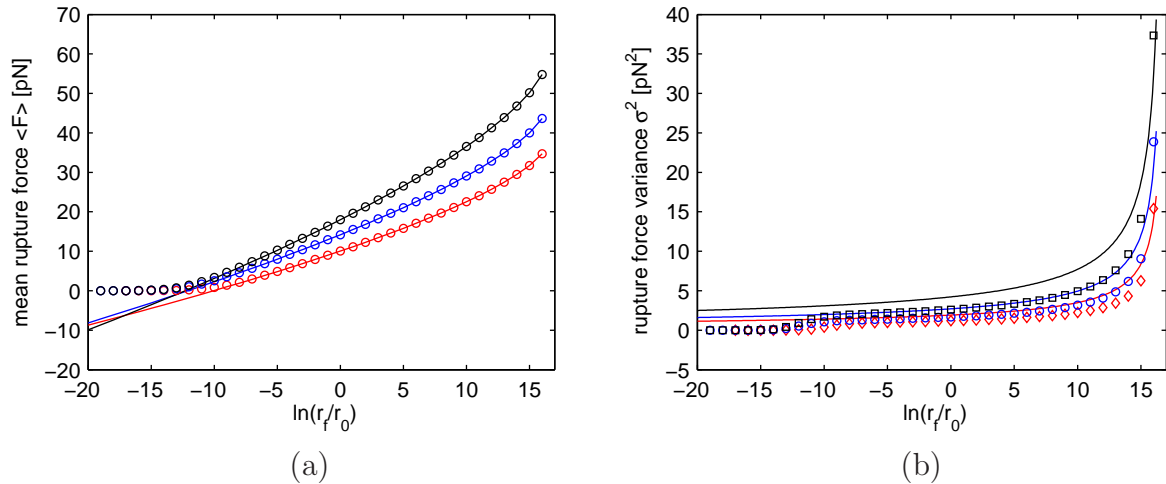


Figure 5.15: (a) The mean rupture force according to Eq. (5.7) (*symbols*) and (b) the rupture force variance as given by Eq. (5.8) were compared to the model-dependent approach (*lines*). The transition parameters listed in Tab. (5.2) were used for $\epsilon = 6 \text{ k}_B\text{T nm}^{-1}$ (*red diamonds*), $\epsilon = 7 \text{ k}_B\text{T nm}^{-1}$ (*blue circles*) and $\epsilon = 8 \text{ k}_B\text{T nm}^{-1}$ (*black squares*).

5.3.4 Effect of DNA charge renormalization

In the simulation electrostatics is treated on the level of the Debye-Hückel potential, which is the linearized solution of the full non-linear Poisson-Boltzmann equation. Nevertheless, as described in section (3.1.2) non-linear effects as counterion condensation can be incorporated into the Debye-Hückel theory by using the charge renormalization approximation. For highly charged objects, e.g. DNA, the electrostatic attraction of

counterions outweighs readily the entropic factors. Therefore as postulated by Manning the counterions may condense onto the charged object, renormalizing the effective charge density. For DNA, the theory predicts that counterions compensate about 75 % of the bare DNA charge. But in real systems the assumptions underlying the theory may not be fulfilled. The renormalized charge is strictly only valid in the limit of vanishing salt, while counterion condensation is highly suppressed at elevated salt. Further due to the finite size, end effects become important, which shift the balance towards counterion decondensation. At last in the nucleosome, the positively charged histone core complex drives away the condensed counterions from the DNA.

Therefore we regard the renormalized charge density only as a lower bound on the effective charge density, while the in the preceding sections employed bare DNA charge represents the upper bound. The two limits for charge density define the range for the effective DNA charge in real systems and are used to identify the maximal effect of charge renormalization on the unwrapping transition.

The effect of DNA charge renormalization was studied with BD simulations at equilibrium conditions regarding the adsorbed DNA length fluctuations and at non-equilibrium in stretching experiments. For this the adsorption energy density was held constant at $\epsilon = 6 \text{ k}_\text{B}\text{T nm}^{-1}$, while the linear charge density was set to the two limiting cases.

Concerning the first part we observed that the weaker Coulomb repulsion between the DNA strands on different turns increased the mean adsorbed contour length of DNA to 48.9 nm relative to 44.9 nm for the bare DNA charge. Spontaneous DNA fluctuations were greatly inhibited, which resulted in a sharp probability distribution function around the peak value (see Fig. (5.16a)). Analog to the calculations for the nucleosome systems with bare DNA charge, we estimated the equilibrium constant K_eq as shown in Fig. (5.16b). In respect of the net adsorption densities, the fits of simulated equilibrium constants to Eq. (5.1) yielded a significantly higher net adsorption energy density $\epsilon^{(\text{net})} \approx 3.1 \text{ k}_\text{B}\text{T nm}^{-1}$; a numerical value closer to the adopted total adsorption energy density.

In the second part the effect of charge renormalization was also studied in simulated DFS experiments. The effect can be deduced by the comparison of typical force-extension curves for bare and renormalized DNA charge (see Fig. (5.17a)). Here the mean average force needed to unwrap the outer DNA turn from the histone core is for renormalized DNA charge greatly increased with respect to the bare DNA charge, amounting to 9.6 pN as compared to 2.1 pN. We conclude that a major driving force for the unwrapping of the first turn is the electrostatic repulsion between the two adjacent DNA strands.

In a next step the rupture forces in the high force regime have been analyzed. We estimated from the linear slope of the force-extension curves an effective spring constant $k_\text{eff} \approx 1 \text{ pN nm}^{-1}$. The functional relation between mean rupture force and force loading rate is shown in Fig. (5.17b).

Analog to previous calculations the optimal values (see Tab. (5.4)) and bounds for the

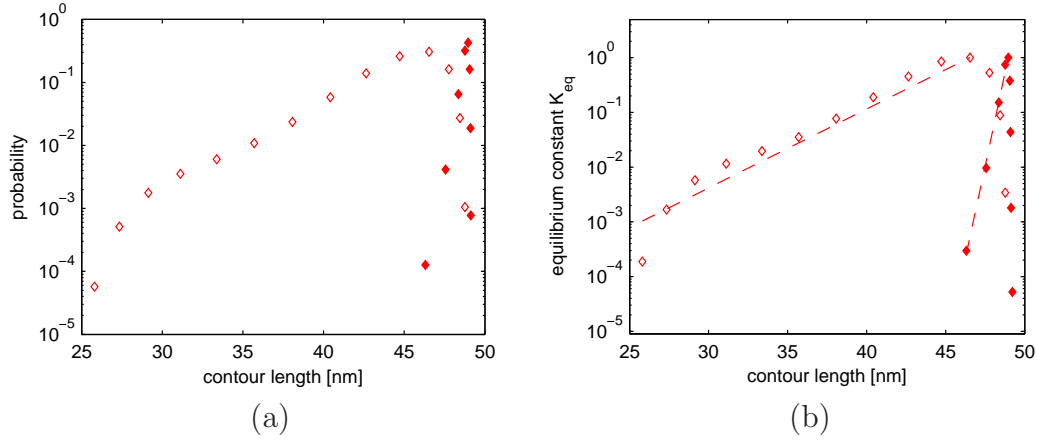


Figure 5.16: Probability distribution of contour length adsorbed to the histone core ($\epsilon = 6 k_B T \text{ nm}^{-1}$) for bare (*blank diamonds*) and renormalized DNA charge (*filled diamonds*).

transition parameters (see Fig. (5.18)) were determined.

It was found that for bare DNA charge the Coulombic repulsion between the two DNA strands also reduces the rupture forces significantly in comparison to renormalized DNA charge, which is expected foremost to be relevant for the unwrapping of the outer DNA turn. This indicates that in vicinity of the transition state, e.g. as shown in Fig. (5.4c,d)), where only at one point the two DNA strands face each other, the electrostatic repulsion facilitates the transition.

	$E_b [k_B T]$	$d [\text{nm}]$	$k_{\text{off}} [\text{s}^{-1}]$
bare DNA charge	26.4	4.36	2.61×10^{-5}
renormalized DNA charge	26.8	2.72	9.48×10^{-6}

Table 5.4: Comparison of transition parameters between renormalized and bare DNA charge for the model-dependent approach ($\epsilon = 6 k_B T \text{ nm}^{-1}$).

5.4 Oligonucleosomes

DNA in the cell nucleus is organized in a chromatin fiber, which is built up of individual nucleosomes as repetitive element. The structure of the chromatin fiber is regulated by internucleosomal, but it is to date not fully understood. Experimentally nucleosome disruption was studied mostly in oligonucleosomes [Cui and Bustamante, 2000, Brower-Toland et al., 2002]. In the present work the single nucleosome model was extended to provide a framework for the simulations of oligonucleosomes. Nucleosome-nucleosome interactions were incorporated on the level of a modified Gay-Berne potential (see section (3.9.1)). Preliminary results of oligonucleosome structures and dinucleosome

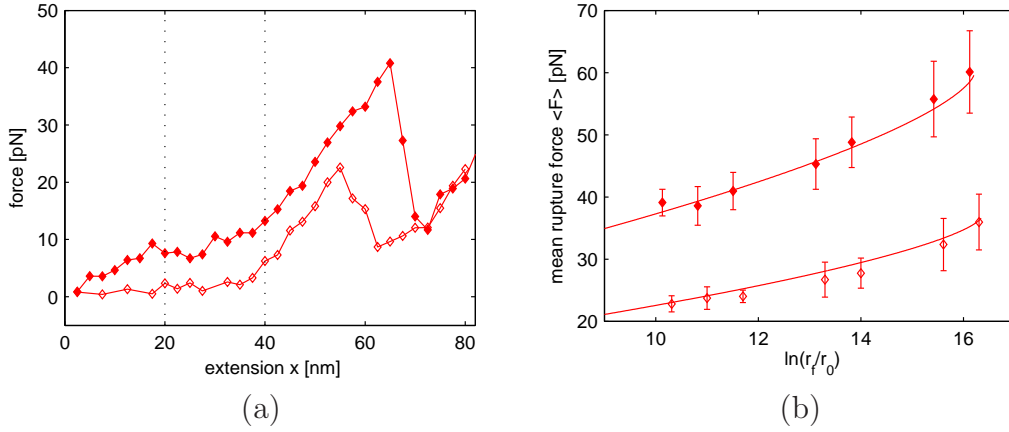


Figure 5.17: (a) Representative force-extension curves were recorded during the stretching simulation for bare (*blank diamonds*) and renormalized DNA charge (*filled diamonds*). The stretching velocity was held constant at $v = 2.5 \times 10^{-3} \text{ cm s}^{-1}$ ($\epsilon = 6 k_B T \text{ nm}^{-1}$). (b) Simulated mean rupture forces for renormalized and bare DNA charge. The analytical solutions (*lines*) of the model-dependent approach are shown. The respective parameters are listed in Tab. (5.4).

stretching experiments are shown.

In the initialization phase the histone cores were positioned equidistantly along the DNA fragment. During simulation the histone cores slide and show preference for a positioning at the DNA ends. A representative conformation of a 180 nm-DNA fragment containing two nucleosomes is shown in Fig. (5.19). The same effect was demonstrated in simulations and observed by AFM [Sakaue and Yoshikawa, 2001].

In order to relate the stretching velocity to the force loading rate an effective spring constant $k_{\text{eff}} \approx 0.5 \text{ pN nm}^{-1}$ was estimated from the force-extension curves.

In the following we show the reconstruction of single nucleosome kinetic rates and energy surface parameters from simulated pulling experiments of oligonucleosomes. Here the stretching of a dinucleosome was considered, but arrays containing multiple nucleosomes could be also analyzed accordingly in this way.

In a dinucleosome the probability distributions of rupture forces for the occurrence of the first and second rupture are related to the probability distribution $P_1(F) = -dS_1/dF$ and to the survival probability $S_1(F)$ of a single nucleosome, as defined in section (2.2) and (5.3.1). The survival probability for a dinucleosome for the case that no rupture has occurred yet, is given by $S_2^a = S_1^2$. The underlying assumption is that the individual nucleosomes disrupt independently and non-cooperatively. The assumption of an independent nucleosome disruption in nucleosome arrays is often assumed in the analysis of stretching experiments [Brower-Toland et al., 2002, Pope et al., 2005]. Therefore the combined survival probability of the dinucleosome can be

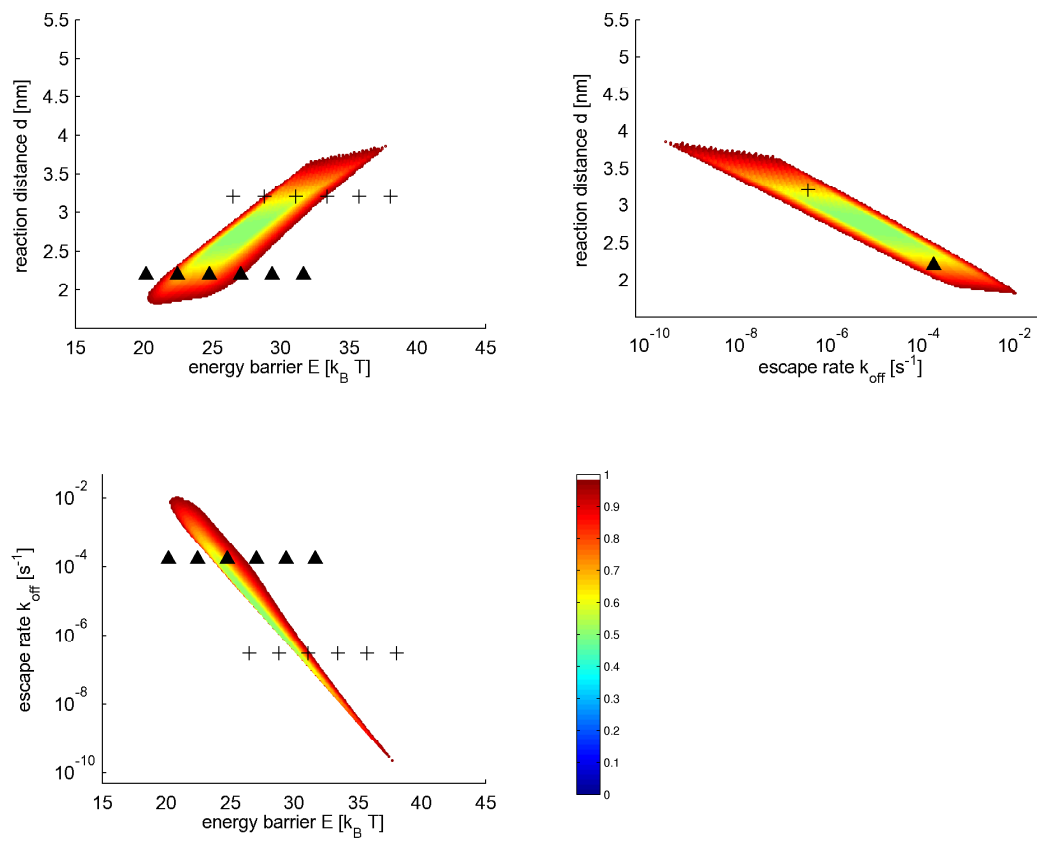


Figure 5.18: Contour surfaces of RMSD, described in Fig. (5.9), are shown for renormalized DNA charge ($\epsilon = 6 k_B T \text{ nm}^{-1}$).

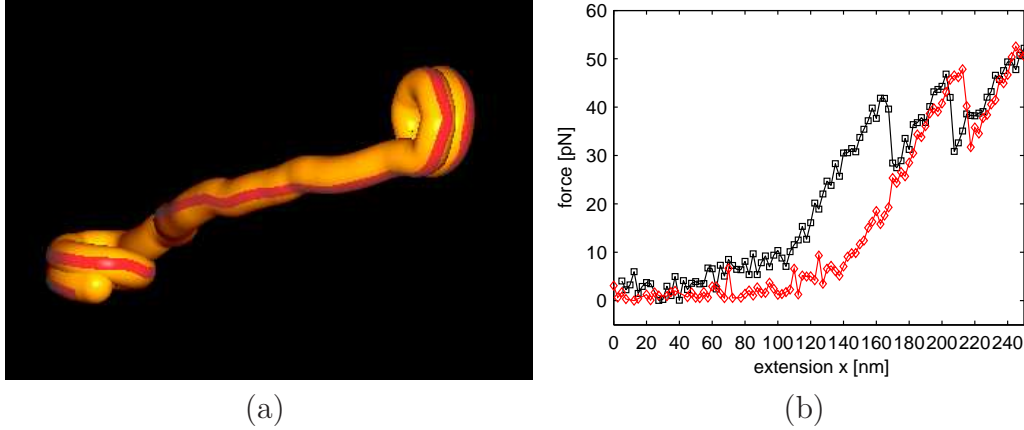


Figure 5.19: (a) The relaxed conformation of a dinucleosome is shown. (b) Force-extension curves of mononucleosome (*red diamonds*) and dinucleosome (*black squares*) at a stretching velocity $v = 0.1 \text{ cm s}^{-1}$ ($\epsilon = 8 \text{ k}_B\text{T nm}^{-1}$).

written as a product of the single survival probabilities. Then the following expression describes the rupture force distribution of the first rupture

$$P_2^a(F) = 2P_1(F) S_1(F). \quad (5.9)$$

The analog survival probability for a dinucleosome for the case that exactly one nucleosome is disrupted, is given by $S_2^b = 2S_1(1 - S_1)$. Hence the rupture force distribution for the second rupture reads

$$P_2^b(F) = 2P_1(F)(1 - S_1(F)). \quad (5.10)$$

We generated from force-extension curves histograms of rupture forces for the first and for the second nucleosome disruption (see Fig. (5.20)). The simulated annealing MC algorithm found optimal transition parameters by fitting the histogram data to the respective rupture force distributions P_2^a and P_2^b . Best estimates of the transition parameters are ($E_b = 29.3 \text{ k}_B\text{T}$, $d = 3.2 \text{ nm}$, $k_{\text{off}} = 2.3 \times 10^{-7} \text{ s}^{-1}$) for first rupture and ($E_b = 26.8 \text{ k}_B\text{T}$, $d = 2.9 \text{ nm}$, $k_{\text{off}} = 5.0 \times 10^{-6} \text{ s}^{-1}$) for the second rupture, which is in good agreement with transition parameters reconstructed from single nucleosome stretching simulations (see Fig. (5.11)). A further consequence is that at least for the chosen low nucleosome-nucleosome interaction strength, the individual nucleosome disrupt independently.

A first and initial step towards the chromatin fiber was done by studying a system containing three nucleosomes on a 200 nm-DNA fragment. The trinucleosome represents the smallest system of the chromatin fiber for which internucleosomal interactions gain importance, and therefore provides insight into the higher-order organization of the chromatin fiber. Here the system was investigated for bare and renormalized DNA charge with respect to compaction. Representative conformations are shown in

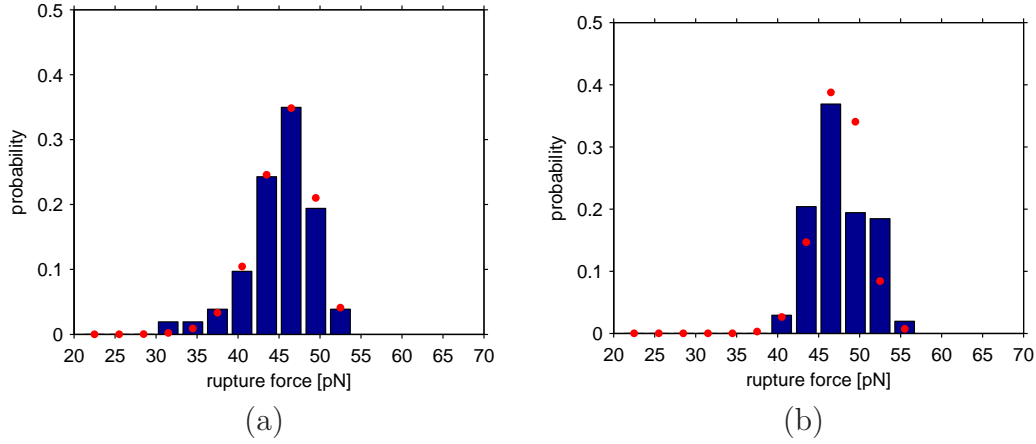


Figure 5.20: Rupture force distributions of a dinucleosome with bare DNA charge. The generated histograms show the rupture force distribution for (a) the first and (b) second nucleosome disruption at a stretching velocity $v = 0.1 \text{ cm s}^{-1}$ ($\epsilon = 8 \text{ k}_B\text{T nm}^{-1}$). A fit to the rupture force distributions given by Eq. (5.9) and Eq. (5.10) yielded the transition parameters (a) ($E_b = 29.3 \text{ k}_B\text{T}$, $d = 3.2 \text{ nm}$, $k_{\text{off}} = 2.3 \times 10^{-7} \text{ s}^{-1}$) for first and (b) ($E_b = 26.8 \text{ k}_B\text{T}$, $d = 2.9 \text{ nm}$, $k_{\text{off}} = 5.0 \times 10^{-6} \text{ s}^{-1}$) for second rupture, respectively.

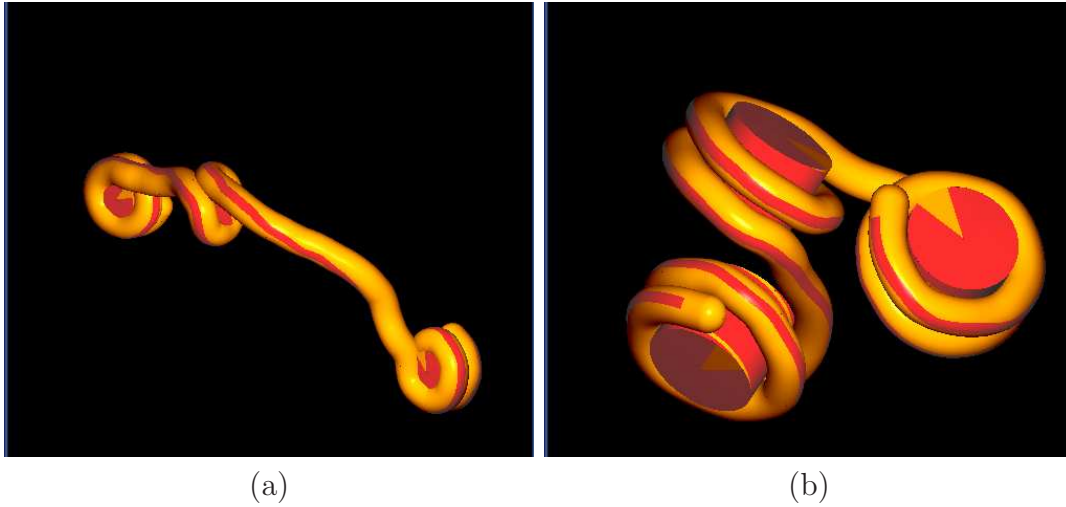


Figure 5.21: (a) Trinucleosome with bare DNA charge adopts an extended conformation ($\epsilon = 8 \text{ k}_B\text{T nm}^{-1}$), while (b) for renormalized DNA charge the structure is compacted ($\epsilon = 6 \text{ k}_B\text{T nm}^{-1}$).

Fig. (5.21) illustrating the different degree of compaction. In Tab. (5.5) the average center-to-center nucleosome distances between consecutive nucleosomes on the DNA and outer nucleosomes are listed. The electrostatic repulsion between the linker DNA favors an extended conformation of the trinucleosome for bare DNA charge, which is consistent to oligonucleosomes simulations [Arya and Schlick, 2006] observing the

strong electrostatic contribution of linker DNA to unfolding.

	I	II
bare DNA charge	20.5 nm	24.7 nm
renormalized DNA charge	13.4 nm	14.5 nm

Table 5.5: Average center-to-center nucleosome distances in trinucleosomes of (I) consecutive and (II) outer nucleosomes for bare ($\epsilon = 8 \text{ k}_\text{B} \text{T nm}^{-1}$) and renormalized DNA charge ($\epsilon = 6 \text{ k}_\text{B} \text{T nm}^{-1}$).

Chapter 6

Concluding Remarks

6.1 Conclusion

This thesis deals with the dynamics of DNA in plasmids and nucleosomes. In plasmids, the circular DNA adopts mostly a superhelical conformation, which brings two distant sites on the DNA ring in close proximity to each other. Such contacts are known to be necessary for the initiation of DNA transcription and replication. For the understanding of these processes, a detailed knowledge of the dynamics of individual DNA sites within the plasmid is required. Recently Fluorescence Correlation Spectroscopy (FCS) studies of single fluorophore-labeled DNA provided information on the motion of DNA monomers [Shusterman et al., 2004, 2008]. A goal of this thesis was to investigate the DNA monomer motion by numerical simulations and relate it to observations in the FCS experiments. Central questions concerned the effect of superhelicity, permanently bent DNA sequences and the fluorophore positioning on monomer dynamics.

DNA in the nucleosome is wrapped almost twofold around a protein complex. The nucleosome is not a static entity, but highly dynamic as shown by FRET [Gansen et al., 2009] and restriction enzyme accessibility [Polach and Widom, 1995] experiments. DNA fluctuations allow many proteins to access nucleosomal DNA, otherwise sterically occluded inside the nucleosome. Dynamic Force Spectroscopy (DFS) experiments have shown that a considerable energy barrier prevents the complete unwinding of the inner DNA turn from the histone core [Brower-Toland et al., 2002, Pope et al., 2005]. Furthermore the conformation of DNA in the nucleosome influences also the folding of nucleosomes into the higher-order chromatin structure. Therefore the local nucleosome structure determines the compaction of the chromatin fiber, which in turn makes certain regions of the genome accessible to regulatory proteins or not. In this context we studied conformational changes of DNA in the nucleosome by application of an external force, which allowed to study the transition between the wrapped and the unwrapped state. A major focus of this thesis is the determination of the unwrapping transition kinetics and strength of DNA-histone core interaction in relation to experimental DFS data.

The plasmids and nucleosomes were investigated by numerical simulations, which modeled the biological system, but also captured the basic features of the experimental

setups. The broad range of time and length scales involved in the problem necessitated the use of coarse-grained models. The DNA is modeled as a chain of linear segments interacting via harmonic potentials for bending, stretching and twisting, and incorporating hydrodynamic and electrostatic interactions based on the Brownian dynamics (BD) simulations described in [Klenin et al., 1998]. The nucleosome model [Wocjan et al., 2009a] takes into account the superhelical winding of DNA around the cylindrical shaped histone core as known from crystallographic data [Luger et al., 1997]. The DNA-histone core interaction is assumed to be uniformly distributed along the superhelical path. In the model the DNA ends can be stretched by a constant velocity/force, which provides a framework to simulate stretching experiments.

A first point concerned how well the dynamics of simulated DNA represent the motion of semiflexible polymers. In order to answer this question, the simulation results were compared with an analytical model of a semiflexible polymer. A suitable analytical description is given by a linear Gaussian chain with hydrodynamic interactions, which incorporates a bending rigidity [Harnau et al., 1996]. It was confirmed that the simulated mean-square displacement of single monomers is governed on length scales below the persistence length by the power law $\langle \vec{r}_i^2 \rangle \propto t^{3/4}$ as expected for stiff polymers [Kroy and Frey, 1997] and normal diffusion in the limit of large length scales $\langle \vec{r}_i^2 \rangle \propto t$. An excellent agreement was found between the analytical solution and numerical simulation, therefore validating this simulation approach. Rotational motion of a local DNA segment along the helical axis can be treated within the Gaussian semiflexible chain model, and rotations perpendicular to the helical DNA axis are consistent with the Zimm-Barkley model [Barkley and Zimm, 1979].

These findings allowed us to study the changes in DNA dynamics induced by circularization and superhelicity. Here, we focused on whether an acceleration of dynamics with increasing superhelical density can be observed. Circularization of torsionally relaxed DNA lead to only minor deviations from linear DNA. However, with increasing superhelicity the DNA ring undergoes a transition to a plectonemic structure subdivided into a stem region with interwound DNA strands, which is terminated by end-loops [Boles et al., 1990, Vologodskii et al., 1992]. The BD simulations showed that monomers in the end-loop structure are correlated with significantly faster motion, but due to continuous spatial reformation of the superhelix the effect averages out over time.

Hence, the relation indicates that the acceleration of dynamics possibly stems from a shift of the fluorophore-labeled monomer towards an end loop region, provided that the monomer remains a large fraction of time within the end loop. A stabilization of the end loop is known for naturally bent DNA sequences inside plasmids from electron-microscopy [Laundon and Griffith, 1988] and Monte Carlo simulations [Kremer et al., 1993]. Intriguingly, bent sequences can also be found in the studied pUC18 plasmid [Muzard et al., 1990] in proximity of the fluorophore-labeling site in the FCS study [Shusterman et al., 2008]. The insertion of a bent sequence caused that the motion of single monomers differs depending on their position relative to the bent sequence. With increasing superhelicity the monomer motion is accelerated within bent sequences, while is at the same time suppressed in the stem region.

A further point of interest was whether an additional intermediate regime appears, which was reported in experimental studies of circular (2.7 kbp) [Shusterman et al., 2008] and linear DNA (2-23 kbp) [Shusterman et al., 2004], and therein was associated with Rouse dynamics of the monomers $\langle \vec{r}_i^2 \rangle \propto t^{1/2}$. But for a sufficiently long semiflexible polymer as DNA it would be expected that at intermediate length scales motion is governed by Zimm dynamics $\langle \vec{r}_i^2 \rangle \propto t^{2/3}$, which brought up the question if dsDNA dynamics in dilute solution are controlled by hydrodynamic interactions. For the simulated short 2.7 kbp-DNA fragments the intramolecular contribution saturates fast due to the finite size of the polymer and therefore at first no intermediate regime was observed as seen in experiments by Shusterman et al..

A possible mechanism which explains the intermediate regime is provided in this thesis. The interaction of the dipole moment of the attached fluorophore with partially polarized excitation light, as found typically in FCS experiments, depends on the relative orientation. We accounted explicitly for the rotational motion of the dipole moment, which is assumed to coherently follow the local DNA segment. A subsequent simulation of the FCS process on the generated BD trajectories yielded a FCS autocorrelation function, revealing an apparent intermediate regime for the mean-square-displacement. We propose that the experimentally observed Rouse-like regime originates from the detection of the local DNA and fluorophore rotation, whose time-scale lies within the time-resolution of the FCS setup, and represents a cross-over regime from the rotational dynamics of the dipole moment to normal translational diffusion [Wocjan et al., 2009b]. Naturally, the full extent of fluorophore dynamics and fluorophore coupling to the DNA remains to be clarified in experimental studies.

In the second part of this thesis the dynamics of nucleosomes were studied. Regarding the fluctuations of DNA from the histone core at thermal equilibrium, we observed transient unwrapping events of the outer DNA turn. It was possible to relate the results to equilibrium constants of DNA site exposure from restriction enzyme accessibility assays [Polach and Widom, 1995] and therefore determine the strength of DNA-histone core interaction.

The application of an external force facilitated the DNA unwrapping and allowed us to probe the transition pathway to the unwrapped nucleosome state and associated conformations. As proposed in the stretching experiments [Brower-Toland et al., 2002], the nucleosome structure opens in distinct steps: In the first step, DNA gradually detaches from the histone core at low force, followed by disruptive release of the second DNA turn at the rupture force and is accompanied by a rotation of the histone core [Cui and Bustamante, 2000]. Characteristic force-extension curves as measured experimentally [Brower-Toland et al., 2002, Pope et al., 2005] have been calculated by the BD simulations. The rupture forces give insight into the underlying energy landscape. An analysis of the rupture force distribution in the framework of the DFS theory allowed us to calculate intrinsic kinetic rate constants and energy barriers of the unwrapping transition. For the strong pulling conditions the obtained simulation data was shown to be compatible with a model-dependent approach [Dudko et al., 2006] rather than the phenomenological model [Bell, 1978]. The predicted rupture force based on the analytical model were compared with available experimental rupture force data [Brower-Toland

et al., 2002, Pope et al., 2005], and provided quantitative statements about the DNA-histone core interaction strength as well as nucleosome binding energies.

At higher-order the nucleosomes compact into the chromatin fiber. An initial step towards the simulation of oligonucleosomes including internucleosomal interactions was also done in this thesis. We developed a model which allowed us to perform stretching simulations of dinucleosomes, which supported the findings regarding the transition parameters of single nucleosomes. Lastly the conformations of trinucleosome, the minimal unit already comprising all relevant interactions in the chromatin fiber, were studied, which showed folding/unfolding as function of the (linker) DNA charge.

6.2 Future perspectives

In this thesis single monomer dynamics in DNA molecules using BD simulations have been studied. A focus was put on the rotational motion of a fluorophore attached to the DNA and its relation to FCS experiments. As the studied DNA fragments were restricted to a single chain length, a logical extension would investigate the influence of increasing molecule length. A matter of particular interest is the interplay of the intermediate regime originating from the rotating dipole moment and the growing intramolecular contribution due to the increasing polymer flexibility for longer DNA molecules.

The present thesis provides an analysis of the DNA unwrapping transition in the nucleosome. The obtained predictions are based on the underlying assumptions inherent in the coarse-grained representation of the DNA and the histone octamer. On the other hand coarse-graining is necessary to limit the range of time and length scales involved in the problem, while it nevertheless leaves the possibility for more accurate modeling. Improvement could be done by incorporating localized interaction sites for the DNA-protein interaction and modulating the uniform adsorption energy density profile. A possible approach to this would be the distribution of discrete charges on the histone core surface to mimic the electrostatic potential of the protein complex. The assigned charges could be optimized to approximate the electrical field of the histone core at atomic resolution. The resulting nucleosome model would display in more detail crystallographic structure properties such as increasingly stronger DNA-histone interactions towards the nucleosome dyad axis, which are focused at interaction sites in 10 bp-intervals along the superhelical path. This would likely lead to more specific predictions of the nucleosome dynamics.

The refinement of the model also applies to the nucleosome-nucleosome interaction. One shortcoming concerns the salt-dependence of the internucleosomal potential. An important aspect on this is the role of histone tails mediating attractive interactions between neighboring nucleosomes. This would open the way to simulate more precisely, within the developed oligonucleosome simulation, stretching of nucleosome arrays, which combine at low-force, the opening of the chromatin fiber due to nucleosome rearrangement and at higher forces the disruption of individual nucleosomes.

Chapter 7

Appendix

The appendix provides a synopsis of the forces and torques due to the DNA-histone core interaction as defined in [Wocjan et al., 2009a]. The forces and torques are the partial derivatives of the DNA-histone core interaction energy $E_i^{(n)}$, given by Eq. (3.15), over the system coordinates.

The force $\vec{F}_i^{(n)}$ acting on the i th segment can be expressed as the sum

$$\vec{F}_i^{(n)} = \vec{F}_{i,next}^{(act)} + \vec{F}_{i,prev}^{(act)} - \vec{F}_{i,next}^{(rot)} + \vec{F}_{i,prev}^{(rot)}. \quad (7.1)$$

The contributions to the DNA-histone core interaction force acting on the i th vertex from the i th segment are $\vec{F}_{i,next}^{(act)}$ and $\vec{F}_{i,next}^{(rot)}$:

$$\vec{F}_{i,next}^{(act)} = \begin{cases} -\frac{U_0}{2r_0} \frac{\partial |\vec{R}_i|}{\partial \vec{r}_i^{(m)}} \left[\frac{\Theta_0 - \Theta}{\Theta_0} (1 - k_0) + k_0 \right] \\ + \frac{U_0}{2} \frac{r_0 - |\vec{R}_i|}{r_0} \frac{1 - k_0}{\Theta_0} \frac{1}{\sqrt{1 - (\vec{a}_i \cdot \vec{f}_i)^2}} \frac{\partial (\vec{a}_i \cdot \vec{f}_i)}{\partial \vec{r}_i^{(m)}} & \Theta < \Theta_0 \\ -\frac{U_0}{2r_0} k_0 \frac{\partial |\vec{R}_i|}{\partial \vec{r}_i^{(m)}} & \Theta \geq \Theta_0 \end{cases} \quad (7.2)$$

and

$$\vec{F}_{i,next}^{(rot)} = \begin{cases} U_0 \frac{r_0 - |\vec{R}_i|}{r_0} \frac{1 - k_0}{\Theta_0} \frac{1}{\sqrt{1 - (\vec{a}_i \cdot \vec{f}_i)^2}} \frac{\vec{e}_i \times (\vec{a}_i \times \vec{f}_i)}{|\vec{s}_i|} & \Theta < \Theta_0 \\ 0 & \Theta \geq \Theta_0, \end{cases} \quad (7.3)$$

where

$$\begin{aligned} \frac{\partial (\vec{a}_i \cdot \vec{f}_i)}{\partial \vec{r}_i^{(m)}} &= \vec{f}_i \left(\tau \left[\vec{c} \times \vec{b}_i \right] \times \vec{a}_i + \left[\vec{c} \times \vec{a}_i \right] \right) \frac{\vec{c} \times \vec{a}_i}{|\vec{r}_i^{(m)} - \vec{r}^{(n)}|} \\ \frac{\partial |\vec{R}_i|}{\partial \vec{r}_i^{(m)}} &= \frac{1}{|\vec{R}_i|} \left(-\vec{R}_i + \left(R^{(n)} \vec{R}_i \cdot \left[\vec{c} \times \vec{b}_i \right] - p \vec{R}_i \cdot \vec{c} \right) \frac{\vec{c} \times \vec{b}_i}{|\vec{r}_i^{(m)} - \vec{r}^{(n)}|} \right). \end{aligned}$$

The analogous contributions to the DNA-histone core interaction force acting on the i th vertex from the $(i-1)$ th segment are $\vec{F}_{i,prev}^{(act)}$ and $\vec{F}_{i,prev}^{(rot)}$. The terms $\vec{F}_{i,prev}^{(act)}$ and $\vec{F}_{i,prev}^{(rot)}$ can be obtained by substituting the i th terms with the corresponding $(i-1)$ th terms in the respective Eq. (7.2) and Eq. (7.3).

The torque $T_i^{(n)}$ on the i th segment is defined as

$$\vec{T}_i^{(n)} = \begin{cases} U_0 \frac{r_0 - |\vec{R}_i|}{r_0} \frac{1 - k_0}{\Theta_0} \left(1 - (\vec{a}_i \cdot \vec{f}_i)^2 \right)^{-\frac{1}{2}} \vec{a}_i \left[\vec{e}_i \times \vec{f}_i \right] & \Theta < \Theta_0 \\ 0 & \Theta \geq \Theta_0 \end{cases} \quad (7.4)$$

The counter force $\vec{F}^{(n)}$ and the counter torque $\vec{T}^{(n)}$ acting on the histone core are then given by

$$\vec{F}^{(n)} = - \sum_{i=0}^N \left(\vec{F}_{i,prev}^{(act)} + \vec{F}_{i,next}^{(act)} \right) \quad (7.5)$$

$$\vec{T}^{(n)} = - \sum_{i=0}^N \left(\vec{r}_i^{(m)} - \vec{r}^{(n)} \right) \times \left(\vec{F}_{i,prev}^{(act)} + \vec{F}_{i,next}^{(act)} \right). \quad (7.6)$$

Acknowledgements

An erster Stelle möchte ich mich bei Herrn Prof. Jörg Langowski bedanken für die Möglichkeit an einem spannenden und vielfältigen Thema zu arbeiten. Die erfahrene Unterstützung und gleichzeitig die gegebene Freiheit eigene Ansätze zu entwickeln war stets motivierend.

Herrn Prof. Jeremy C. Smith danke ich für die Übernahme des Koreferats.

Mein Dank gilt insbesondere Herrn Dr. Konstantin Klenin für die Zusammenarbeit, und seine Ratschläge und Anregungen, die wesentlich zum Gelingen der Arbeit beigetragen haben.

Ein großes Dankeschön gilt auch Karine Voltz, Georgi Pachov und Mithun Biswas für zahlreiche Gespräche über Nukleosome und auch darüberhinaus.

Es war eine Freude mit Herrn Dr. Oleg Krichevsky und Jan Krieger zusammenzuarbeiten. Bei der Diskussion und Lösung zahlreicher Probleme waren Jan Krieger und Christian Fritsch immer eine große Hilfe.

Für die Korrektur des Manuskriptes bedanke ich mich bei Christian Fritsch, Vera Böhm, Alexander Gansen, Jan Krieger, Aaron Hieb, Gerd Grünert und Tabea Elbel. Meine Zimmerkollegen Christian Fritsch, Annika Wedemeier und Karine Voltz übernehmen die volle Verantwortung für die vielen heiteren Stunden des wissenschaftlichen Arbeitens.

Allen Mitgliedern des Instituts "Biophysik der Makromoleküle" am DKFZ, Heidelberg danke ich für die angenehme und interessante Zeit.

Publications

T.Wocjan, K.Klenin, and J.Langowski. Brownian dynamics simulation of DNA Unrolling from the Nucleosome. *J.Phys. Chem. B* 113, 2639-2646, 2009

T.Wocjan, J.Krieger, O.Krichevsky, and J.Langowski. Dynamics of a fluorophore attached to superhelical DNA:FCS experiments simulated by Brownian dynamics. *Phys. Chem. Chem. Phys.* DOI:10.1039/B911857H, 2009

Bibliography

- M. Abramowitz and I.A. Stegun. *Handbook of mathematical functions*. Dover, New York, 1970.
- M. Adrian, B. ten Heggeler-Bordier, W. Wahli, A.Z Stasiak, A. Stasiak, and J. Dubochet. Direct visualization of supercoiled DNA molecules in solution. *EMBO J.*, 9: 4551–4554, 1990.
- B. Alberts, A. Johnson, J. Lewis, M. Raff, K. Roberts, and P. Walter. *Molecular Biology of the Cell*. Garland Science (Taylor & Francis Group), New York, 2002.
- M.P. Allen and D.J. Tildesley. *Computer Simulations of Liquids*. Oxford University Press, Oxford, 1989.
- S.A. Allison and J.M. Schurr. Torsion dynamics and depolarization of fluorescence of linear macromolecules. i. theory and application to DNA. *Chem. Phys.*, 41:35–59, 1979.
- J.D. Anderson and J. Widom. Sequence and position-dependence of the equilibrium accessibility of nucleosomal DNA target sites. *J. Mol. Biol.*, 296:976–987, 2000.
- S. R. Aragón and R. Pecora. Fluorescence correlation spectroscopy and brownian rotational diffusion. *Biopolymers*, 14:119–138, 1975.
- L. Arcesi, G. La Penna, and A. Perico. Generalized electrostatic model of the wrapping of DNA around oppositely charged proteins. *Biopolymers*, 86:127–135, 2007.
- G. Arents, R.W. Burlingame, B.-C. Wang, W.E. Love, and E.N. Moudrianakis. The nucleosomal core histone octamer at 3.1 Å resolution: A tripartite protein assembly and a left-handed superhelix. *Proc. Natl. Acad. Sci. U.S.A.*, 88:10148–10152, 1991.
- G. Arents and E.N. Moudrianakis. Topography of the histone octamer surface: Repeating structural motifs utilized in the docking of nucleosomal DNA. *Proc. Natl. Acad. Sci. U.S.A.*, 90:10489–10493, 1993.
- G. Arya and T. Schlick. Role of histone tails in chromatin folding revealed by a mesoscopic oligonucleosome model. *Proc. Natl. Acad. Sci. U.S.A.*, 103:16236–16241, 2006.
- G. Arya, Q. Zhang, and T. Schlick. Flexible histone tails in a new mesoscopic oligonucleosome model. *Biophys. J.*, 91:133–150, 2006.

- A. Ashkin, J.M. Dziedzic, J.E. Bjorkholm, and S. Chu. Observation of a single-beam gradient force optical trap for dielectric particles. *Opt. Lett.*, 11:288–290, 1986.
- M.D. Barkley and B.H. Zimm. Theory of twisting and bending of chain macromolecules; analysis of the fluorescence depolarization of DNA. *J. Chem. Phys.*, 70:2991–3007, 1979.
- J. Bednar, R.A. Horowitz, S.A. Grigoryev, L.M. Carruthers, J.C. Hansen, A.J. Koster, and C.L. Woodcock. Nucleosomes, linker DNA, and linker histone form a unique structural motif that directs the higher-order folding and compaction of chromatin. *Proc. Natl. Acad. Sci. U.S.A.*, 95:14173–14178, 1998.
- G.I. Bell. Models for the specific adhesion of cells to cells. *Science*, 200(4342):618–627, 1978.
- B.J. Berne and P. Pechukas. Gaussian model potentials for molecular interactions. *J. Chem. Phys.*, 56(8):4213–4216, 1972.
- G. Binning, C.F. Quate, and Ch. Gerber. Atomic force microscope. *Phys. Rev. Lett.*, 56(9):930–934, 1985.
- T.C. Boles, J.H. White, and N.R. Cozzarelli. Structure of plectonemically supercoiled DNA. *J. Mol. Biol.*, 213:931–951, 1990.
- N. Borochoy, H. Eisenberg, and Z. Kam. Dependence of DNA conformation on the concentration of salt. *Biopolymers*, 20:231–235, 1981.
- B.D. Brower-Toland, C.L. Smith, R.C. Yeh, J.T. Lis, C.L. Peterson, and M.D. Wang. Mechanical disruption of individual nucleosomes reveals a reversible multistage release of DNA. *Proc. Natl. Acad. Sci. U.S.A.*, 99:1960–1965, 2002.
- B.D. Brower-Toland, D.A. Wacker, R.M. Fulbright, J.T. Lis, W. Lee Kraus, and M.D. Wang. Specific contributions of histone tails and their acetylation to the mechanical stability of nucleosomes. *J. Mol. Biol.*, 346:135–146, 2005.
- F. Bueche. The viscoelastic properties of plastics. *J. Chem. Phys.*, 22(4):603–609, 1954.
- C.R. Calladine, H.R. Drew, B.F. Luisi, and A.A. Travers. *Understanding DNA*. Elsevier Academic Press, London, 2004.
- B. Carrasco, J.G. de la Torre, and P. Zipper. Calculation of hydrodynamic properties of macromolecular bead models with overlapping spheres. *Eur. Biophys. J.*, 28: 510–515, 1999.
- D.J. Clark and T. Kimura. Electrostatic mechanism of chromatin folding. *J. Mol. Biol.*, 211:883–896, 1990.

- A. Corana, M. Marchesi, C. Martini, and S. Ridella. Minimizing multimodal functions of continuous variables with the "simulated annealing" algorithm. *ACM Transactions on Mathematical Software*, 13:262–280, 1987.
- Y. Cui and C. Bustamante. Pulling a single chromatin fiber reveals the forces that maintain its higher-order structure. *Proc. Natl. Acad. Sci. U.S.A.*, 97:127–132, 2000.
- R.J. Davenport, G.J.L. Wuite, R. Landick, and C. Bustamante. Single-molecule study of transcriptional pausing and arrest by *E. coli* RNA polymerase. *Science*, 287:2497–2500, 2000.
- C.A. Davey, D.F. Sargent, K. Luger, A.W. Maeder, and T.J. Richmond. Solvent mediated interactions in the structure of the nucleosome core particle at 1.9 Å resolution. *J. Mol. Biol.*, 319:1097–1113, 2002.
- C. De Haen, R.A. Easterly, and D.C. Teller. Translational friction of rigid assemblies of spheres: Derivation and application of new hydrodynamic interaction tensors. *Biopolymers*, 22:1133–1143, 1983.
- J.A. Dix, E.F.Y. Hom, and A.S. Verkman. Fluorescence correlation spectroscopy simulations of photophysical phenomena and molecular interactions: A molecular dynamics/monte carlo approach. *J. Phys. Chem.*, 110:1896–1906, 2006.
- M. Doi and S.F. Edwards. *The Theory of Polymer Dynamics*. Oxford University Press, Oxford, 1986.
- O.K. Dudko, A.E. Filippov, J. Klafter, and M. Urbakh. Beyond the conventional description of dynamic force spectroscopy of adhesion bonds. *Proc. Natl. Acad. Sci. U.S.A.*, 100(20):11378–11381, 2003.
- O.K. Dudko, G. Hummer, and A. Szabo. Intrinsic rates and activation free energies from single-molecule pulling experiments. *Phys. Rev. Lett.*, 96(108101), 2006.
- E.L. Elson and D. Magde. Fluorescence correlation spectroscopy. i. conceptual basis and theory. *Biopolymers*, 13:1–27, 1974.
- A.P.J. Emerson, G.R. Luckhurst, and S.G. Whatling. Computer simulation studies of anisotropic systems xxiii. the gay-berne discogen. *Molecular Physics*, 82:113–124, 1994.
- D.L. Ermak and J.A. McCammon. Brownian dynamics with hydrodynamic interactions. *J. Chem. Phys.*, 69:1352–1360, 1978.
- E Evans and K Ritchie. Dynamic strenght of molecular adhesion bonds. *Biophys. J.*, 72:1541–1555, 1997.
- E Evans and K Ritchie. Strength of a weak bond connecting flexible polymer chains. *Biophys. J.*, 76:2439–2447, 1999.
- G. Felsenfeld and A. Klug. Controlling the double helix. *Nature*, 42:448–453, 2003.

- J. Finch and A. Klug. Solenoidal model for superstructure in chromatin. *Proc. Natl. Acad. Sci. U.S.A.*, 73:1897–1901, 1976.
- J.T. Finch, L.C. Lutter, D. Rhodes, R.S. Brown, B. Rushton, M. Levitt, and A. Klug. Structure of nucleosome core particles of chromatin. *Nature*, 269:29–36, 1977.
- P.J. Flory. *Statistical Mechanics of Chain Molecules*. Oxford University Press, New York, 1988.
- N.R. Forde, D. Izhaky, G.R. Woodcock, G.J.L. Wuite, and C. Bustamante. Using mechanical force to probe the mechanism of pausing and arrest during continuous elongation by Escherichia coli RNA polymerase. *Proc. Natl. Acad. Sci. U.S.A.*, 99:11682–11687, 2002.
- T. Förster. Zwischenmolekulare Energiewanderung und Fluoreszenz. *Annalen der Physik*, 2:55–75, 1948.
- R.W. Friddle. Unified model of dynamic forced barrier crossing in single molecules. *Phys. Rev. Lett.*, 100(138302), 2008.
- A. Gansen, K. Tóth, N. Schwarz, and J. Langowski. Structural variability of nucleosomes detected by single-pair Förster resonance energy transfer: Histone acetylation, sequence variation, and salt effects. *J. Phys. Chem.*, pages 2604–2613, 2009.
- A. Garg. Escape-field distribution for escape from a metastable potential well subject to a steadily increasing bias field. *Phys. Rev. B*, 51(21):15592–15595, 1995.
- J.G. Gay and B.J. Berne. Modification of the overlap potential to mimic a linear site-site potential. *J. Chem. Phys.*, 74(6):3316–3319, 1981.
- G.J. Gemmen, R. Sim, K.A. Haushalter, Pu Chun Ke, J.T. Kadonaga, and D.E. Smith. Forced unraveling of nucleosomes assembled on heterogeneous DNA using core histones, nap-1, and acf. *J. Mol. Biol.*, 351:89–99, 2005.
- C. Gergely, J.-C. Voegel, P. Schaaf, B. Senger, M. Maaloum, J.K.H. Hörber, and J. Hemmerlé. Unbinding process of adsorbed proteins under external stress studied by atomic force microscopy. *Proc. Natl. Acad. Sci. U.S.A.*, 97(20):10802–10807, 2000.
- R.F. Goldstein. Macromolecular diffusion constants: A calculational strategy. *J. Chem. Phys.*, 83:2390–2397, 1985.
- A.Y. Grosberg and A.R. Khokhlov. *Statistical Physics of Macromolecules*. AIP Press, New York, 1994.
- P.J. Hagerman. Flexibility of DNA. *Ann. Rev. Biophys. Biophys. Chem.*, 17:265, 1988.
- P.J. Hagerman and B.H. Zimm. Monte carlo approach to the analysis of the rotational diffusion of wormlike chains. *Biopolymers*, 20:1481–1502, 1981.

- M. Hammermann, N. Brun, K.V. Klenin, R. May, K. Tóth, and J. Langowski. Salt-dependent DNA superhelix diameter studied by small angle neutron scattering measurements and monte carlo simulations. *Biophys. J.*, 75:3057–3063, 1998.
- P. Hänggi, P. Talkner, and M. Borkovec. Reaction-rate theory: fifty years after kramers. *Rev. Mod. Phys.*, 62:251–336, 1990.
- L. Harnau, R.G. Winkler, and P. Reineker. Dynamic properties of molecular chains with variable stiffness. *J. Chem. Phys.*, 102:7750–7757, 1995.
- L. Harnau, R.G. Winkler, and P. Reineker. Dynamic structure factor of semiflexible macromolecules in dilute solution. *J. Chem. Phys.*, 104:6355–6368, 1996.
- P.J. Heath, J.B. Clendenning, B.S. Fujimoto, and J.M. Schurr. Effect of bending strain on the torsion elastic constant of DNA. *J. Mol. Biol.*, 260:718–730, 1996.
- D.R. Hewish and L.A. Burgoyne. Chromatin sub-structure: the digestion of chromatin DNA at regularly spaced sites by a nuclear deoxyribonuclease. *Biochem. Biophys. Res. Comm.*, 52:504–510, 1973.
- M. Hinczewski, X. Schlagberger, M. Rubinstein, O. Krichevsky, and R.R. Netz. End-monomer dynamics in semiflexible polymers. *Macromolecules*, 42:860–875, 2009.
- D.S. Horowitz and J.C. Wang. Torsional rigidity of DNA and length dependence of the free energy of DNA supercoiling. *J. Mol. Biol.*, 173:75–91, 1984.
- G. Hummer and A. Szabo. Free energy reconstruction from nonequilibrium single-molecule pulling experiments. *Proc. Natl. Acad. Sci. U.S.A.*, 98:3658–3661, 2001.
- A. Iniesta and J. Garcia de la Torre. A second-order algorithm for the simulation of the brownian dynamics of macromolecular models. *J. Chem. Phys.*, 92:2015, 1990.
- C. Jarzynski. Equilibrium free-energy differences from nonequilibrium measurements: A master-equation approach. *Phys. Rev. E*, 56:5018–5035, 1997a.
- C. Jarzynski. Nonequilibrium equality for free energy differences. *Phys. Rev. Lett.*, 78 (14):2690–2693, 1997b.
- H. Jian, T. Schlick, and A. Vologodskii. Internal motion of supercoiled DNA: Brownian dynamics simulations of site juxtaposition. *J. Mol. Biol.*, 284:287–296, 1998.
- H. Jian, A.V. Vologodskii, and J. Garcia de la Torre. A combined wormlike-chain and bead model for dynamic simulations of long linear DNA. *J. Computational. Phys.*, 136:168–179, 1997.
- V. Kabadi. Molecular dynamics of fluids: the gaussian overlap model ii. *Ber. Bunsenges. Phys. Chem.*, 90:327–332, 1986a.
- V. Kabadi. Statistical mechanics of non-spherical molecules: spherical harmonic expansions on non-spherical surfaces ii: Gay-berne gaussian overlap potential. *Ber. Bunsenges. Phys. Chem.*, 90:332–339, 1986b.

- P. Kask, P. Piksarv, Ü. Mets, and E. Lippmaa. Fluorescence correlation spectroscopy in the nanosecond time range: rotational diffusion of bovine carbonic anhydrase b. *Eur. Biophys. J.*, 14:257–261, 1987.
- P. Kask, P. Piksarv, M. Pooga, Ü. Mets, and E. Lippmaa. Separation of the rotational contribution in fluorescence correlation experiments. *Biophys. J.*, 55:213–220, 1989.
- S.N. Khrapunov, A.I. Dragan, A.V. Sivolob, and A.M. Zagariya. Mechanisms of stabilizing nucleosome structure. study of dissociation of histone octamer from DNA. *Biochem. Biophys. Acta*, 1351:213–222, 1997.
- K. Klenin, M. Hammermann, and J. Langowski. Modeling dynamic light scattering of supercoiled DNA. *Macromolecules*, 33:1459–1466, 2000.
- K. Klenin and J. Langowski. Computation of writhe in modeling of supercoiled DNA. *Biopolymers*, 54:307–317, 2000.
- K.V. Klenin, M.D. Frank-Kamenetskii, and J. Langowski. Modulation of intramolecular interactions in superhelical DNA by curved sequences: A monte carlo simulation study. *Biophys. J.*, 68:81–88, 1995.
- K.V. Klenin and J. Langowski. Modelling of intramolecular reactions of polymers: An efficient method based on brownian dynamics simulations. *J. Chem. Phys.*, 121:4951–4960, 2004.
- K.V. Klenin, H. Merlitz, and J. Langowski. A brownian dynamics program for the simulation of linear and circular DNA and other wormlike chain polyelectrolytes. *Biophys. J.*, 74(2):780–788, 1998.
- K.V. Klenin, A.V. Vologodskii, V.A. Vadim, A.M. Dykhne, and M.D. Frank-Kamenetskii. Computer simulation of DNA supercoiling. *J. Mol. Biol.*, 217:413–419, 1991.
- R.H. Koehler, P. Schwille, W.W. Webb, and M.R. Hanson. Active protein transport through plastid tubules: velocity quantified by fluorescence correlation spectroscopy. *J. Cell. Sci.*, 113:3921–3930, 2000.
- I. Koltover, T. Salditt, and C.R. Safinya. Phase diagram, stability, and overcharging of lamellar cationic lipid-DNA self-assembled complexes. *Biophys. J.*, 77:915–924, 1999.
- W.J.A. Koopmans, A. Brehm, C. Logie, T. Schmidt, and J. van Noort. Single-pair FRET microscopy reveals mononucleosome dynamics. *J. Fluoresc.*, 17:785–795, 2007.
- R.D. Kornberg. Chromatin structure: A repeating unit of histones and DNA. *Science*, 184:868–871, 1974.
- W.A. Krajewski. Histone acetylation status and DNA sequence modulate ATP-dependent nucleosome repositioning. *J. Biol. Chem.*, 277:14509–14513, 2002.

- H.A. Kramers. Brownian motion in a field of force and the diffusion model of chemical reactions. *Physica*, VII(4):284–304, 1940.
- O. Kratky and G. Porod. Röntgenuntersuchung gelöster Fadenmoleküle. *Recl. Trav. Chim. Pays-Bas*, 68:1106, 1949.
- W. Kremer, K. Klenin, S. Diekmann, and J. Langowski. DNA curvature influences the internal motions of supercoiled DNA. *EMBO J.*, 12:4407–4412, 1993.
- J. Krieger. Fluorescence correlation spectroscopy simulation toolbox (private communication). 2009.
- K. Kroy and E. Frey. Dynamic scattering from solutions of semiflexible polymers. *Phys. Rev. E*, 55:2469–2476, 1997.
- M. Kruithof, F. Chien, M. de Jager, and J. van Noort. Subpiconewton dynamic force spectroscopy using magnetic tweezers. *Biophys. J.*, 94:2343–2348, 2008.
- I.M. Kulić and H. Schiessel. DNA spools under tension. *Phys. Rev. Lett.*, 92(228101), 2004.
- K.-K. Kunze and R.R. Netz. Salt-induced DNA-histone complexation. *Phys. Rev. Lett.*, 85:4389–4392, 2000.
- K.-K. Kunze and R.R. Netz. Complexes of semiflexible polyelectrolytes and charged spheres as models for salt-modulated nucleosomal structures. *Phys. Rev. E*, 66(011918), 2002.
- J. Kurkijärvi. Intrinsic fluctuations in a superconducting ring closed with a josephson junction. *Phys. Rev. B*, 6(3):832–835, 1972.
- J. Langowski, U. Kapp, K. Klenin, and A. Vologodskii. Solution structure and dynamics of DNA topoisomers: Dynamic light scattering studies and monte carlo simulations. *Biopolymers*, 34:639–646, 1994.
- C.H. Laundon and J.D. Griffith. Curved helix segments can uniquely orient the topology of supertwisted DNA. *Cell*, 52:545–549, 1988.
- A. Leforestier, J. Dubochet, and F. Livolant. Bilayers of nucleosome core particles. *Biophys. J.*, 81:2414–2421, 2001.
- A. Leforestier and F. Livolant. Liquid crystalline ordering of nucleosome core particles under macromolecular crowding conditions: evidence for a discotic columnar hexagonal phase. *Biophys. J.*, 73:1771–1776, 1997.
- J.E. Lennard-Jones. Cohesion. *Proceedings of the Physical Society*, 43(240):461–482, 1931.

- S.H. Leuba, G. Yang, C. Robert, B. Samori, K. van Holde, J. Zlatanova, and C. Bustamante. Three-dimensional structure of extended chromatin fibers as revealed by tapping-mode scanning force microscopy. *Proc. Natl. Acad. Sci. U.S.A.*, 91:11621–11625, 1994.
- G. Li, M. Levitus, C. Bustamante, and J. Widom. Rapid spontaneous accessibility of nucleosomal DNA. *Nat. Struct. Mol. Biol.*, 12:46–53, 2005.
- H.J. Lin, H.Y. Chen, Y.J. Sheng, and H.K. Tsao. Bell’s expression and the generalized garg form for forced dissociation of a biomolecular complex. *Phys. Rev. Lett.*, 98 (088304), 2007.
- J. Liphardt, B. Onoa, S.B. Smith, I. Tinoco Jr., and C. Bustamante. Reversible unfolding of single RNA molecules by mechanical force. *Science*, 292:733–737, 2001.
- P.T. Lowary and J. Widom. New DNA sequence rules for high affinity binding to histone octamer and sequence-directed nucleosome positioning. *J. Mol. Biol.*, 276: 19–42, 1998.
- K. Luger, A.W. Maeder, R.K. Richmond, D.F. Sargent, and T.J. Richmond. Crystal structure of the nucleosome core particle at 2.8 Å resolution. *Nature*, 389:251, 1997.
- K. Luger and T.J. Richmond. DNA binding within the nucleosome core. *Curr. Opin. Struct. Biol.*, 8:33–40, 1998.
- D. Lumma, S. Keller, T. Vilgis, and J. O. Rädler. Dynamics of large semiflexible chains probed by fluorescence correlation spectroscopy. *Phys. Rev. Lett.*, 90(21): 218301, 2003.
- D. Magde, E.L. Elson, and W.W. Webb. Fluorescence correlation spectroscopy. ii. an experimental realization. *Biopolymers*, 13:29–61, 1974.
- D. Magde, E.L. Elson, and W.W. Webb. Fluorescence correlation spectroscopy. ii. uniform translation and laminar flow. *Biopolymers*, 17:361–376, 1978.
- G.S. Manning. Limiting laws and counterion condensation in polyelectrolyte solutions. i. colligative properties. *J. Chem. Phys.*, 51:924–933, 1969a.
- G.S. Manning. Limiting laws and counterion condensation in polyelectrolyte solutions. iii. an analysis based on the mayer ionic solution theory. *J. Chem. Phys.*, 51:3249–3252, 1969b.
- G.S. Manning. Limiting laws and counterion condensation in polyelectrolyte solutions. iv. the approach to the limit and the extraordinary stability of the charge fraction. *Biophys. Chem.*, 7:95–102, 1977.
- G.S. Manning. A procedure for extracting persistence lengths from light-scattering data on intermediate molecular weight DNA. *Biopolymers*, 20:1751–1755, 1981.

- J.F. Marko. The internal 'slithering' dynamics of supercoiled DNA. *Physica A*, 244: 263–277, 1997.
- J.F. Marko and E.D. Siggia. Statistical mechanics of supercoiled DNA. *Phys. Rev. E*, 52:2912–2938, 1995.
- N.L. Marky and G.S. Manning. The elastic resilience of DNA can induce all-or-none structural transitions in the nucleosome core particle. *Biopolymers*, 31:1543, 1991.
- N.L. Marky and G.S. Manning. A theory of DNA dissociation from the nucleosome. *J. Mol. Biol.*, 254(1):50–61, 1995.
- H. Merlitz, K. Rippe, K.V. Klenin, and J. Langowski. Looping dynamics of linear DNA molecules and the effect of DNA curvature: A study by brownian dynamics simulation. *Biophys. J.*, 74:773–779, 1998.
- C. Muchardt and M. Yaniv. ATP-dependent chromatin remodelling: SWI/SNF and co. are on the job. *J. Mol. Biol.*, 293:187–198, 1999.
- G. Muzard, B. Théveny, and B. Révet. Electron microscopy mapping of pBR322 DNA curvature. comparison with theoretical models. *EMBO J.*, 9:1289–1298, 1990.
- D.N. Nikova, L.H. Pope, M.L. Bennink, K.A. van Leijenhorst-Groener, K. van der Werf, and J. Greve. Unexpected binding motifs for subnucleosomal particles revealed by atomic force microscopy. *Bio. Phys. J.*, 87:4135–4145, 2004.
- A.L. Olins and D.E. Olins. Spheroid chromatin units (ν bodies). *Science*, 183(4122): 330–332, 1974.
- E.P. Petrov, T. Ohrt, R.G. Winkler, and P. Schwille. Diffusion and segmental dynamics of double-stranded DNA. *Phys. Rev. Lett.*, 97(258101), 2006.
- C. Pfannschmidt, A. Schaper, G. Heim, T.M. Jovin, and J. Langowski. Sequence-specific labeling of superhelical DNA by triple helix formation and psoralen crosslinking. *Nucl. Acids. Res.*, 24:1702–1709, 1996.
- K.J. Polach and J. Widom. Mechanism of protein access to specific DNA sequences in chromatin: A dynamic equilibrium model for gene regulation. *J. Mol. Biol.*, 254: 130–149, 1995.
- L.H. Pope, M.L. Bennink, K.A. van Leijenhorst-Groener, D. Nikova, J. Greve, and J.F. Marko. Single chromatin fiber stretching reveals physically distinct populations of disassembly events. *Biophys. J.*, 88:3572–3583, 2005.
- T.J. Richmond and C.A. Davey. The structure of DNA in the nucleosome. *Nature*, 423:145–150, 2003.
- T.J. Richmond, J.T. Finch, B. Rushton, D. Rhodes, and A. Klug. Structure of the nucleosome core particle at 7 Å resolution. *Nature*, 311:532–537, 1984.

- P.D. Ross and R.L. Scruggs. Electrophoresis of DNA. ii. specific interactions of univalent and divalent cations with DNA. *Biopolymers*, 2:79–89, 2004.
- J. Rotne and S. Prager. Variational treatment of hydrodynamic interaction in polymers. *J. Chem. Phys.*, 50:4831–4837, 1969.
- P.E. Rouse. A theory of the linear viscoelastic properties of dilute solutions of coiling polymers. *J. Chem. Phys.*, 21:1272–1280, 1953.
- M. Rubinstein and R.H. Colby. *Polymer Physics*. Oxford University Press, New York, 2003.
- A. Saha, J. Wittmeyer, and B.R. Cairns. Chromatin remodelling: the industrial revolution of DNA around histones. *Nat. Rev. Mol. Cell Biol.*, 7:437–447, 2006.
- T. Sakaue and K. Yoshikawa. Histone core slips along DNA and prefers positioning at the chain end. *Phys. Rev. Lett.*, 87:078105, 2001.
- T. Schalch, S. Duda, D.F. Sargent, and T.J. Richmond. X-ray structure of a tetranucleosome and its implications for the chromatin fibre. *Nature*, 436:138–141, 2005.
- J.A. Schellman and D. Stigter. Electrical double layer, zeta potential, and electrophoretic charge of double-stranded DNA. *Biopolymers*, 16:1415–1434, 1977.
- H. Schiessel. The physics of chromatin. *J. Phys.: Condens. Matter*, 15, 2003.
- H. Schiessel, J. Rudnick, R. Bruinsma, and W.M. Gelbert. Organized condensation of worm-like chains. *Europhys. Lett.*, 51:237, 2000.
- P. Sens and J.-F. Joanny. Counterion release and electrostatic adsorption. *Phys. Rev. Lett.*, 84:4862–4866, 2000.
- D. Shore and R.L. Baldwin. Energetics of DNA twisting: II. topoisomer analysis. *J. Mol. Biol.*, 170:983–1007, 1983.
- T.E. Shrader and D.M. Crothers. Effects of DNA sequence and histone-histone interactions on nucleosome placement. *J. Mol. Biol.*, 216:69–84, 1990.
- R. Shusterman, S. Alon, T. Gavrinov, and O. Krichevsky. Monomer dynamics in double- and single-stranded DNA polymers. *Phys. Rev. Lett.*, 92(4), 2004.
- R. Shusterman, T. Gavrinov, and O. Krichevsky. Internal dynamics of superhelical DNA. *Phys. Rev. Lett.*, 100(098102), 2008.
- R.T. Simpson. Structure of the chromatosome, a chromatin particle containing 160 base pairs of DNA and all the histones. *Biochemistry*, 17:5524–5531, 1978.
- E.S. Sobel and J.A. Harpst. Effects of Na⁺ on the persistence length and excluded volume of T7 bacteriophage DNA. *Biopolymers*, 31:1559–1564, 1991.

- D. Stigter. Interactions of highly charged colloidal cylinders with applications to double-stranded DNA. *Biopolymers*, 16:1435–1448, 1977.
- T.R. Strick, J.-F. Allemand, D. Bensimon, A. Bensimon, and V. Croquette. The elasticity of a single supercoiled DNA molecule. *Science*, 271:1835–1838, 1996.
- A. Szabo and G. Hummer. Kinetics from nonequilibrium single-molecule pulling experiments. *Biophys. J.*, 85:5–15, 2003.
- W.H. Taylor and P.J. Hagerman. Application of the method of phage T4 DNA ligase-catalyzed ring-closure to the study of DNA structure: Ii. NaCl-dependence of DNA flexibility and helical repeat. *J. Mol. Biol.*, 212:363–376, 1990.
- M.M. Tirado and J.G. de la Torre. Translational friction coefficients of rigid, symmetric top macromolecules. application to circular cylinders. *J. Chem. Phys.*, 71:2581–2587, 1979.
- M.M. Tirado and J.G. de la Torre. Rotational dynamics of rigid, symmetric top macromolecules. application to circular cylinders. *J. Chem. Phys.*, 73:1986–1993, 1980.
- M. Tomschik, H. Zheng, K. van Holde, J. Zlatanova, and S.H. Leuba. Fast, long-range, reversible conformational fluctuations in nucleosomes revealed by single-pair fluorescence resonance energy transfer. *Proc. Natl. Acad. Sci. U.S.A.*, 102:3278–3283, 2005.
- K. Tóth, N. Brun, and J. Langowski. Chromatin compaction at the mononucleosome level. *Biochemistry*, 45:1591–1598, 2006.
- K.E. van Holde. *Chromatin*. Springer, New York, 1989.
- J. Vinograd, J. Lebowitz, R. Radloff, R. Watson, and P. Laipis. The twisted circular form of polyoma viral DNA. *Biochemistry*, 53:1104–1111, 1965.
- A.V. Vologodskii, S.D. Levene, K.V. Klenin, M.D. Frank-Kamenetskii, and N.R. Cozzarelli. Conformational and thermodynamic properties of supercoiled DNA. *J. Mol. Biol.*, 227:1224–1243, 1992.
- M. Wachsmuth, W. Waldeck, and J. Langowski. Anomalous diffusion of fluorescent probes inside living cell nuclei investigated by spatially-resolved fluorescence correlation spectroscopy. *J. Mol. Biol.*, 298:677–689, 2000.
- P. Wahl, J. Paoletti, and J.B. Le Pecq. Decay of fluorescence emission anisotropy of the ethidium bromide-DNA complex evidence for an internal motion in DNA. *Proc. Natl. Acad. Sci. U.S.A.*, 65:417–421, 1970.
- T.A. Waigh. *Applied Biophysics*. John Wiley & Sons, Ltd, West Sussex, 2007.
- S.A. Wasserman and N.R. Cozzarelli. Biochemical topology: Applications to DNA recombination and replication. *Science*, 232:951–960, 1986.

- G. Wedemann and J. Langowski. Computer simulation of the 30-nanometer chromatin fiber. *Biophys. J.*, 82:2847–2859, 2002.
- M. Weiss, M. Elsner, F. Kartberg, and T. Nilsson. Anomalous subdiffusion is a measure for cytoplasmic crowding in living cells. *Biophys. J.*, 87:3518–3524, 2004.
- J.H. White. Self-linking and the gauss integral in higher dimensions. *Am. J. of Mathematics*, 91:693–728, 1969.
- J.H. White and W.R. Bauer. Calculation of the twist and the writhe for representative models of DNA. *J. Mol. Biol.*, 189:329, 1986.
- J. Widengren, Ü. Mets, and R. Rigler. Fluorescence correlation spectroscopy of triplet states in solution: a theoretical and experimental study. *J. Phys. Chem.*, 99(36): 13368–13379, 1995.
- R. Williamson. Properties of rapidly labelled deoxyribonucleic acid fragments isolated from the cytoplasm of primary cultures of embryonic mouse liver cells. *J. Mol. Biol.*, 51:157–168, 1970.
- R.G. Winkler, S. Keller, and J.O. Rädler. Intramolecular dynamics of linear macromolecules by fluorescence correlation spectroscopy. *Phys. Rev. E*, 73(041919), 2006.
- T. Wocjan, K.V. Klenin, and J. Langowski. Brownian dynamics simulation of DNA unrolling from the nucleosome. *J. Phys. Chem. B*, 113(9):2639–2646, 2009a.
- T. Wocjan, J. Krieger, O. Krichevsky, and J. Langowski. Dynamics of a fluorophore attached to superhelical DNA: FCS experiments simulated by brownian dynamics. *Phys. Chem. Chem. Phys.*, (DOI:10.1039/B911857H), 2009b.
- A. Wolffe. *Chromatin: Structure and Function*. Academic Press Limited, London, 1995.
- C.L.F. Woodcock. Ultrastructure of inactive chromatin. *J. Cell. Biol.*, 59:368a, 1973.
- H. Yin, M.D. Wang, K. Svoboda, R. Landick, S.M. Block, and J. Gelles. Transcription against an applied force. *Science*, 270:1653–1657, 1995.
- B.H. Zimm. Dynamics of polymer molecules in dilute solution: Viscoelasticity, flow birefringence and dielectric loss. *J. Chem. Phys.*, 24:269–278, 1956.
- J. Zlatanova, S.H. Leuba, and K. van Holde. Chromatin fiber structure: Morphology, molecular determinants, structural transitions. *Biophys. J.*, 74:2554–2566, 1998.